FUNCTIONALIZED SILICONE COMPOSITES: OMNIPHOBIC COATINGS, MICROSPHERES AND PLASTIC EXPLOSIVES

BY

NITIN KRISHNA NEELAKANTAN

DISSERTATION

Submitted in partial fulfillment of the requirements
for the degree of Doctor of Philosophy in Chemistry
in the Graduate College of the
University of Illinois at Urbana-Champaign, 2017

Urbana, Illinois

Doctoral Committee:

Professor Kenneth S. Suslick, Chair
Professor Dana D. Dlott
Professor Catherine J. Murphy
Assistant Professor David W. Flaherty

ABSTRACT

Silicones are ubiquitous polymers containing a silicon-oxygen backbone and a variety of functional groups that can be tailored to very specific applications. Their flexibility, biocompatibility and relative inertness make them the ideal choice in materials as diverse as cosmetics, defoaming agents in food and medical implants. This thesis will focus on three separate projects, each one a silicone-based composite. Chapter 1 is an overview that includes a brief history, background, synthesis, applications, chemical structure, and any other relevant information regarding silicones.

Chapter 2 describes the successful fabrication of a sprayable omniphobic coating that contains a polydimethylsiloxane binder and nanoparticle ZnO. A coating, or any other surface, is considered omniphobic if it is both water-repellent (i.e. hydrophobic) and oil-repellant (i.e. oleophobic). The coating herein was sprayed on a variety of different surfaces, such as metal mesh, filter paper and bare aluminum, rending them resistant to liquid contamination. The desired application of this coating is to promote efficient heat transfer in condensing pipes by preventing insulating oily films from forming on their interior. By keeping the surface free of films, more heat may be available for transport to the ambient environment.

Chapter 3 describes the synthesis of silicone microspheres via ultrasonic spray pyrolysis. A viable route to silicone microspheres has eluded researchers for many years, in large part due to the very low surface energy of silicone polymers. This prevents a simple emulsion route; the surface energy promotes agglomeration, a problem which cannot be combatted effectively by common surfactants. Microfluidic devices are expensive and afford only low yield and even lower throughput. Thus, we have developed a simple route which nebulizes silicone precursors

into micron-sized aerosol droplets and flows the droplets through a furnace tube, where curing and solvent evaporation take place. Since each droplet is its own micro-reactor, each produces a well-formed microsphere with ano observable agglomeration. Furthermore, we can tune the size and composition of these microspheres simply by altering the concentration and components of the precursor.

Chapter 4 describes a series of experiments on silicone-based plastic explosives. There is a paucity of literature regarding the controlled shock impact and subsequent detonation of commonly used explosives. What reports exist rely on computer-modelling and idealized assumptions to make conclusions about the thermomechanical and chemical nature of these events. When an actual explosive is used, it is often loosely packed powder which is of low density and contains many pores and defects. We have devised a method that uses mild-impact sources to generate explosions in a very small amount of explosive material. We incorporate instrumentation that allows us to see, with nanosecond resolution, the temperature and spectral emission of this explosive, under real-life impact conditions.

ACKNOWLEDGEMENTS

This thesis would not have been possible without contributions from a number of sources that, as many of whom I can remember, I would like to cite here. First and foremost is my advisor, Professor Ken Suslick: thank you for all of your support, input, advice and patience, for instilling in me a passion to do science and for letting me pursue my research interests independently. Your guidance was the reason for my success as a graduate student. I would like to also thank my thesis committee, Cathy Murphy, Greg Girolami and David Flaherty, as their suggestions shaped this thesis. I would also like to thank Bill King and Dana Dlott for their collaborations.

Thank you to all my collaborators: Jackie Rankin, John Overcash, Sizhu You, Patricia Weisensee, Will Bassett and Eduardo Torrealba. It was a profoundly educational experience working with you; I am honored to have the privilege of saying you were my colleagues and/or co-authors. We did some great science together, and I know you are all continuing to do great science! Thank you to all of the Suslick group members I have known throughout the years (in no order): Maria LaGasse, Yinan Zhang, John Sander, Jon Askim, Jinrui Guo, Maryam Sayyah, Zhi Su, Alberto Comazzi, Yurun Miao, Zheng Li, Hyo Na Kim, Jordan Hinman, Sam Fuchs and Kimberly Lundberg. You guys made grad school something I will never regret nor forget.

I would like to next thank the staff at the School of Chemical Sciences, all of whom have displayed the utmost professionalism and diligence in their respective occupations. A warm thank you to the IMP office: Connie Knight, Karen Watson, Theresa Struss, Beth Myler and Stacy Dudzinski. A cup of coffee and idle conversation there cured the many grad school afflictions I faced such as stress and generalized panic. A warm thank you to the machine shop:

Michael ‘Hodge’ Harland, Rob Brown, Brad Lutz, et. al. If it was broken, you could and did fix it. A warm thank you to the electrical shop: Kyle Webb and Kyle Kroha. You miraculously found the last gasket on Earth that fits our vacuum oven. A warm thank you to the staff scientists at MRL and Noyes: Honghui Zhou, Wacek Swiech, Jim Mabon, Rick Haasch, Steve Burdin, Tim Spila, Elizabeth Eves, Ratna Dutta, Rudy Laufhutte et. al. for teaching me how to use scientific instrumentation and for helping me acquire the data presented in this thesis.

Thank you to my friends, whether made here at Illinois, back home or scattered far across the corners of the world for the times we shared, the memories made and the ones still to come.

Finally, I would like to thank my mother, my father and my sister. You raised me to be who I am today. You always believed I could do great things and you were always there for me. This thesis is dedicated to you.

TABLE OF CONTENTS

CHAPTER 1: SILICONES: BACKGROUND, SYNTHESIS AND APPLICATIONS

Silicones are polymers that have repeat units of substituted silicon-oxygen bonds. The most widely used silicone is polydimethylsiloxane (PDMS). Its properties, such as biocompatibility, flexibility, transparency, gas permeability and chemical resistance make it the ideal material in a variety of applications such as medical devices, implants, microfluidic channels, food additives and lubricating oils.[1-6] This chapter will include an overview of the chemical structure and properties of silicones, their industrial production, and the most relevant silicone-based materials.

1.1 Background

The word 'silicone' is derived from an analogy to ketones, which contain a similar structure with a carbon center instead of a silicon center. The generalized chemical formula is shown in **Figure 1.1**, with R groups corresponding to simple alkyl groups, alkoxy groups, hydride groups, vinyl groups, fluoroalkyl groups, and phenyl groups among others (**Figure 1.2a-f**). While the formula shown is of a linear nature, there are many possibilities for branching and cross-linking, as will be demonstrated in the synthesis section of this chapter.

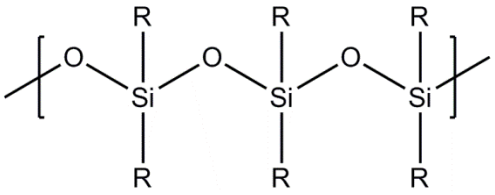

Figure 1.1 Generic structure of silicone backbone.

The most commonly used and widely available polymer in the silicone family is polydimethylsiloxane (i.e., PDMS, **Figure 1.2a**). The polymer used in the bulk of the research that encompasses this thesis is PDMS, thus, the bulk of this chapter will focus on the production and applications of PDMS.

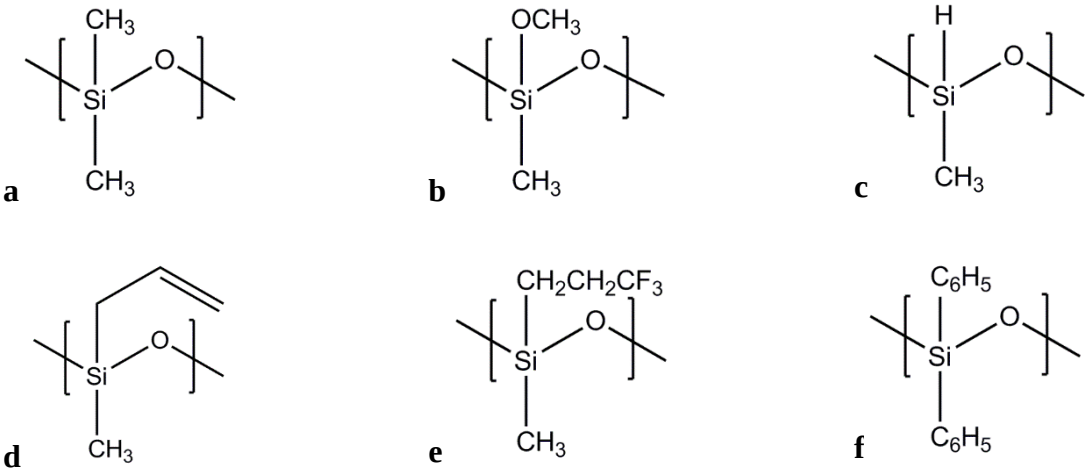

Figure 1.2 Examples of PDMS (a) and a variety of substituents from (b) alkoxy-, (c) hydride-, (d) vinyl, (e) trifluoropropyl- and (f) phenylsiloxanes.

A siloxane unit, which refers to the monomer from which the polymer is derived, can then be considered to have one of the following formulas and corresponding functionalities: mono-, di-, tri- or tetrafunctional, (M, D, T and Q respectively). **Table 1.1** on the following page gives an overview of the chemical nature of each of these starting siloxanes.

Table 1.1 Origin, functionality, and fields of application of silicone structural units[7]

Starting compound	Structural unit		Application
	Symbol	Functionality	
$(CH_3)_3SiCl$ Monochloro-trimethylsilane	M	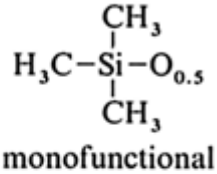 monofunctional	chain end in silicone fluids, trimethylsilyl protecting groups
$(CH_3)_2SiCl_2$ Dichlorodi-methylsilane	D	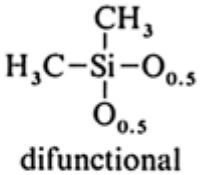 difunctional	linear siloxane polymers, silicone fluids, rubbers, elastomers
CH_3SiCl_3 Trichloro-methylsilane	T	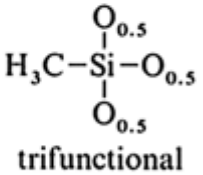 trifunctional	silicone resins for paints, impregnating agents, masonry protection
$SiCl_4$ Tetrachloro-silane	Q	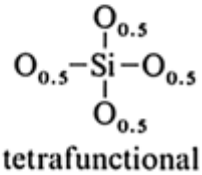 tetrafunctional	silicone resins

It is the ability to combine multiple siloxane functionalities that gives rise to a near infinite combination of co-polymers with distinct reactivity, thermal properties, chemical properties and physical resistance.[8] For instance, simply polymerizing a trifunctional (T) monomer, the cage structures are the most commonly synthesized product (**Figure 1.3**), and not a linear chain, as may be expected with carbon-based analogs.

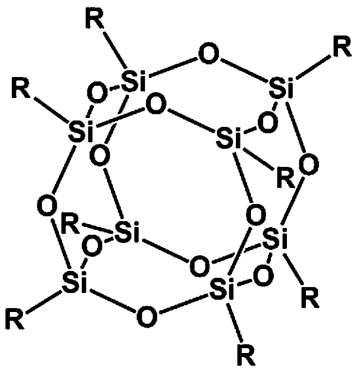

Figure 1.3 A polyhedral organic silsesquioxane, formed by polymerizing a type T monomer.[9]

1.2 The Origin of Silicones

The history of silicone synthesis begins in 1824,[10] with the reduction of potassium silicon hexafluoride to neutral silicon.

$$4\ K + K_2SiF_6 \rightarrow Si + 6\ KF$$

Upon reaction with chlorine gas, silicon tetrachloride is formed.

$$Si + 2\ Cl_2 \rightarrow SiCl_4$$

Years later in 1863, Friedel and Crafts[11] were able to convert silicon tetrachloride in to tetraethylsilane, by using diethylzinc as an alkylating agent, the first example of an organosilane compound.

$$2\ Zn(C_2H_5)_2 + SiCl_4 \rightarrow Si(C_2H_5)_4 + 2\ ZnCl_2$$

The next advance came in 1901 with the work Frederic Stanley Kipping, who is often referred to as the father of organosilicon chemistry. Much of his research entailed the use of Grignard reagents to prepare halogenated organosilanes. Upon the heat-catalyzed condensation of a

phenyl-derived monomer, he describes a ‘vitreous yellow mass’ named diphenyl *silicone*, which coined the term.[12]

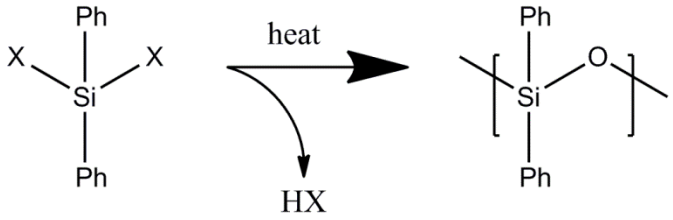

Figure 1.4 Possible reaction discovered by Kipping, where Ph = Phenyl and X = OH, Cl.

While we do not know for certain, he may have obtained the product in **Figure 1.4**, which has the same stoichiometric formula and properties as described by him and his colleagues.

All the previously described methods entailed laboratory scale syntheses which did not lend themselves to industrial viability. It was not until Rochow, et. al. developed a process for directly making halogenated organosilanes using elemental Si and alkyl chlorides as shown below.[13]

$$x\ MeCl + Si \rightarrow Me_3SiCl,\ Me_2SiCl_2,\ MeSiCl_3$$

In the reaction above, methyl chloride is reacted with fine Si particles in a sealed vessel at 250-350 C with a copper catalyst. The temperature and conditions can be optimized to give the desired value of n, which is generally 2, in industrial manufacture. No matter what conditions are selected, a mixture of all possible products is obtained, and distillation, fractionation and other processes are generally required to separate the products.[14]

Upon isolation of dichlorodimethylsilane, hydrolysis can be used to generate polysiloxane products.[15]

$$m(CH_3)_2SiCl_2 + (m+1)H_2O \rightarrow HO[(CH_3)_2SiO]_mH + 2mHCl$$

$$n(CH_3)_2SiCl_2 + nH_2O \rightarrow [(CH_3)_2SiO]_n + 2nHCl$$

The chloride group is replaced by a hydroxyl group, yielding linear (m = ~50) and cylic oligomeric dimethylsiloxanes (n = 3,4,5). HCl is recovered as a byproduct. As in the production of dichlorodimethylsilane, the temperature and reaction conditions can influence the yield of the products obtained. The cyclic product is mostly the 4-membered ring, octamethyltetracyclosiloxane, and it can also under go base-catalyzed ring-opening to produce linear hydroxyl-terminated PDMS, after post-treatment stripping and neutralization.

$$x\ (Me_2SiO)_4 + KOH \rightarrow (Me_2SiO)_y + KO(Me_2SiO)_zH$$

$$KO(Me_2SiO)_zH \rightarrow HO(Me_2SiO)_zH + KOH$$

Unlike many of the carbon based polymers, which become solids and plastics of varying rigidity dependent on their chain-length, linear PDMS is never a solid. The shortest polysiloxanes are liquids, and as the chain length increases, the viscosity increases, i.e., long chains of linear PDMS are merely viscous oils. Shown below (**Table 1.2**) is the relationship between viscosity and molecular weight.

Table 1.2 Linear polysiloxane Molecular weight vs. Viscosity[4]

Molecular Weight (g/mol)	3,600	17,000	30,000	88,000	143,000
Viscosity (cSt)	60	440	1,440	50,000	300,000

1.3 Synthesis of Industrially Relevant Oligomers and Polymers

1.3.1 Synthesis of Silicone Oligomers

A variety of silicone oligomers can be made from their chlorinated precursors, giving rise to synthetic routes which yield silicones with diverse properties. Silicones can be polymerized via condensation, hydrosilylation, dehydrogenative coupling, peroxidation and UV curing. This section will cover how each of these oligomers is produced. The following section will cover how their polymers are produced.

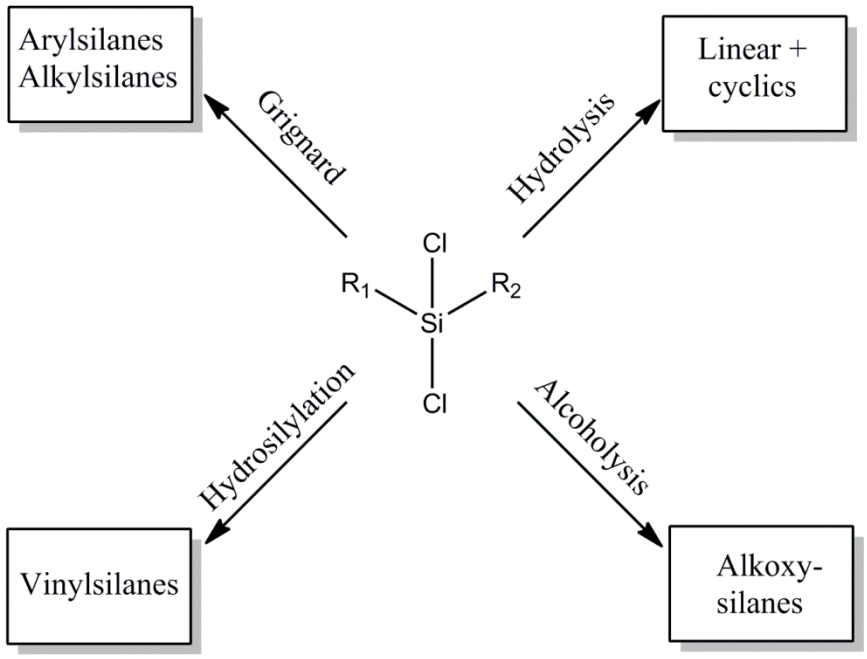

Figure 1.5 Relevant Reactions of chlorosilane monomers (R_1 and R_2 = H or CH_3).

Figure 1.5 above shows the synthetic routes to some common oligomers. Silicones that are made by condensation proceed from alkoxy-monomers and oligomers. These can be readily produced by reacting chlorosilanes with an alcohol. Methanolysis of dimethyldichlorosilane, for example, produces dimethoxydimethylsilane, an important precursor.[16]

$$m(CH_3)_2SiCl_2 + 2mCH_3OH \rightarrow HO[(CH_3)_2SiO]_mH + 2mCH_3Cl + mH_2O$$

$$n(CH_3)_2SiCl_2 + 2nCH_3OH \rightarrow [(CH_3)_2SiO]_n + 2nCH_3Cl + nH_2O$$

Condensation reactions can be carried out using alkoxy-silanes in much the same way as their chlorinated analogues. Acid or base catalyzed hydrolysis and subsequent condensation[17] yields the same products as shown on page 5 (*m* and *n* also have the same values). Alkoxy-silanes exhibit slower reactivity than chlorosilanes, and the rate of reactivity for all silanes follows the general trend of Cl > MeO > EtO.

$MeHSiCl_2$, a product of the Rochow process as shown in **Table 1.1**, is also a very important precursor to platinum-catalyzed silicones, which are perhaps the most widely used silicone product and most widely used in this thesis. It can be polymerized into polymethylhydrosiloxane (PMHS) (**Figure 1.2c**), a cross-linking agent for Pt-cured PDMS. $MeHSiCl_2$ is also reacted with acetylene to introduce vinyl-groups (Vi) via hydrosilylation.[18]

$$MeHSiCl_2 + HC{\equiv}CH \rightarrow MeViSiCl_2$$

The Pt catalyst employed in hydrosilylation reactions has the following structure.

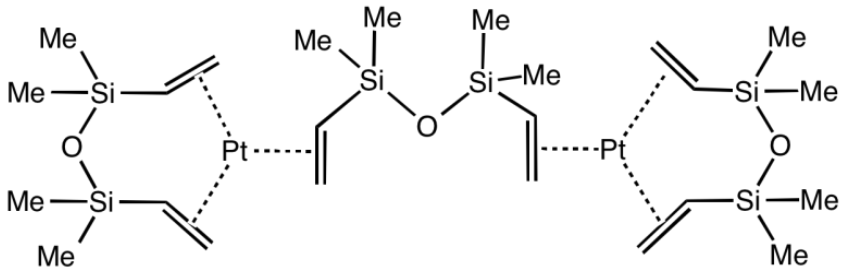

Figure 1.6 Platinum divinyltetramethylosiloxane, which is six-coordinate Pt (0) complex bound by three siloxane units.

This catalyst was first discovered by Karstedt in 1973[19] and is still used today in 2-part room-temperature vulcanizing (RTV) silicones.[20, 21]

1.3.2 Platinum-Catalyzed Polymerization of PDMS

The silicone that is most prevalently used in this thesis is Pt-cured PDMS. The basic catalytic scheme that governs its synthesis is shown below, in which the hydride group of one silicone chain forms a bond with the vinyl group of another silicone chain via addition.

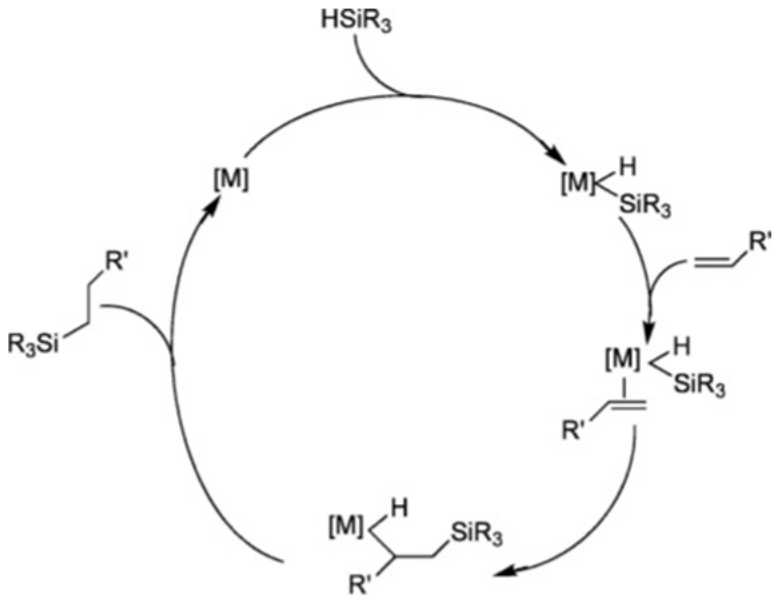

Figure 1.7 Chalk-Harrod catalytic cycle for hydrosilylation of vinyl silanes with hydrosilanes using a Pt catalyst.[22]

This idealized mechanism, first proposed by Chalk and Harrod in 1965,[23] can be described as such. A trisubstituted silyl hydride undergoes oxidative addition with the metal catalyst center. Then, a vinyl-substituted silane couples with the metal center, and the hydride group shifts to the

vinyl group in a migratory insertion step. Finally, the Si-C bond is formed via reductive elimination.

As is the case with condensation reactions, linear products of Pt-cured PDMS are merely oils of varying viscosities. A crosslinked 3-dimensional network is necessary for obtaining a solid elastomeric product. Dichloromethylhydrosilane can be polymerized into polymethylhydrosiloxane (PMHS), while the corresponding vinyl monomer can be polymerized into polymethylvinylsiloxane (PMVS). It is these two polymers which can then be crosslinked into the elastomer, as shown in the reaction below.

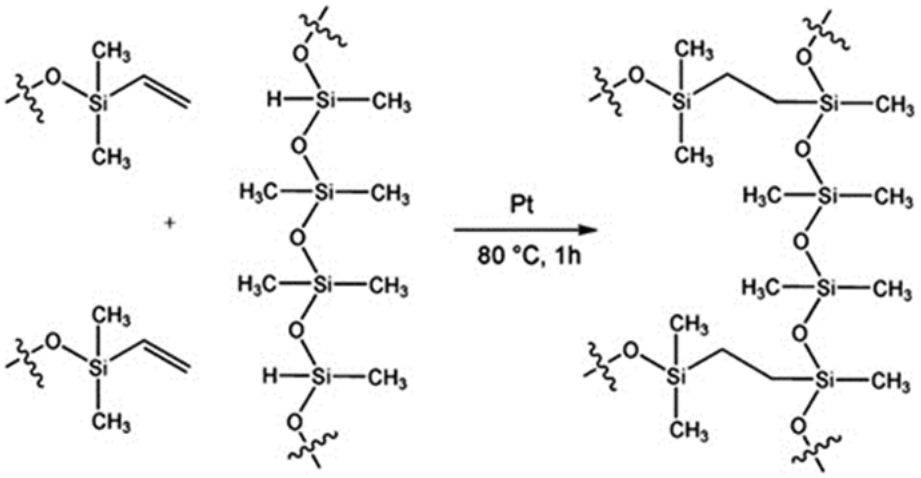

Figure 1.8 Pt-catalyzed crosslinking of two vinyl-PDMS chains and a PMHS-PDMS copolymer.[24]

Commercially available 2-part cures of this type include PMHS and PMVS, but also block copolymers of PMHS-PDMS and PMVS-PDMS, with the mole % of the reactive hydride and vinyl functionalities ranging from 1-50. The relative ratio of the two polymers used in the cure affects the swelling properties and flexibility of the resultant product. More details on the properties of silicone elastomers will be discussed in a later section.

1.3.3 Tin-Catalyzed Polymerization of PDMS

Another route to PDMS involves the dehydrogenative coupling of a hydroxyl-terminated silicone with a hydride-terminated silicone (**Figure 1.9**), which forms a Si-O-Si linkage, along with hydrogen gas as a byproduct. This is in contrast to Pt catalysts, which form Si-C bonds.[25, 26]

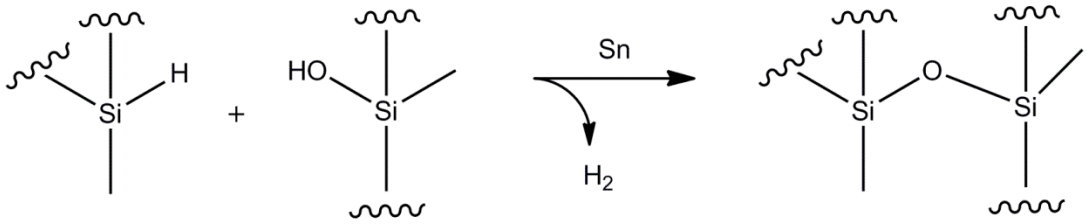

Figure 1.9 Dehydrogenative coupling catalyzed by an organotin salt. Wavy lines are a truncation of the rest of the polymer chain.

Typical catalysts used in this type of cure are tin octanoate and dibutyltin dilaurate, as shown in

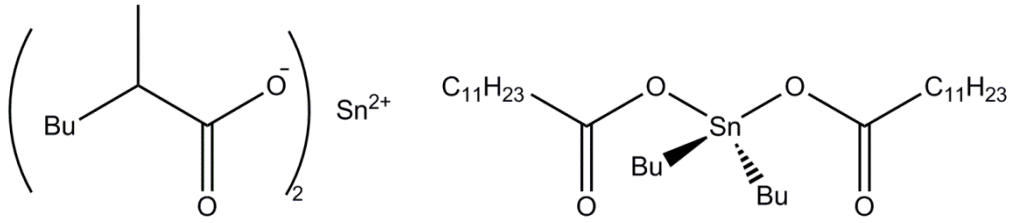

Figure 1.10 The chemical structure of tin octanoate (left) and dibutyltin dilaurate (right), important catalysts in PDMS production.

The organotin salts will also catalyze the crosslinking of a hydroxyl-terminated PDMS with a multi-substituted alkoxy monomer, such as tetraethyl orthosilicate (TEOS). It is important to note that the following reaction (**Figure 1.11**) is a simplification which ignores the hydrolysis of TEOS as a necessary step; this is evidenced by the fact that the reaction requires moisture to proceed.[27]

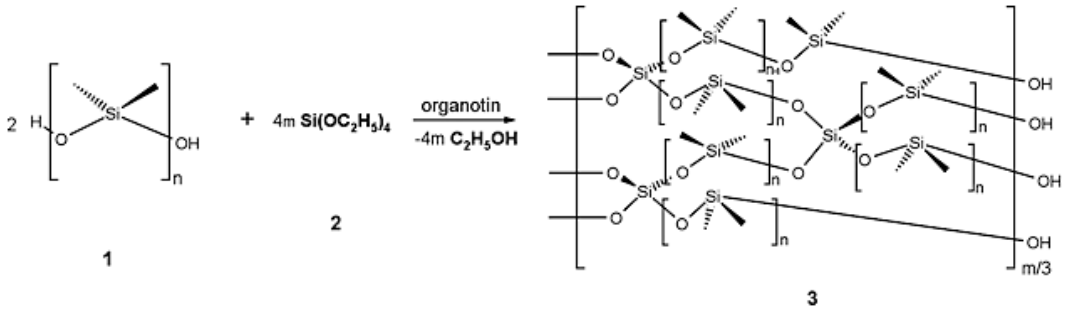

Figure 1.11 Hydroxyl-terminated PDMS (1) crosslinks with TEOS (2) to generate a crosslinked product (3) and ethanol.

Unlike Pt catalysts, which can be used at concentrations as low as 1.5 ppm, tin catalysts must be used at fairly high concentrations of >50 ppm. Thus, concerns of toxicity and adverse reaction have precluded their widespread use in biological and medical applications. Secondly, because alcohol is a byproduct of the reaction, some shrinkage of the final product can be expected, precluding the fabrication of precise objects; this is not so with Pt-catalyzed PDMS. Moreover, while the mechanism for Pt-catalyzed PDMS has been generally understood, the mechanism for Sn-catalyzed pathways has been a source of contention for many years. It is, however, accepted that hydrolysis of the catalyst and Sn-O-Si formation occur as shown in **Figure 1.12**. Severnyi and van der Weij pioneered studies regarding these pathways.[28, 29]

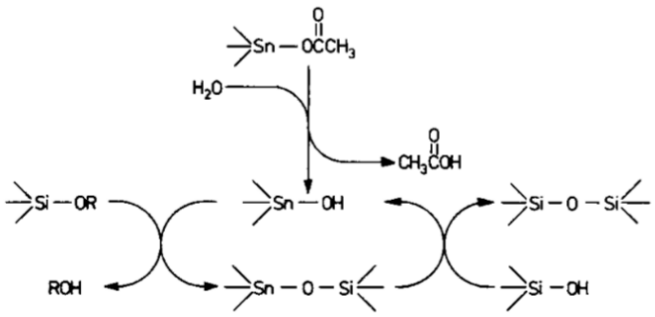

Figure 1.12 Hydrolysis of tin catalyst, formation of Sn-O-Si linkage and polymerization of a siloxane unit.[29]

Tin catalysis also plays the same role in one-part RTV cures, in which all of the reactive species are combined in a vessel and sold as uncured reactants. This is made possible by the fact that tin catalysts do not react under anhydrous conditions. Such PDMS precursors generally contain acetoxy-functionalized prepolymers, which crosslink in the presence of moisture, as described by the following reaction.[25]

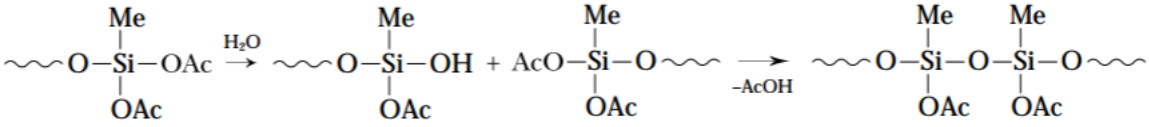

Figure 1.13 Reaction pathway for an acetoxy-cured PDMS. OAc = CH_3COO group. Wavy lines are a truncation of the rest of the polymer chain.[2]

1.3.4 Peroxide and UV Cure

While industrially important, these types of silicones are not used in this thesis, and so will only be briefly discussed. Peroxide cured silicone involves the coupling of a methyl group on one silicone chain to the vinyl group on an adjacent chain, as shown in Figure 1.x. This is generally accomplished by combining high molecular weight (upwards of 500,000) polyvinylmethylsiloxane-polydimethylsiloxane copolymers with an appropriate peroxide at a loading of 0.2-1.0%.[30, 31] These cures require heat so the reaction is carried out at ~130 degrees Celsius. UV cured silicones utilize epoxide and acrylate functionalities which are radicalized and polymerized in the presence of a photoinitiator.

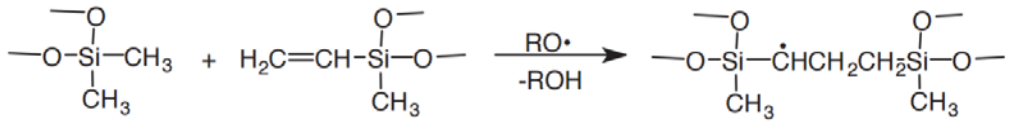

Figure 1.14 Radical polymerization pathway. Vinyl-terminated oligomer reacts with methyl-terminated oligomer, extending the radical chain.[32]

1.4 Properties of Bulk Silicone

As mentioned in the abstract, silicones have properties that are widely desirable for a variety of applications. This section will briefly discuss those properties and their importance. **Table 1.3** shows the various thermal, electrical, rheological and chemical properties of bulk PDMS. A majority of these properties are values given for Dow Sylgard (Dow Corning, Inc.). Sylgard is a commercially available 2-part RTV silicone that was used for a majority of this thesis. Its major constituent is cross-linkable PDMS elastomer, thus it will be used to represent the properties typically found in bulk PDMS.

Table 1.3 General properties of a Silicone Elastomer[34-36]

Property	Value
Density	1.03 g/cm^3
Glass Transition Temperature (T_g)	146 K
Rotation Energy	13.3 kJ/mol
Critical Wetting Energy	24 mN/m
Dielectric Strength	500 kV/mm
Thermal Conductivity	0.27 W/mK
Gas permeability	600-800 Barrer
Resistivity	2.9 x 10^{14} ohm*cm
Refractive Index	1.42
Tensile Strength	6.7 MPa

Polydimethylsiloxane (PDMS) is interesting because it contains both polar Si-O bonds, and highly non-polar methyl groups. In addition, the energy barrier to rotation around a Me_2Si-O group is only 3.3 kJ/mol. Organic polymers such as polyethylene may have a rotational energy of over 13 kJ/mol. Thus, depending on the environment, PDMS may adopt many more configurations than carbon based polymers. Indeed, PDMS can be easily molded into various shapes and it exhibits excellent adhesion depending on the interface to which it is fixed. To elaborate, because there is a low energy cost to changing its orientation, there is greater opportunity for favorable interactions, i.e., between a polar surface and the polar Si-O bonds, and between a non-polar surface and the non-polar methyl groups. PDMS has a glass transition temperature far lower than any hydrocarbon polymer; this gives a very broad working temperature range for PDMS (-50 to 150 °C).

1.4.1 Surface Properties

Exposed to air, PDMS will generally orient its methyl groups towards the surface to minimize surface tension, since air can be considered non-polar. This is in sharp contrast to a rigid polymer, which would have a fixed orientation and correspondingly higher surface energy as a result. As **Table 1.4** shows, at ~20 mN/m, PDMS have the lowest surface energy of almost all known polymers, comparable to that of polytetrafluoroethylene. The surface energy of PDMS is so low that it is less than its own critical surface tension of wetting, meaning that it can evenly coat itself and form good films. The low surface energy and facile film formation of PDMS ensure that it is an ideal material for protecting surfaces and preventing penetration by liquid water and some other liquids. By contrast, PDMS also has high oxygen permeability and water vapor permeability, which means that PDMS coatings will have some degree of breathability.

Table 1.4 Surface Tensions of Common Polymers[37, 38]

Polymer	**Surface Tension (mN/m)**
Polytetrafluoroethylene (PTFE)	19.4
Polydimethylsiloxane (PDMS)	20.1
Polytrifluoroethylene	26.5
Polyisobutylene (PIB, butyl rubber)	27
Polybutadiene	29.3
Poly *n*-butyl methacrylate (PnBMA)	29.8
Polypropylene (PP)	30.5
Polychlorotrifluoroethylene (PCTFE)	30.8
Polyethylene (PE)	31.6
Polyvinylidene fluoride (PVDF)	31.6
Nylon 10,10	32
Polyvinyl fluoride (PVF)	32.7
Nylon 8,8	34
Nylon 9,9	34
Polystyrene (PS)	34
Polyvinyl acetate (PVA)	35.3
Nylon 11	35.6
Polyvinyl alcohol (PVOH)	37
Nylon 12	37.1
Polymethyl methacrylate (PMMA)	37.5
Polyvinyl chloride (PVC)	37.9
Polyphenylene sulfide (PPS)	38
Acrylonitrile butadiene styrene (ABS)	38.5
Polyethylene terephthalate (PET)	39
Polyvinylidene chloride (PVDC, Saran)	40.2
Polysulfone (PSU)	42.1
Nylon 6,6	42.2
Nylon 7,7	43
Polyethylene oxide (PEO, PEG)	43
Nylon 6 (polycaprolactum, aramid 6)	43.9
Polycarbonate (PC)	44
Epoxies	44.5

1.4.2 Bond Enthalpy of Silicones

It is also useful to examine the enthalpy of each of the bonds in PDMS, and in particular, to compare them to bond enthalpies in other polymers. As **Table 1.5** shows, a silicon-oxygen bond, has a bond enthalpy of 110 kcal/mol. This is ~25 kcal/mol higher than that of a carbon-

oxygen single bond. The strength of the Si-O backbone may partially explain PDMS's resistance to chemical attack. Indeed, only very strong acids such as conc. sulfuric acid can "unzip" the polymer chain by breaking this bond. Even then, this process has been shown to take several days in some instances.

Table 1.5 Bond enthalpies for bonds commonly found in polymers [39, 40]

Bond Type	Bond Enthalpy (kcal/mol)
C-C	83
C-H	99
C-O	84
C=O	171
C-N	70
C-F	116
Si-C	69
Si-O	110

On the other hand, C-Si single bonds are weaker than the C-C single bonds present in polyethylene, polypropylene, etc. This gives PDMS another useful property, which is that it can be plasma etched. The methyl groups on the surface can be replaced with silanol groups, rendering the surface highly hydrophilic.[41-43] It also allows for the surface functionalization of PDMS, or if necessary, grafting of PDMS to another polar surface such as glass or another polymer.[44-46]

1.4.3 Swelling Properties and Solvent Compatibility

Of incredible importance to all polymers, but especially PDMS, is their behavior when in contact with liquids. As is expected, PDMS has low affinity for water and the more polar

alcohols due to its surface chemistry being dominated by the methyl groups. It follows that PDMS should have high affinity for hydrocarbons and oils. Depending on a solvent's properties, it might penetrate the crosslinked PDMS matrix, provided that the solvent has some degree of solubility in PDMS.[47-49] If penetration does occur, it may also result in a degree of swelling, since the crosslinked matrix of PDMS must expand to accommodate the solvent molecule. The energy required to separate the PDMS chains so that the solvent molecule may penetrate is described by the following equation:

$$-\frac{U}{V} = c$$

In which *U* is the internal molar energy of PDMS, *V* is the molar volume of PDMS and *c* is the cohesive energy density. Using this term, Hildebrand and Scatchard then developed an equation[50] which governs the solubility of two non-polar liquids by relating the enthalpy change that occurs upon their mixture (subscript p is for PDMS, s is for solvent):

$$\Delta H_m = V_m(\delta_p - \delta_s)^2 \varphi_p \varphi_s$$

Given that $\delta = c^{\frac{1}{2}}$. δ is commonly referred to as the Hildebrand value or the solubility parameter. ΔH_m is the enthalpy of mixture, V_m is the volume of the mixture, and φ is the volume fraction of the component. Since

$$1)\ \Delta G_m = \Delta H_m - T\Delta S_m$$

$$2)\ \Delta H_m \propto (\delta_p - \delta_s)^2$$

ΔG_m is favored when ΔH_m is zero. The implication is then that solubility is maximized when $\delta_p = \delta_s$. This is intuitive since it means there is no enthalpic cost to the molecular exchange of solvent p into solvent s, or in the case of PDMS, to the penetration of the solvent into the matrix.

In 2003, Whitesides et. al. quantified the swelling properties and solvent compatibility of PDMS by immersing a small slab of the polymer (with known dimensions) into a variety of solvents.[51] By measuring the volumetric change of the PDMS slab, they were able to determine the degree to which the chosen solvent had swollen the PDMS. Since swelling and solubility are correlated, they could then statistically determine a "solubility ratio" S, which they define as

$$S = \frac{D}{D_0}$$

in which D is the swollen length of the PDMS slab, and D_0 is the unswollen length. A truncated table of values for the solubility ratio, solubility parameter and dipole moments for various solvents is given in **Table 1.6**.

Table 1.6 Solubility Parameters, Swelling Ratios, and Dipole Moments of Various Solvents Used in Organic Synthesis[51]

Solvent	**δ**	***S***	**μ (D)**
perfluorotributylamine	5.6	1.00	0.0
perfluorodecalin	6.6	1.00	0.0
pentane	7.1	1.44	0.0
poly(dimethylsiloxane)	7.3	∞	0.6−0.9
diisopropylamine	7.3	2.13	1.2
hexanes	7.3	1.35	0.0
n-heptane	7.4	1.34	0.0
triethylamine	7.5	1.58	0.7
ether	7.5	1.38	1.1
cyclohexane	8.2	1.33	0.0
trichloroethylene	9.2	1.34	0.9
dimethoxyethane (DME)	8.8	1.32	1.6
xylenes	8.9	1.41	0.3
toluene	8.9	1.31	0.4
ethyl acetate	9.0	1.18	1.8
benzene	9.2	1.28	0.0
chloroform	9.2	1.39	1.0
methylene chloride	9.9	1.22	1.6
acetone	9.9	1.06	2.9
ethyl alcohol	12.7	1.04	1.7
methanol	14.5	1.02	1.7
water	23.4	1.00	1.9

As a general trend, it appears that non-polar solvents swell PDMS to a greater degree than polar solvents, though the amines are an outlier. This may be due to favorable interactions between the polar nitrogen component and the polar Si-O bonds in addition to the favorable interactions between the alkyl groups on both compounds; most solvents only have a non-polar or a polar moiety. Its dipole moment is also fairly modest compared to acetone and water. In addition to a table, a semi-log plot of solubility parameter to swelling ratio is provided as shown below.

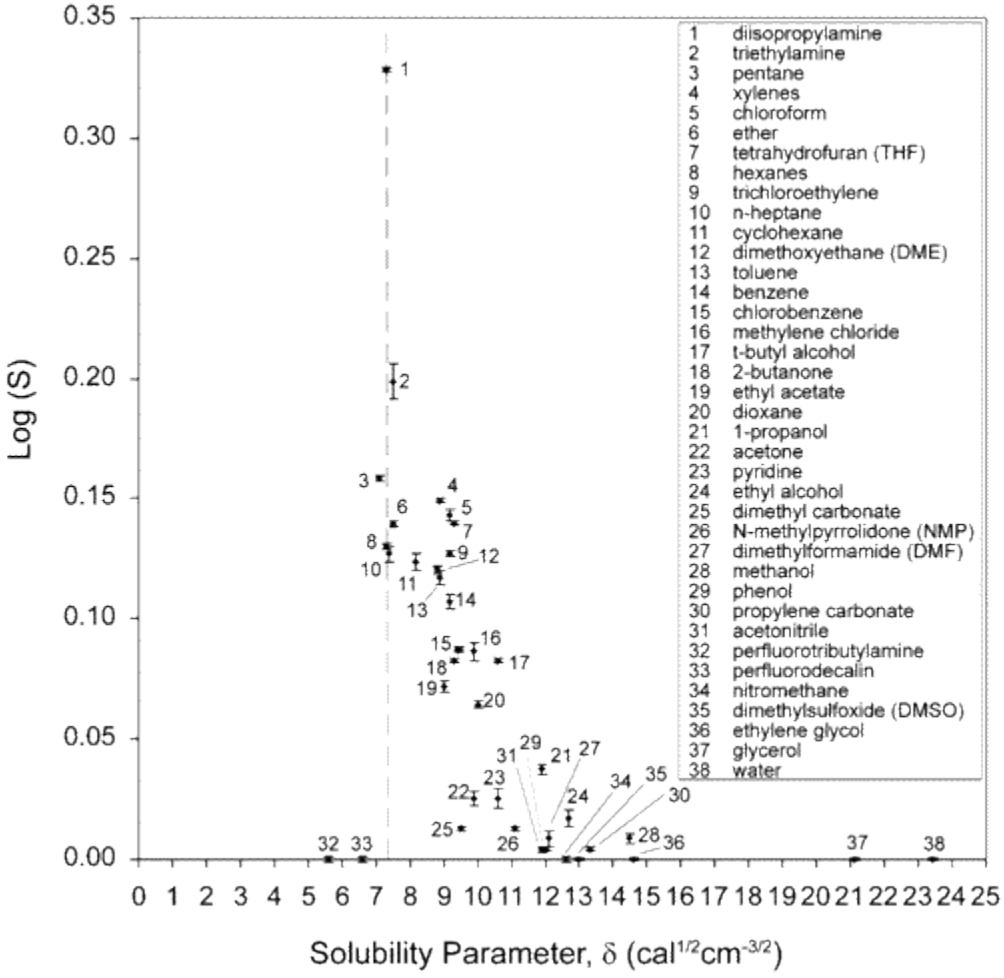

Figure 1.15 Correlation between solubility parameter and swelling. Solvents are ranked from 1 (most swelling) to 38 (least swelling). The closer the solubility parameter is to that of PDMS, the greater the swelling.[51]

As is expected, both solubility and swelling increase as the solubility parameter of the solvent approaches that of PDMS, highlighted by the dashed line in **Figure 1.15**. Perfluorodecalin and perfluorotributylamine appear to be outliers, but their inability to swell PDMS makes sense. The C-F bonds in these solvents have almost no van der Waals forces, due to the strongly electronegative fluorine atom. As a result, they are completely immiscible with PDMS and interact very weakly with PDMS.

1.4.4 Effects of Cross-Linking on Swelling Properties

The results obtained by Whitesides, et al. only apply to the specific composition of the PDMS they used. It should be of no surprise that the cross-linking density has a profound effect on the ability of the PDMS matrix to accommodate a solvent molecule. A denser matrix, after all, will give fewer opportunities for a solvent molecule to penetrate and consequently decrease the amount of swelling that the PDMS undergoes.

Flory and Rehner[52] quantified the relationship between crosslinking density of a polymer the swelling of that polymer in a solvent through the following equation:

$$M_c = \frac{-\rho V_1 v_2^{1/3}}{-X v_2 + \ln(1 - v_2) + v_2}$$

Where M_c is the molecular weight between two crosslinks, ρ is the density of PDMS, V_1 is the molar volume of the solvent, v_2 is the volume fraction of PDMS in the polymer-solvent complex, and X is the interaction parameter between PDMS and the solvent. The interaction parameter is derived from the idealized mixing of polymer and solvent by modelling the polymer as a lattice which has “sites” available for interaction.

1.5 Applications of Silicones

Whether they are in the form of oils, elastomers, pastes, resins, gums, etc., silicones are ubiquitous in industrial, household and medical products. This section will present a broad overview of silicone products, as well as composites and formulations that make prominent use of silicones. The introduction of silicone to the modern industrial world begins with the work of James Franklin Hyde, who in the 1940s noticed that the polymer had a remarkably high electrical resistance and thermal stability. While at Corning Glass Works, he was able to formulate a silicone composite for insulation in motors and aeronautical equipment.[53, 54] Since then, a variety of commercial products have been developed. **Figure 1.16** shows some of the most common industrial applications for silicones, which will be discussed in detail in the following section.

Figure 1.16 Silicone as industrial tubing*, vacuum grease*, wire insulation* (* = public domain) and antifoaming agent (® Mirachem, LLC).

1.5.1 Silicones in Industry

The high temperature stability and low toxicity of silicone make them the material of choice in a number of industries.[55] Silicone oils, which are linear-chain polymers of varying length and viscosity, find application as lubricants in the food processing industry due to their compatibility with bearings, plastic and rubber parts as well as metallic gears.[56] In the textile industry, spinnerets must maintain high rpm without wear or tear in order to produce fibers at high production capacity.[57, 58] Silicone oil is used as a lubricant here as well, due to its thermal properties. In the automotive and chemical industries, silica-thickened PDMS finds use as vacuum grease, with the ability to form airtight connections between joints and other components.[59, 60]

In food/beverage processing, as well as pulp and paper processing, a large amount of foam is generated. The generation of foam reduces the efficiency with which the manufacturing process can proceed, therefore it is undesirable. For instance, foam that arises during the delignification of pulp[61] can cause overflows and present hazards, due to the fumes of the harsh chemicals that are used. Fermentation in food and beverages produces a large amount of foam, due to various gaseous byproducts.[62] In both these cases, silicone finds use as an anti-foaming agent. The exact composition will vary from depending on the nature of the foam, but generally the anti-foaming agent is silicone oil in which hydrophobic particles are dispersed.[63] These have the ability to destabilize foams[64] due to the low surface tension of the silicone.[65] **Figure 1.17** shows a simplified schematic of how the anti-foaming process is thought to work.[66]

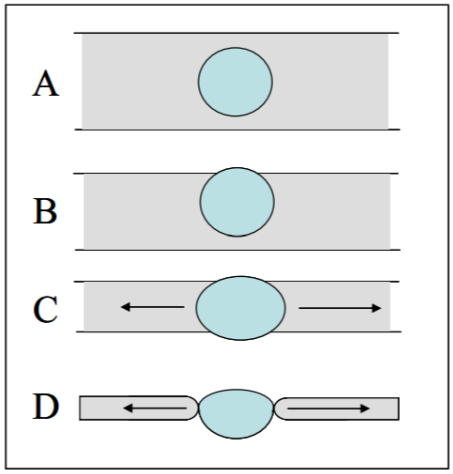

Figure 1.17 Animated representation of the de-foaming process with an idealized spherical antifoam droplet (blue) immersed in a film (gray).[67]

Initially, the anti-foaming droplet is suspended in a foam film (A), but due to its lower surface tension migrates to the surface (B). Once the droplet forms an interface with the surrounding air, it also bridges the foam film (C). Finally, the foam film begins the de-wetting process as it is energetically unfavorable for it to interact with the anti-foaming agent (D). This initiates rupturing of the foam film.[67]

In construction, ideal sealants and adhesives should have a number of optimal parameters. Chief among these are thermal stability, chemical resistance, UV resistance, flexibility and high gas permeability. Due to their low glass transition temperature and strong bonds, silicones play a prominent role in the construction industry.[68-70] As a structural sealant, silicones have proven to be incredibly durable under the conditions that are ordinarily experienced due to weathering.[71, 72] One part curing RTVs provide a simple method of application, while the low surface tension of silicones ensures that they permeate and completely wet the surface they are applied to, regardless of pores and cracks in the surface. Such sealants have found prominent use in ship construction as marine anti-fouling coatings.[73, 74]

1.5.2 Silicones in Household Products and Personal Care Applications

Household items and personal care products that prominently feature silicones as a constituent are shown in **Figure 1.18**. In paints, silicones are added in small quantities as performance-enhancers that promote the even wetting and adhesion of paints to substrate.[75] They can also be the major component of other paints in the form of resins, where long-term water repellency and wear resistance is a concern.[76] In fabrics, silicones can give anti-static properties[77] due to the fact that they are electrical insulators. Since it cures in air, is water-repellent and also discourages the growth of bacteria, silicone caulking is a very popular choice for preventing leaks in the bathroom, especially near the bathtub or sink.[78]

Figure 1.18 Silicones prominently featured in products such as spatulas, sealants, children's toys, paint, cosmetics and personal care products. All images are public domain.

Silicones were likely first introduced to the average customer when they were used in a skin application in the 1950s, but it was not until their use in deodorants in 1970s that the market began to rapidly expand.[79] The cyclosiloxane oils, shown in **Figure 1.19** are some of the most important compounds in beauty care, cosmetics, and personal care products.

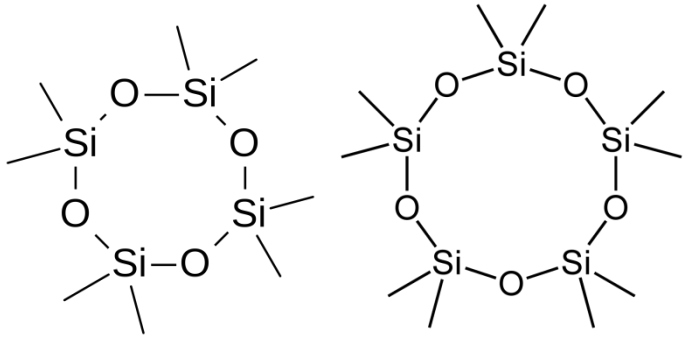

Figure 1.19 Octamethylcyclotetrasiloxane (left) and Decamethylcyclopentasiloxane. Two commonly used silicone oils in the cosmetics industry.

These compounds are notable because of the feel that they provide to things like creams, moisturizers and shampoos.[80] They often provide the smoothness and even spreading that is necessary when applied to skin.[81] For instance UV-protective lotions are only effective when all of the skin is coated and covered by it.[82, 83] Additionally, these products need to be resistant to sweat and contact with water so they work for extended periods of time; silicones complete this task by affording a degree of hydrophobicity. When in shampoo formulations, silicones leave a glossy, silky feel that is desired by customers, and it gives hair a certain sheen and brightness.

1.5.3 Medical Applications of Silicones

Silicones are used in medical devices in all of their forms, be it as oils, gels, elastomers, etc.[1, 84-86] The reason they excel in these roles is due to their biocompatibility. Biocompatibility is

defined as “the ability of a material to perform with an appropriate host response in a specific situation.”[87] This section will briefly cover both the most common applications of silicones in medical technology.

The first use of an organosiloxane in the medical field can be traced to 1946, when methylchlorosilane-treatment of glassware was shown to prevent blood clotting.[88] Surface silanol groups on the glass can condense with chlorosilane, leading to the formation of silicone oil that is bonded to the glass. A possible explanation for the anti-clotting property is that the low surface energy of PDMS stabilizes platelets and inhibits aggregation (a necessary step for clotting to occur). Shortly after this report, biliary surgery was performed using silicone tubing for the repair of damaged gastrointestinal ducts.[89] Ever since, silicones have played a prominent role in the medical field.

Figure 1.20 Silicones in some common medical devices such as catheters, drains, tubes and cannulae.[3]

Shown in **Figure 1.20-21** are examples of silicone based medical implants that are currently in use. **Figure 1.20** shows a variety of silicone-based short-term medical implants and devices such as a thoracic drain, cannula and a catheter. Silicone coatings on catheters reduce encrustation from bodily mineral salts due to the non-wettability of the surface.[3] **Figure 1.21** shows a hydrocephalic shunt for long-term implantation. Hydrocephalus is a condition where fluid buildup in the brain causes swelling and compression of the brain stem.[90]

Figure 1.21 The Sphera Duo hydrocephalus shunt system, made from transparent medical grade silicone. Permission obtained from Spiegelberg.

As pharmaceutical ingredients, silicones play both a passive and active role. In topical ointments and creams, 'cyclomethicone' (i.e., the volatile cyclosiloxanes) is commonly used as skin protectant and aids in preventing dryness and moisture loss. PDMS fluids are listed as 'dimethicone' are found as an active pharmaceutical ingredient (API) in formulations as diverse as diaper rash cream[91] (in conjunction with zinc oxide) and anti-flatulents (in conjunction with finely divided silica).[92] In the form of an elastomer, silicones can be used as pressure-sensitive adhesives in transdermally delivered drugs.[93] This allows for the slow and steady delivery of compounds such as fentanyl.[94, 95] Silicones are ideal for this process since they are permeable to small hydrophobic molecules, which encompass a large number of pharmaceutical compounds.

1.5.4 Functionalized Silicone Materials

It is no surprise that several research groups around the world have dedicated research to developing silicone materials. This section will briefly cover some of the more promising literature reports of potential applications of silicone composites. Since this thesis is particularly focused on silicone composites with respect to biomedical applications and low surface energy materials, the examples provided will highlight ongoing research into these two areas.

1.5.4.1 Biomedical Research

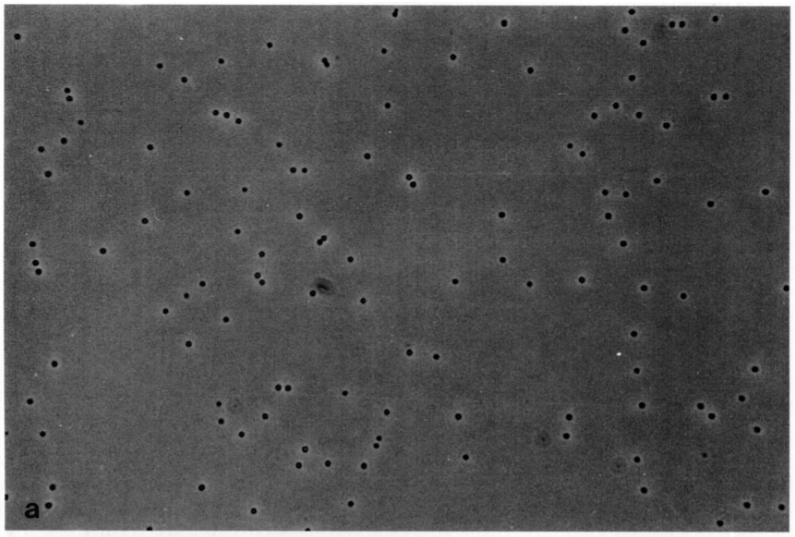

Figure 1.22 Silicone microdroplets shown above (black dots). Average size is 1.5 μm.[96]

Silicone's ability to uptake pharmaceutical agents is of interest in the biomedical field.[97] Thus, research has been invested in developing micro-materials that could enter the human body. Silicone-derived microcapsules, for instance, traditionally begin with the polymerization of alkoxy-monomers of PDMS via condensation. The monomers used are methyltriethoxysilane (MTES) and dimethyldiethoxysilane (DMDES). By adding these monomers to a basic or acidic aqueous solution, Obey, et. al obtained well-formed PDMS droplets, shown on the previous page (**Figure 1.22**).[96]

Obey reported that the viscoelastic properties of the obtained PDMS droplets could be varied by changing the concentration of the two monomers. As noted earlier in the chapter, using type D and T monomers will generally result in cyclics and viscoelastic PDMS, as opposed to the fully cross-linked solid. Indeed, Obey noted that the product obtained is a "silicone oil microgel". PDMS obtained from this Stober-like process is a stable emulsion in water, but destabilizes when an alcohol such as ethanol is added.

Oil-core microcapsules have long been in use in the food/beverage industry and the cosmetics industry.[98] Thus, the next advance in functionalized PDMS droplets came when it was noted that PDMS droplets could serve as the oil core and the shell could be made by bonding tetraethylorthosilicate (TEOS, Q-type monomer) to the surface. This is made possible by surface silanol groups, which remain unbonded.[99] TEOS reacts and cross-links around the oil core to form a silica shell**. Figure 1.23** shows an SEM of the product obtained, which contains broken shells as well as unbroken shells. The liquid interior has evaporated and additionally, it appears that agglomeration has occurred, either during synthesis or upon drying.

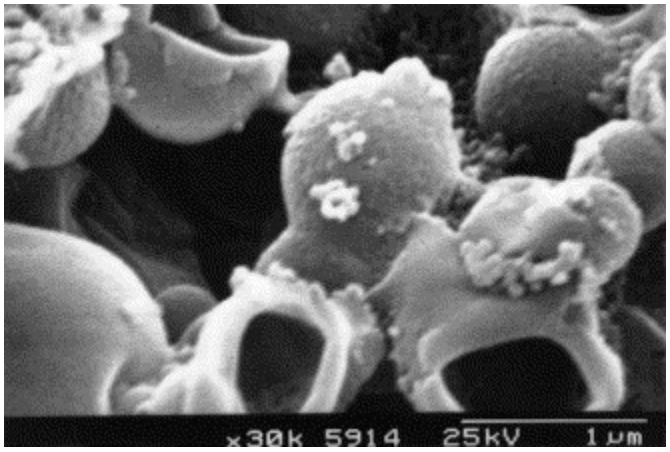

Figure 1.23 Scanning electron micrograph of broken and unbroken shells of PDMS-silica core-shell microparticles, synthesized by Goller.[99]

Years later, the Imhof group discovered a process to make well-formed monodisperse silica-shell PDMS microspheres (**Figure 1.24**) by adding a polyvinylpyrrolidone surfactant.[100] These core-shell particles can be size-tuned, and it was found that the core could be exchanged with surrounding media. Thus, it is possible that the PDMS core of these particles could be loaded with a drug.

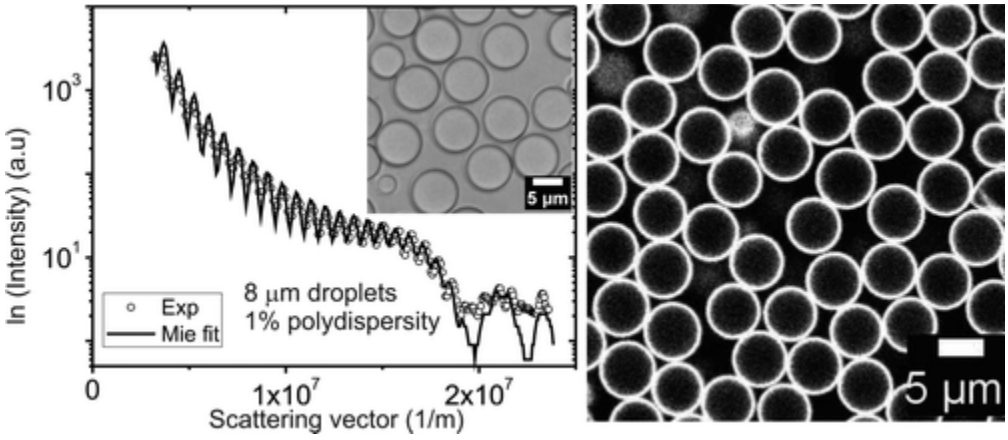

Figure 1.24 Light scattering fit of PDMS droplets (left) and silica-shell PDMS microspheres (right).[100]

1.5.4.2 Low Surface Energy Materials

PDMS is the ideal polymer for producing low surface energy materials: it adheres well to a variety of substrates, it is easy to functionalize, and it coats almost all surfaces evenly and with ease. Thus, much research has been dedicated to producing low-surface energy materials using PDMS. For instance, by using lithography, any type of repeating pattern can be etched onto a PDMS surface. As will be discussed in the next chapter, patterned surfaces prevent the wetting of liquids by introducing air pockets that are hard to displace. Three examples are shown below in **Figure 1.25**. The Senez group utilized a mushroom type geometry (**Figure 1.25a**) to obtain flexible liquid-repellent surfaces,[101] while Tuteja used a pillar morphology in conjunction with a

fluorosilicone **(Figure 1.25b**).[102] The latter surface has the advantage of being transparent, which could enable use in windshields, touchscreens, etc. However, obvious drawbacks to using lithography are its cost-ineffectiveness and multistep procedures required to fabricate complex architectures.

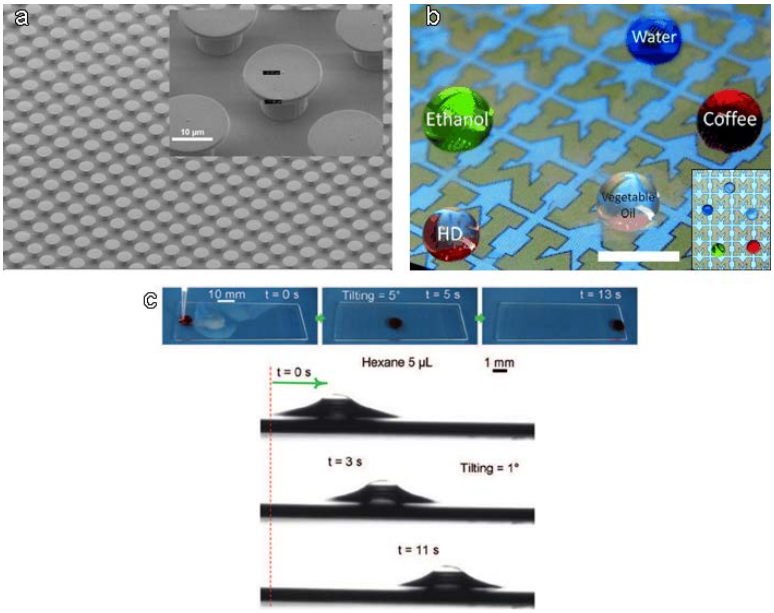

Figure 1.25 a) Micro-mushroom PDMS surface made using lithography and functionalized with a fluorosilane. b) Transparent pillar surface coated with fluorinated silicone on a touchscreen display, repelling ethanol water, coffee, vegetable oil and hexadecane. Scale bar is 500 µm. c) Glass slide coated with linear PDMS. The toluene droplet (red) slides across with no streaking. A hexane droplet slides across the same surface even at a tilt of 1°.[101-103]

Another rapidly emerging technology for liquid-repellency is the lubricant-infused surface. Instead of a solid coating, a liquid coating is applied to a surface, providing a low-friction interface that is impermeable to a contaminating liquid. The contaminating liquid droplet slides off easily keeping the surface clean. Recently, McCarthy has developed a simple condensation route to bonding silicone oil to glass[103] (**Figure 1.25c**). This surface was found to repel water as well as several oils. Since the glass and silicone are bonded via the strong Si-O

bond, there is little possibility for physical removal of the oil, though chemical degradation via hydrolysis is possible. One drawback is that this technique is limited to substrates which have a sufficiently high affinity for forming siloxane bonds as well as a high enough surface hydroxyl ratio for forming those bonds.

1.6 Summary

Silicones are an important polymer in a variety of applications, ranging from manufacturing, food processing, pharmaceuticals, healthcare, cosmetics, biomedical implants, microfluidics and coatings. Biocompatibility, inertness, chemical resistance and flexibility are among the key properties that enable their use in such diverse technologies. Due to the numerous types of silicones available, the ease of chemically functionalizing them and the control over their final composition, any number of silicone-based materials can be pursued. As will be seen in this thesis, radically different functionalized composites can be produced, each with PDMS as a part of their formulation.

1.7 References

1) S. Braley. The chemistry and properties of the medical-grade silicones. *Journal of Macromolecular Science—Chemistry*, 1970, **4**, 529-544.

2) A. Colas. Silicones: Preparation, properties and performance. *Dow Corning, Life Sciences*, 2005.

3) A. Colas and J. Curtis. Silicone biomaterials: history and chemistry. *Biomaterials science: An introduction to materials in medicine*, 2004, **2**, 80-85.

4) W. Noll. *Chemistry and technology of silicones*, Elsevier, 2012.

5) A. O'Lenick. Basic silicone chemistry–a review. *Silicone Spectator*, 2009, 1-23.

6) L. Sommer. An introduction to the chemistry of silicones. *J. Chem. Educ*, 1952, **29**, 588.

7) H. H. Moretto, M. Schulze and G. Wagner. Silicones. *Ullmann's Encyclopedia of Industrial Chemistry*, 1993.

8) C. Burger and F.-H. Kreuzer, in *Silicon in Polymer Synthesis*, Springer, 1996, pp. 113-222.

9) J. Wu, Z. L. Wu, H. Yang and Q. Zheng. Crosslinking of low density polyethylene with octavinyl polyhedral oligomeric silsesquioxane as the crosslinker. *RSC Advances*, 2014, **4**, 44030-44038.

10) J. Berzelius. Zersetzung der ussspatsauren Kieselerde durch Kalium. *Ann. Phys. Chem*, 1824, **1**, 169-208.

11) C. Friedel and J. Crafts. Ueber einige neue organische Verbindungen des Siliciums und das Atomgewicht dieses Elementes. *Justus Liebigs Annalen der Chemie*, 1863, **127**, 28-32.

12) F. S. Kipping and L. L. Lloyd. XLVII.—Organic derivatives of silicon. Triphenylsilicol and alkyloxysilicon chlorides. *Journal of the Chemical Society, Transactions*, 1901, **79**, 449-459.

13) E. G. Rochow. The direct synthesis of organosilicon compounds. *Journal of the American Chemical Society*, 1945, **67**, 963-965.

14) B. Hardman and A. Torkelson. Silicones. *Encyclopedia of polymer science and engineering*, 1989, **15**, 243.

15) W. Patnode and D. F. Wilcock. Methylpolysiloxanes. *Journal of the American Chemical Society*, 1946, **68**, 358-363.

16) R. O. Sauer. Derivatives of the methylchlorosilanes. I. Trimethylsilanol and its simple ethers. *Journal of the American Chemical Society*, 1944, **66**, 1707-1710.

17) S. W. Kantor. The hydrolysis of methoxysilanes. Dimethylsilanediol. *Journal of the American Chemical Society*, 1953, **75**, 2712-2714.

18) F. Stark, J. Falender and A. Wright. Silicones. *Comprehensive organometallic chemistry*, 1982, **2**, 305.

19) Karstedt, B. Platinum complexes of unsaturated siloxanes and platinum containing organopolysiloxanes. US Patent 3,775,452; 1973.

20) S. J. Clarson and J. A. Semlyen. *Siloxane polymers*, Prentice Hall, 1993.

21) Y. Xia and G. M. Whitesides. Soft lithography. *Annual review of materials science*, 1998, **28**, 153-184.

22) B. Marciniec. *Hydrosilylation: a comprehensive review on recent advances*, Springer Science & Business Media, 2008.

23) A. J. Chalk and J. Harrod. Homogeneous Catalysis. II. The Mechanism of the Hydrosilation of Olefins Catalyzed by Group VIII Metal Complexes. *Journal of the American Chemical Society*, 1965, **87**, 16-21.

24) G. C. Lisensky, D. J. Campbell, K. J. Beckman, C. E. Calderon, P. W. Doolan, R. M. Ottosen and A. B. Ellis. Replication and compression of surface structures with polydimethylsiloxane elastomer. *J. Chem. Educ*, 1999, **76**, 537.

25) B. Arkles. Silicon Compounds, Silanes. *Kirk-Othmer Encyclopedia of Chemical Technology*, 1980.

26) C. Lee, R. Niemi and K. Kelly. New Silicone RTV Foam. *Journal of Cellular Plastics*, 1977, **13**, 62-67.

27) J. Cervantes, R. Zárraga and C. Salazar-Hernández. Organotin catalysts in organosilicon chemistry. *Applied Organometallic Chemistry*, 2012, **26**, 157.

28) V. Severnyi, R. Minasyan, I. Makarenko and N. Bizyukova. Mechanism of Cold Vulcanization of Low-Molecular Polyorganosiloxane Rubbers. *Vysokomolekularanye Soedineniya Seriya A*, 1976, **18**, 1276-1281.

29) F. W. van Der Weij. The action of tin compounds in condensation-type RTV silicone rubbers. *Die Makromolekulare Chemie,* 1980, **181**, 2541-2548.

30) W. Lynch. *Handbook of silicone rubber fabrication,* Van Nostrand Reinhold Company, 1978.

31) D. Brassard. *The Silicone Elastomer Handbook,* Silicone Solutions, 2010.

32) C. Gelsest. Reactive silicones: forging new polymer links. *Gelest Inc, Morrisville, Pennsylvania, Available at: www.gelest.com/company/ pdfs/reactivesilicones.pdf,* 1967.

33) http://www.dowcorning.com/DataFiles/090276fe80190b08.pdf.

34) M. Owen. Why silicones behave funny. *Chemtech*, 1981, **11**, 288-292.

35) W. Robb. Thin Silicone Membranes-Their Permeation Properties and Some Applications. *Annals of the New York Academy of Sciences*, 1968, **146**, 119-137.

36) E. Yilgör and I. Yilgör. Silicone containing copolymers: synthesis, properties and applications. *Progress in Polymer Science,* 2014, **39**, 1165-1195.

37) J. Brandrup, E. H. Immergut, E. A. Grulke, A. Abe and D. R. Bloch. *Polymer handbook*, Wiley New York etc, 1989.

38) R. N. Shimizu and N. R. Demarquette. Evaluation of surface energy of solid polymers using different models. *Journal of Applied Polymer Science*, 2000, **76**, 1831-1845.

39) F. Rodriguez, C. Cohen, C. K. Ober and L. Archer. *Principles of polymer systems*, CRC Press, 2014.

40) R. Sanderson. *Chemical Bonds and Bonds Energy,* Elsevier, 2012.

41) S. Bhattacharya, A. Datta, J. M. Berg and S. Gangopadhyay. Studies on surface wettability of poly (dimethyl) siloxane (PDMS) and glass under oxygen-plasma treatment and correlation with bond strength. *Journal of microelectromechanical systems*, 2005, **14**, 590-597.

42) J. Garra, T. Long, J. Currie, T. Schneider, R. White and M. Paranjape. Dry etching of polydimethylsiloxane for microfluidic systems. *Journal of Vacuum Science & Technology A*, 2002, **20**, 975-982.

43) S. J. Hwang, D. J. Oh, P. G. Jung, S. M. Lee, J. S. Go, J.-H. Kim, K.-Y. Hwang and J. S. Ko. Dry etching of polydimethylsiloxane using microwave plasma. *Journal of Micromechanics and Microengineering*, 2009, **19**, 095010.

44) D. Bodas and C. Khan-Malek. Formation of more stable hydrophilic surfaces of PDMS by plasma and chemical treatments. *Microelectronic engineering*, 2006, **83**, 1277-1279.

45) D. Bodas and C. Khan-Malek. Hydrophilization and hydrophobic recovery of PDMS by oxygen plasma and chemical treatment—An SEM investigation. *Sensors and Actuators B: Chemical*, 2007, **123**, 368-373.

46) Q. He, Z. Liu, P. Xiao, R. Liang, N. He and Z. Lu. Preparation of hydrophilic poly (dimethylsiloxane) stamps by plasma-induced grafting. *Langmuir*, 2003, **19**, 6982-6986.

47) J. Hildebrand and R. Scott. Solubility of Nonelectrolytes Reinhold Pub. *Co., New York*, 1950, **3**.

48) J. H. Hildebrand and R. L. Scott. *Regular solutions*, Prentice-Hall, 1962.

49) J. E. Mark. *Physical properties of polymers handbook*, Springer, 2007.

50) A. F. Barton. *Handbook of polymer-liquid interaction parameters and solubility parameters*, CRC press, 1990.

51) J. N. Lee, C. Park and G. M. Whitesides. Solvent compatibility of poly (dimethylsiloxane)-based microfluidic devices. *Analytical chemistry*, 2003, **75**, 6544-6554.

52) P. J. Flory and J. Rehner Jr. Statistical Mechanics of Cross-Linked Polymer Networks I. Rubberlike Elasticity. *The Journal of Chemical Physics*, 1943, **11**, 512-520.

53) M. Hunter, J. Hyde, E. Warrick and H. Fletcher. Organo-Silicon Polymers. The Cyclic Dimethyl Siloxanes*. *Journal of the American Chemical Society*, 1946, **68**, 667-672.

54) J. F. Hyde, Method of rendering glass. US Patent 2,439,689; 1948.

55) M. Andriot, S. Chao, A. Colas, S. Cray, F. deBuyl, J. DeGroot, A. Dupont, T. Easton, J. Garaud, E. Gerlach, F. Gubbels, M. Jungk, S. Leadley, J. Lecomte, B. Lenoble, R. Meeks, A. Mountney, G. Shearer, S. Stassen, C. Stevens, X. Thomas and A. Wolf. *Silicones in industrial applications*, Gleria, R. D. J. M., Nova Science Publishers, New York, 2009.

56) F. Stefanoiu. Synthèse et caractérisation d'ASAs (Anhydrides Alkényles Succiniques) et de dérivés d'ASAs–Application à l'industrie des lubrifiants. 2007.

57) M. L. Joseph, P. B. Hudson, A. C. Clapp and D. Kness. *Joseph's introductory textile science*, Harcourt Brace Javanovich College Publishers, 1993.

58) H. L. Needles. *Textile fibers, dyes, finishes, and processes*, Standard Publishers Distributors, 2001.

59) Wright, J. H. Grease-like silicone compound. US Patent 3,453,210: 1969.

60) R. Zechel, P. Lonsky and H. Trautmann. Molykote. 1991.

61) G. A. Smook. *Handbook for pulp & paper technologists*, Tappi, 1992.

62) B. Junker. Foam and its mitigation in fermentation systems. *Biotechnology progress*, 2007, **23**, 767-784.

63) D. T. Wasan and S. P. Christiano. Foams and antifoams: a thin film approach. *Handbook of Surface and Colloid Chemistry*, 1997, 179-215.

64) P. Garrett. The mode of action of antifoams. *Surfactant Science Series*, 1993, 1-1.

65) R. Kulkarni, E. Goddard and P. Chandar. Science and technology of silicone antifoams. *SURFACTANT SCIENCE SERIES*, 1996, 555-585.

66) N. D. Denkov. Mechanisms of foam destruction by oil-based antifoams. *Langmuir*, 2004, **20**, 9463-9505.

67) N. D. Denkov, S. Tcholakova, K. G. Marinova and A. Hadjiiski. Role of oil spreading for the efficiency of mixed oil-solid antifoams. *Langmuir*, 2002, **18**, 5810-5817.

68) F. De Buyl. Silicone sealants and structural adhesives. *International Journal of Adhesion and Adhesives*, 2001, **21**, 411-422.

69) B. Parbhoo; L. O'Hare and S. Leadley, Fundamental aspects of adhesion technology in silicones (Chapter 14). Elsevier: Amsterdam: 2002; pp 677-711.

70) A. Wolf. Durability of silicone sealants. *RILEM report*, 1999, 253-274.

71) D. Oldfield and T. Symes. Long term natural ageing of silicone elastomers. *Polymer Testing*, 1996, **15**, 115-128.

72) L. B. Sandberg. Comparisons of silicone and urethane sealant durabilities. *Journal of materials in civil engineering*, 1991, **3**, 278-291.

73) M. E. Callow and J. A. Callow. Marine biofouling: a sticky problem. *Biologist*, 2002, **49**, 1-5.

74) A. A. Finnie and D. N. Williams. Paint and coatings technology for the control of marine fouling. *Biofouling*, 2010, **18**.

75) M. Glaser. Silicone in protective coatings. *Industrial & Engineering Chemistry*, 1954, **46**, 2334-2342.

76) H. Mayer. Masonry protection with silanes, siloxanes and silicone resins. *Surface Coatings International Part B: Coatings Transactions*, 1998, **81**, 89-93.

77) Zenon, H. J. Liquid composition for fabric treatment. US Patent 3,992,332: 1976.

78) M. R. Nejadnik, H. C. van der Mei, W. Norde and H. J. Busscher. Bacterial adhesion and growth on a polymer brush-coating. *Biomaterials*, 2008, **29**, 4117-4121.

79) A. DiSapio and P. Fridd. Silicones: use of substantive properties on skin and hair. *International journal of cosmetic science*, 1988, **10**, 75-89.

80) E. Abrutyn and B. Bahr. Formulating enhancements for underarm applications. *Cosmetics and Toiletries*, 1993, **108**, 51-51.

81) G. De Backer and D. Ghirardi. Goodbye to grease. *Soap Perfumery and Cosmetics*, 1993, **66**, 37-38.

82) A. J. DiSapio. Silicones as adjuvants in sun products. *Cosmetics and toiletries*, 1987, **102**, 102-106.

83) M. Lanzet. Comedogenic effects of cosmetic raw materials. *Cosmetics and toiletries*, 1986, **101**, 63-72.

84) B. Arkles and P. Redinger. Silicones in biomedical applications. *Biocompatible polymers, metals, and composites. Lancaster, PA: Technomic*, 1983, 749-768.

85) R. Blocksma and S. Braley. THE SILICONES IN PLASTIC SURGERY. *Plastic and reconstructive surgery*, 1965, **35**, 366-370.

86) J. Curtis and A. Colas. Medical applications of silicones. *Biomaterials science: An introduction to materials in medicine*, 2004, 697-707.

87) J. Black. *Biological performance of materials: fundamentals of biocompatibility*, CRC Press, 2005.

88) L. Jaques, E. Fidlar, E. Feldsted and A. MacDonald. Silicones and blood coagulation. *Canadian Medical Association Journal*, 1946, **55**, 26.

89) F. Lahey. Comments made following the speech "Results from using Vitallium tubes in biliary surgery," read by Pearse, HE before the American Surgical Association, Hot Springs, VA. *Ann. Surg*, 1946, **124**, 1027.

90) K. T. Kahle, A. V. Kulkarni, D. D. Limbrick and B. C. Warf. Hydrocephalus in children. *The Lancet*, 2016, **387**, 788-799.

91) M. J. Sibley; D. E. Hartung and R. Ruland, Buffered diaper rash cream. Google Patents: 1994.

92) J. A. Rider and H. C. Moeller. Use of silicone in the treatment of intestinal gas and bloating. *JAMA*, 1960, **174**, 2052-2054.

93) H. M. Leeper and R. M. Wright. Elastomers in medicine. *Rubber Chem. Technol.*, 1983, **56**, 523-556.

94) H. Aliyar and G. Schalau. Recent developments in silicones for topical and transdermal drug delivery. *Therapeutic delivery*, 2015, **6**, 827-839.

95) K. Ulman and X. Thomas. Silicone pressure sensitive adhesives for healthcare applications. *Handbook of Pressure Sensitive Adhesive Technology. 3rd ed. Rhode Island: Satas & Associates*, 1999, 724-747.

96) T. M. Obey and B. Vincent. Novel Monodisperse" Silicone Oil"/Water Emulsions. *Journal of colloid and interface science*, 1994, **163**, 454-463.

97) R. K. Malcolm, S. McCullagh, A. D. Woolfson, M. Catney and P. Tallon. A dynamic mechanical method for determining the silicone elastomer solubility of drugs and pharmaceutical excipients in silicone intravaginal drug delivery rings. *Biomaterials*, 2002, **23**, 3589-3594.

98) H. N. Yow and A. F. Routh. Formation of liquid core–polymer shell microcapsules. *Soft Matter*, 2006, **2**, 940-949.

99) M. Goller and B. Vincent. Silica encapsulation of liquid PDMS droplets. *Colloids and Surfaces A: Physicochemical and Engineering Aspects*, 1998, **142**, 281-285.

100) N. A. Elbers, J. Jose, A. Imhof and A. van Blaaderen. Bulk Scale Synthesis of Monodisperse PDMS Droplets above 3 μm and Their Encapsulation by Elastic Shells. *Chemistry of Materials*, 2015, **27**, 1709-1719.

101) R. Dufour, M. Harnois, Y. Coffinier, V. Thomy, R. Boukherroub and V. Senez. Engineering sticky superomniphobic surfaces on transparent and flexible PDMS substrate. *Langmuir*, 2010, **26**, 17242-17247.

102) K. Golovin, D. H. Lee, J. M. Mabry and A. Tuteja. Transparent, Flexible, Superomniphobic Surfaces with Ultra-Low Contact Angle Hysteresis. *Angewandte Chemie International Edition*, 2013, **52**, 13007-13011.

103) L. Wang and T. J. McCarthy. Covalently Attached Liquids: Instant Omniphobic Surfaces with Unprecedented Repellency. *Angewandte Chemie*, 2016, **128**, 252-256.

CHAPTER 2: SPRAYABLE OMNIPHOBIC COATINGS

2.1 Introduction

This chapter is taken in large part from the following reference:

Neelakantan, N. K.; Weisensee, P. B.; Overcash, J.W.; Torrealba E.J.; Suslick, K. S.; King, W. P. Spray-On Omniphobic ZnO coatings. *RSC Advances* **2015**, *5*, 29643-29650.

The water-shedding property of the Lotus plant (i.e. the "Lotus effect") is the most well-known example of liquid repellency.[1-3] The underpinnings behind this phenomenon require an understanding of the physical forces that govern interfacial interactions between liquids, surfaces and air. Young originally described the contact angle[4] of a liquid droplet for an ideal flat surface using the following equation:

$$\gamma_{sl} + \gamma_{lg} \cos\theta = \gamma_{sg}$$

Where θ is the contact angle (also called the Young contact angle), and: γ_{sl}, γ_{lg}, γ_{sg} are the solid/liquid, liquid/gas and solid/gas interfacial energies respectively. **Figure 2.1** illustrates the force balance of the tensions and the standard protocol for measuring contact angles.

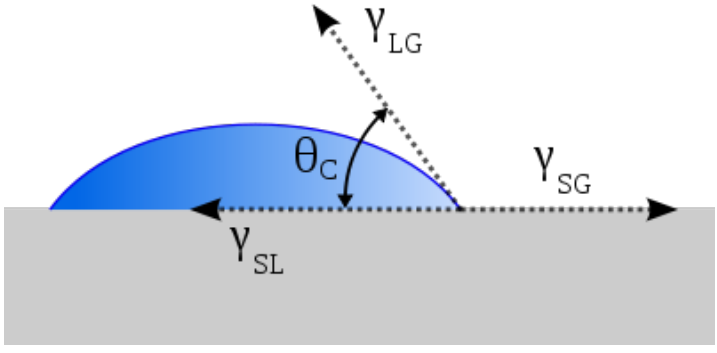

Figure 2.1 Force balance showing Young contact angle of a droplet on an ideal, flat surface.

Thus, surfaces can be described as hydrophilic (θ <90) or hydrophobic (θ >90) for a water droplet. For even the lowest energy smooth surfaces, the largest water contact angles 120°. However, water droplets form a nearly 150° contact angle with the lotus plant. Furthermore, these droplets slide off the lotus leaf with ease. It is, in fact, the micro-roughness of the lotus leaf[5] that sustains these unusually high contact angles (**Figure 2.2**). Air pockets occupy the voids where a liquid droplet cannot penetrate, as the energetic cost is too high to do so, enhancing the contact angle of the liquid.

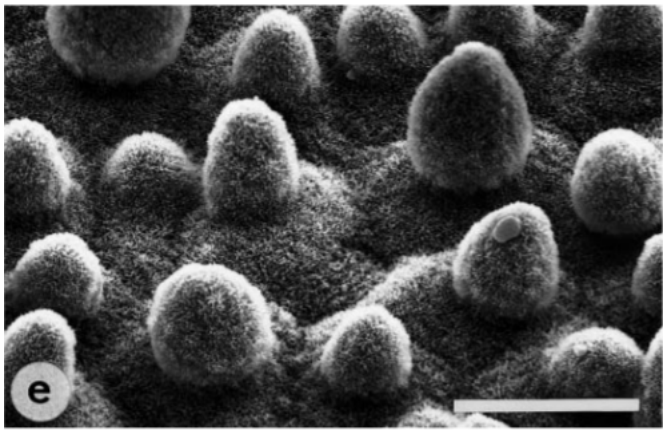

Figure 2.2 Scanning electron micrograph of a lotus leaf surface showing roughened papules. Scale bar is 20 μm.[5]

Wenzel[6] first described contact angles of droplets on rough surfaces using the following equation:

$$\cos\theta_W = r\cos\theta$$

Where θ_W is the Young contact angle and r is the roughness of the surface, that is, the projected surface area divided by the nominal surface area. This equation applies to droplets in which the liquid penetrates the voids, meaning that roughness increases the contact angle of water if the

surface is hydrophobic, but decreases it if it is hydrophilic. Cassie and Baxter[7] then developed the following equation:

$$\cos\theta_{CB} = r_f f \cos\theta + f - 1$$

where θ_{CB} is the apparent contact angle in the Cassie-Baxter state, r_f is the roughness of the wetted surface, and f is the fraction of the solid in contact with the liquid. The preceding equations presented describe droplets (**Figure 2.3**) in the following states: the Wenzel state, in which rough cavities are penetrated by the liquid, and the Cassie-Baxter state, in which voids are filled with air that are not penetrated by liquid. The Cassie-Baxter equation and droplet state accurately describe a water droplet on a lotus leaf, (droplets in the Wenzel state tend to pin to the surface).

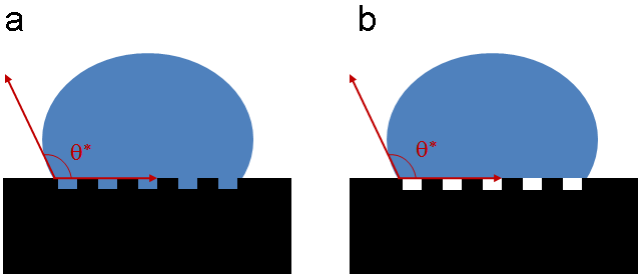

Figure 2.3 (a) Wenzel droplet (blue) with apparent contact angle θ^*. The droplet is penetrating a textured surface (black). (b) Cassie-baxter droplet (blue) with apparent contact angle θ^*. The droplet cannot displace air voids and as a result, the textured surface (black) is unwet.

2.1.1 Omniphobic Surfaces

Synthetic surfaces that mimic the lotus leaf[8-10] rely on hierarchical roughness to prevent wetting by water. Due to their low surface tension, most oils cannot form contact angles greater than 90° on flat surfaces or those with nano- and microstructures with positive or vertical slopes.

Re-entrant structures with overhanging slopes are necessary to repel these kinds of liquids.[11-13] So-called 'superomniphobic' surfaces[14, 15] repel both water and a variety of oils and other low surface- tension liquids and are characterized by high droplet mobility. Superomniphobic surfaces have been prepared by a number of methods: e.g., lithographically patterned roughness, low surface energy coatings, metal oxide nanoparticle coatings, electrodeposition, and electrospun textured polymers.[16-24]

A key challenge for omniphobic surfaces remains: facile and scalable fabrication. Many of the methods used to fabricate omniphobic surfaces are tedious, multi-step procedures requiring specialty equipment and chemicals, and in many cases are simply too expensive to implement at large scale. In the same vein, silicon wafers are commonly used as the substrate,[13, 15, 18] but these are not often relevant to industrial or real-world applications. There is a need for methods that are compatible with a wide variety of substrate materials, including glass, metals and polymers. Of the many ways for making omniphobic surfaces, spray-coating[25-28] has significant advantages: an aerosol from a precursor solution containing the necessary chemical components can coat a surface evenly regardless of its dimensions, geometry, or substrate material. Spray-coating is also inexpensive and easily scaled-up. Nanoparticle zinc oxide (ZnO) is a suitable precursor, as it is non-toxic, commercially available, and controllaly textured.

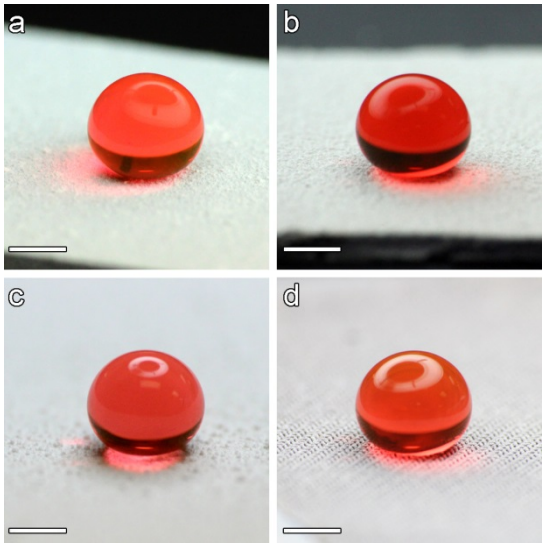

Figure 2.4 Photographs of a water droplet (containing red dye) on spray coated surfaces of (a) aluminium, (b) silicon wafer, (c) cellulose filter paper and (d) copper mesh. All surfaces were spray-coated with a 2:1 solution of ZnO:PDMS. Scale bars represent 1 mm.

Using a polydimethylsiloxane (PDMS) binder, we report a simple method of fabricating a hierarchically roughened surface with intrinsic re-entrant microstructures that can be easily modified with a low surface-energy overcoating (**Figure 2.4**). Qualitative relationships between the surface chemistry, surface roughness, and wettability for various ZnO:PDMS mass ratios and surface coatings are presented. Given the interest in making superomniphobic surfaces that favor drop-wise condensation over film-wise condensation and thus improve the efficiency of condensers, we have examined quantitatively the wetting behavior of these surfaces with both water and a common refrigeration lubricant (RL). To that end, we have characterized the performance of these surfaces by measuring the static contact angles (SCA) and sliding angles (α) of water (surface tension = 72.6 mN/m) and RL-68H (from Emkarate Corp., surface tension = 27.7 mN/m).[29] RLs are generally polyol esters miscible with hydrofluorocarbon (HFC) refrigerants that cycle through a refrigerator and keep all moving parts properly lubricated. The goal of the present work is to prevent film formation of RL on refrigeration piping and condenser

surfaces as a first step towards designing coatings that could improve the performance of heat transfer equipment.

2.2 Experimental

2.2.1 Materials

Four materials were tested as substrates for the omniphobic coatings. Silicon wafers (150 mm diameter, 675 µm thick, type P, <100>) were purchased from Ted Pella, Inc. and cut into 8x10 mm pieces. Other substrate examined include stock aluminium sheet (alloy 6061, .063", McMaster-Carr, 12x25 mm), copper wire mesh (wire diameter 50 µm, mesh opening 75 µm, TWP Inc., 8x10 mm) and cellulose filter paper (qualitative grade, Whatman #1001, 70 mm diameter). Zinc oxide powder (NanoGard), particle diameter 40-100 nm, was used as received from Alfa Aesar. Sylgard 182 (Dow Corning), perfluorodecyltrichlorosilane (Gelest), and hexanes (Fisher Scientific) were used as received. RL-68H (Emkarate), Teflon AF 1600 (DuPont) and Fluorinert FC-770 (3M) were used as received.

2.2.2 Solution Preparation

First, a stock solution of 0.25 g Sylgard 182 (PDMS) /mL hexanes was prepared. In a scintillation vial, 0.5 g ZnO was added; this was the standard amount used in fabricating all samples. The stock PDMS solution was added to the ZnO at mass ratios of 1:2, 1:1 and 2:1 ZnO:PDMS, i.e., 4 mL, 2 mL and 1 mL respectively. Hexane was added to these solutions until the final volumes were ~20 mL. Then, the solutions were manually agitated to disperse the ZnO and PDMS evenly. This process was expedited by the use of an ultrasonication bath when

necessary. Higher ratios of ZnO:PDMS (i.e., 3:1, 4:1) resulted in dispersions that were insufficiently stable to permit spray deposition.

2.2.3 Spray Procedure

For spraying procedure, aerosols were produced using a Badger 250 airbrush attached to a compressed air tank. Substrates were placed on a hot plate set to the lowest heat setting to facilitate solvent evaporation during spraying. The airbrush outlet is roughly 0.5 mm in diameter, and the air pressure used for spraying was 20 psi, corresponding to a flow rate of ~10 mL/min. The airbrush was held 15-20 cm from the substrate to ensure complete coverage and avoid any pooling of liquid on the surface. Coated samples were then cured in a Lindberg/Blue M programmable oven at 70 °C for 24 hours.

2.2.4 Teflon Coating

After samples were removed from oven and cooled, a 5:1 v/v solution of Fluorinert FC-770 to Teflon AF was prepared. The amount necessary per sample is 100 μL FC-770 to 20 μL Teflon AF. Samples were dipped in a petri dish of the Teflon solution for 10-20 seconds so that the entire surface was coated. They were then placed in an oven and cured according to the manufacturer's instructions: 105°C for 5 min, ramped over 5 min to 160°C and held for 5 min, ramped over 5 min to 330°C and held for 15 min.

2.2.5 Fluorosilane Deposition

Alternatively, a liquid-phase deposition method similar to one previously reported in the literature was used to functionalize uncoated ZnO:PDMS surfaces with a commercial fluorosilane. Samples were placed in a vial with 20 mL of hexanes, and then cooled to -10 °C. 50 μL of perfluorodecyltrichlorosilane (FDTS) were then added, and the reaction proceeded for 24

hours at -10°C. The samples were then dried and rinsed with ethanol to remove any unwanted byproducts.

Plasma-etchng: Some samples were also pre-treated with oxygen plasma for 1 min at 70 W and immediately submerged in 10 mL of toluene in a scintillation vial; 50 μL of FDTS were then added and allowed to react for 1 hour at room temperature.

2.2.6 Characterization

Electron microscope images of Teflon-coated samples were taken using a JEOL 7000F and a Philips XL30 ESEM-FEG scanning electron microscope. Samples were sputter-coated with Au/Pt for 25 sec (a thickness of 7-8 nm) prior to image acquisition. 3D images and roughness data were acquired using an Alicona Infinite Focus 3D microscope, also after coating to reduce the diffuse scattering of the white ZnO and to enhance the image quality. The lateral resolution was 2 μm and the vertical resolution was 100 nm. On each sample, the data from a projected area of 1.04 x 0.54 mm^2 was measured and analyzed with the internal software provided by Alicona for surface roughness. It is important to note that the 3D microscope's resolution is much larger than the average nanoparticle size, thus, the calculations for roughness and conclusions derived from these calculations pertain to differences in microstructure only and not in the underlying nanostructure.

A Canon T3i camera with a Sigma 70-300 mm lens and a Raynox DCR-150 macro lens was used to capture photographs of droplets on various surfaces. For contact angle measurements, a KSV CAM200 goniometer was employed. Water contact angle measurements used a 15 μL droplet size, whereas oil droplets were 5 μL in volume, the smallest dispensable quantities from the goniometer's custom micropipette, respectively. Static contact angle (SCA) was measured immediately after droplet deposition. Measurements are an average based on 10

images of a sample (acquisition rate: 1 image per second), for 3 different samples of each type made. This was done to ensure consistency in the spraying method and reproducibility across samples. The sliding angles were measured on a ThorLabs Goniometer stage by placing the droplet on the sample and then slowly tilting the stage until the droplet started moving. The angle was recorded and the measurement repeated for a minimum of 4 times to determine sliding angles. The droplet volumes were similar to those reported above for contact angle measurements.

Attenuated-total reflectance infrared spectroscopy (ATR-IR) was carried out using a Perkin Elmer 100 IR Spectrometer. A coated silicon wafer was placed facing the sample window. A pressure of 80-90 N was applied to each sample and 10 scans were averaged to ensure high signal-to-noise ratio.

X-ray photoelectron spectroscopy (XPS) was carried out on a Kratos Axis ULTRA photoelectron spectrometer using a monochromatic Al Kα source. Survey spectra were collected at a constant pass energy of 160 eV. Spectra of the C(1s), Si(2p), and F(1s) core levels were collected at a pass energy of 40 eV and used to determine the relative atomic percentage of each of those elements.

2.3 Results and Discussion

Spray-coating is a simple and effective method of coating a substrate because it is inexpensive, easily scalable, and applicable to a variety of surfaces.[30] The versatility of this approach permits any number of treatments to be applied to a single type of roughened surface. The spraying procedure employed in these experiments used a range of ZnO to PDMS ratios in

order to investigate the effects of roughness on the contact angles of water and the refrigeration lubricant, RL-68H. Nanoparticle ZnO was to confer roughness to the surface, and PDMS acted as a polymer binder and hydrophobic contact surface. As a control, contact angles were also measured on a flat silicon wafer sprayed with PDMS. Since the flat PDMS coated wafer is relatively smooth, changes in contact angle of the ZnO modified surfaces can be attributed purely to changes in roughness.

Our coating process can be applied to a wide variety of substrates, including flat silicon wafer, stock aluminium sheet, copper mesh, and cellulose filter paper. Silicon wafers are not an essential substrate, but were examined in detail in order to make comparisons to prior studies of omniphobic coatings.[13, 15, 18] As shown in **Figure 2.4**, superhydrophobic behavior is observed for all four substrates with the same ZnO nanoparticle/PDMS coating.

The effect of modifying the surface energy was investigated by comparing ZnO:PDMS surfaces on silicon wafers to fluorocarbon over-coated counterparts. By comparing the liquid contact angles, we can compare the effects of surface roughness to the effects of changes in surface energy due to the over-coating for substrates of comparable roughness. For such comparisons, Teflon AF and perfluorodecyltrichlorosilane (FDTS) were each deposited from the liquid-phase onto ZnO:PDMS surfaces. Although FDTS has a lower critical surface energy (γ_c) than Teflon AF (12 mN/m vs. 16 mN/m), it only reacts with surface hydroxyl groups, forming a siloxane bond. Because the density of surface hydroxyl groups on the ZnO is limited, there is a trade-off with FDTS between the density of the total surface coverage vs. a lower γ_c. To improve the surface coverage, we plasma-oxidized samples before silanization to maximize the number of hydroxyl groups available for bonding. Examination of the Teflon AF and the FDTS surfaces

permits comparison between a non-covalent vs. covalent over-coating procedures in terms of contact angles and sliding angles.

One might be tempted to incorporate low surface energy fluorochemicals into the initial polymeric binder rather than apply them as a second overcoat. Such an approach has two problems: First, bulk incorporation of a fluorocarbon does not guarantee that the fluorocarbon is actually present at the exposed surface. Second, large loadings of fluorochemicals into the polymeric binder would be necessary and the resulting composite may be dispersible only in expensive fluorinated solvents.[31-33] In addition, excessive use of fluorocarbons in general can be problematic because many fluorochemicals are precursors to perfluorooctanoic acid, a known toxic bioaccumulant.[34] By separating the spray-coating and top-coating steps, the fluorocarbon is inherently on the contact surface and the amount of fluorocarbons necessary to coat the surface is greatly reduced.

2.3.1 SEM and 3D Microscope Characterization

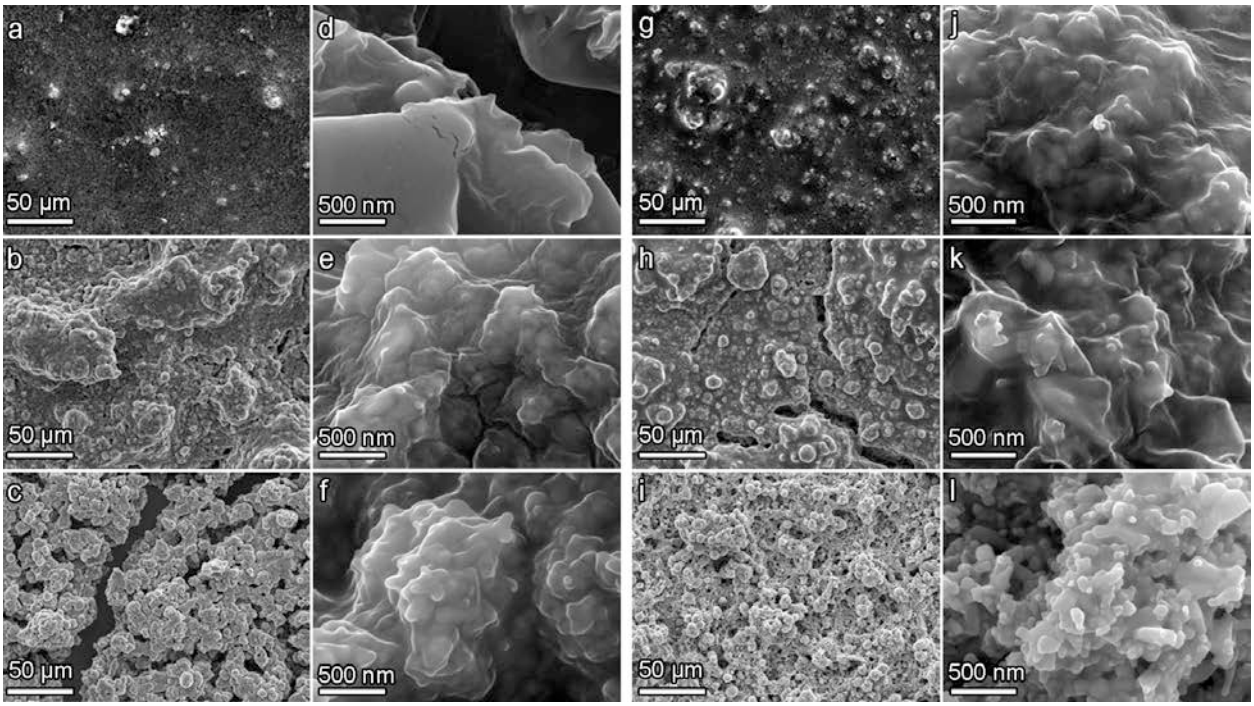

Figure 2.5 SEM images of spray coatings of ZnO:PDMS at ratios of 1:2 (a and d), 1:1 (b and e) and 2:1 (c and f). Note the texturing at both the micro- and nano-scale. SEM images of spray coatings of ZnO:PDMS with a top-coating of Teflon AF at ratios of 1:2 (g and j), 1:1 (h and k) and 2:1 (i and l).

Figure 2.5a-f shows SEM images of all ratios of ZnO:PDMS without a Teflon AF coating. As the relative amount of PDMS decreases compared to ZnO, an increase in texturing, due to increasing exposure of ZnO nanoparticles, can clearly be seen (e.g., **Figure 2.5**a vs. b vs. c). At a 2:1 ratio of ZnO:PDMS (**Figure 2.5** c,f), individual nanoparticles protrude from the PDMS film, and a hierarchical roughness is observed that can best be described as micro-scale ZnO:PDMS globules which themselves consist of nano-scale ZnO papules. These hierarchical structures (**Figure 2.5** c,f,i,l) produce an intrinsic multi-scale roughness with characteristic re-entrant structures necessary for omniphobicity with high contact angles and low roll-off angles.[35]

Figure 2.5g-l shows the same samples after they have been coated with Teflon AF and oven- cured. The same trend is observed as for the non-over-coated samples: higher relative ratios of ZnO produce a more textured surface and give a hierarchical structure. Compared to the samples without Teflon coating, more nano-scale ZnO papules emerge at the surface and increase the surface roughness (e.g., compare **Figure 2.5**f vs 2.5l). The high heat treatment necessary to cure the Teflon AF alter the topographical appearance of PDMS, as confirmed by separate heat treatment of non-fluorinated samples.

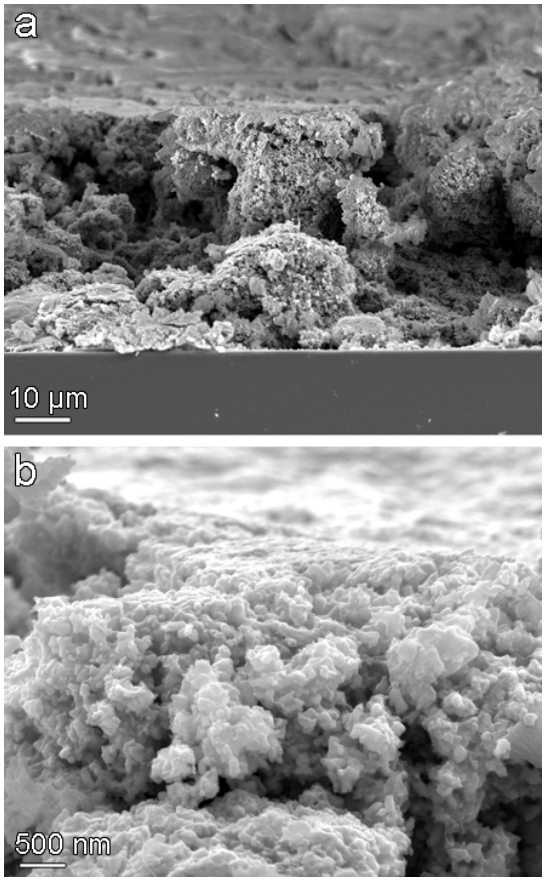

Figure 2.6 Cross-sectional SEM of a 2:1 ZnO:PDMS spray-coated silicon wafer. (a) Cavities are formed by the spraying process showing re-entrant curvature. (b) Close-up of such a cavity.

The initial aerosol droplets from the airbrush, which are tens of microns in diameter, deposit on the smooth Si surface. As the solvent evaporates, the ZnO nanoparticles and uncured PDMS coalesce. The PDMS then forms crosslinks as it cures and the final coating is produced. The emergence of hierarchical structures in the coating derives from the very different scales of the initial aerosol droplets (tens of μm) vs. the agglomeration of the ZnO nanoparticles-polymer composite as solvent evaporates (tens of nm). The spray process results in the formation of micro-scale re-entrant cavities, as can be seen in **Figure 2.6a**. A close-up of one of these cavities (**Figure 2.6b**) shows micro-scale globules with individual ZnO nanoparticles protruding from them, revealing the hierarchical roughness.

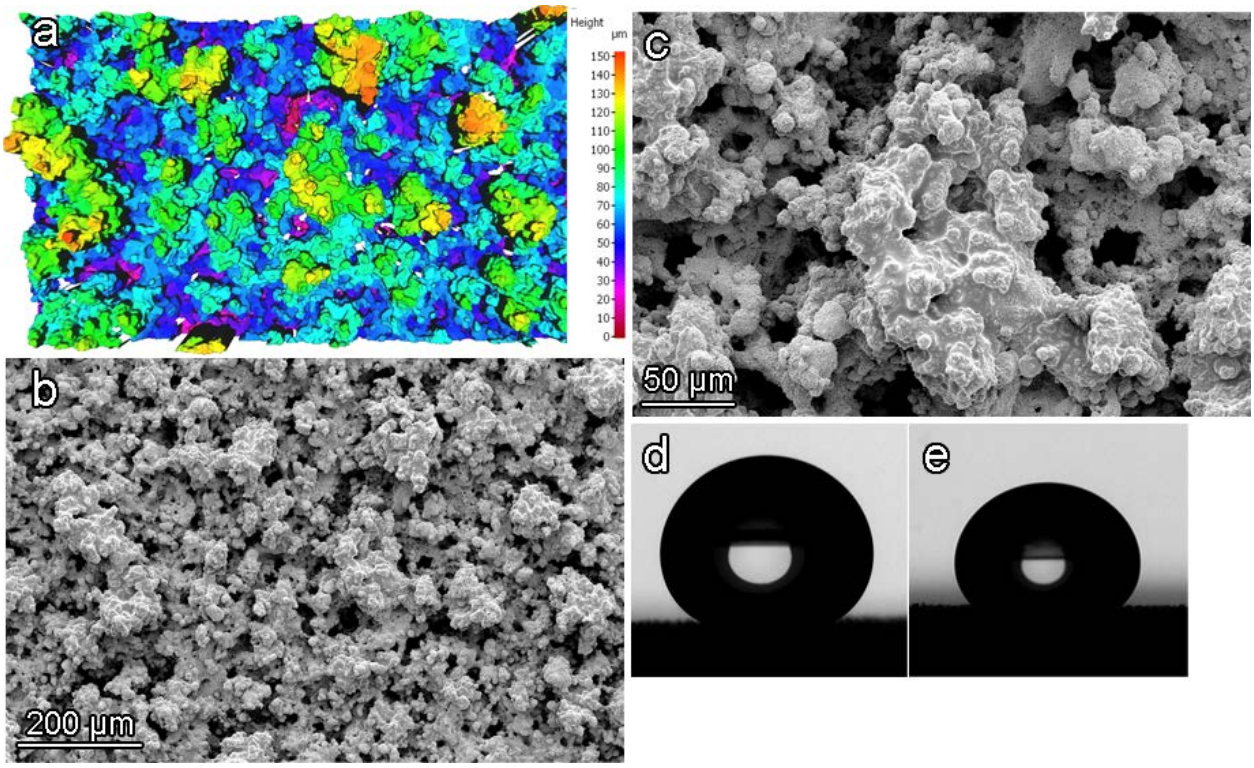

Figure 2.7 (a) 3D microscopic image of a 2:1 ZnO:PDMS surface coated with Teflon taken on an InfiniteFocus 3D microscope; the area scanned was 0.58 mm x 1.04 mm; the scale bar is 200 μm. (b) SEM image of the same area and (c) insert showing detailed micro- and nanostructures. Optical image of a (d) water droplet and (e) RL-68H droplet on the same surface.

Figure 2.7 shows a 3D micrograph with a colored z-gradient of a Teflon AF coated 2:1 ZnO:PDMS surface, with an accompanying SEM images of the same sample section with a projected area of 1.04 mm x 0.58 mm and a detailed view from the center of the section. Peaks and valleys ranging from 30-200 μm are formed by the spray procedure contributing to the micro-scale roughness of the surfaces. The SEM images reveal additional nano-scale roughness that cannot be captured by the InfiniteFocus optical microscope. The z-gradient mapping allows for a qualitative comparison of surface roughness between the different ZnO:PDMS mass ratios and over-coating procedures.

We are not limited to flat surfaces in our coating process. The spray deposition can be used to effectively coat complex textured surfaces. For example, the coating of a copper mesh is shown in **Figure 2.8**. The ZnO:PDMS coating forms the same hierarchically roughened structures discussed earlier (i.e. micro-globules of ZnO and PDMS on Si wafer). Similar structures are observed using the spray coating process on stock aluminium and cellulose filter paper as well (Figure 1).

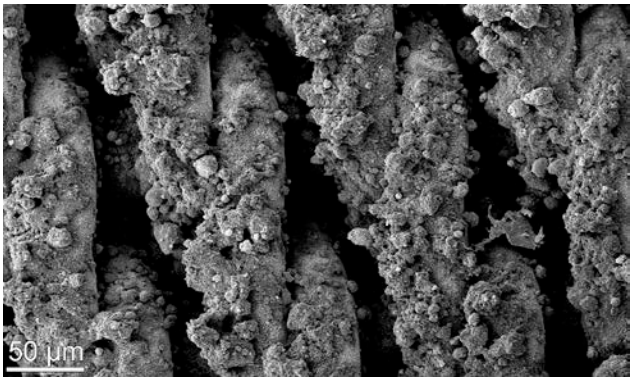

Figure 2.8 SEM of a copper mesh spray coated with a 2:1 solution of ZnO:PDMS.

2.3.2 Contact Angle Results

Table 2.1 Static contact angles of water and RL-68H on ZnO : PDMS coatings

ZnO : PDMS ratio	**Top coat**	***θ*, H_2O (°)**	***θ*, RL-68H (°)**
PDMS on flat Si	—	105 ± 2	Wetted, ~0
1 : 2	—	119 ± 11	Wetted, ~0
1 : 1	—	155 ± 2	60 ± 4
2 : 1	—	152 ± 6	Wetted, ~0

Table 2.1 shows the static contact angles of water and RL-68H the samples without Teflon AF coating. The 'PDMS on flat Si' sample, made by spraying a 25 mg/mL solution of PDMS onto a silicon wafer, acted as a flat reference sample with a similar surface chemistry as the samples with nanoparticles to study the effect of surface roughness on the contact angles. PDMS is intrinsically hydrophobic (surface energy = ~22 mN/m[36]), which leads to a SCA for water of 105°. RL-68H completely wets the surface. As the roughness of the samples increases, so does the water contact angle. In all cases, the de-wetting of water is improved by the spray-coating procedure when compared to the flat reference sample. On the 1:1 and 2:1 ZnO:PDMS, water contact angles of over >150° are achieved, indicating that the surfaces are highly hydrophobic, even without a fluorinated over-coating. The droplets are in the non-wetting Cassie-Baxter state.[37]

It is interesting to note that a non-zero contact angle for the refrigeration lubricant is obtained for a 1:1 ratio, yet the surfaces are completely wetted for the 2:1 and 1:2 ratios. This can be ascribed to a balance between the low surface energy from the PDMS (which would favor a lower ratio of ZnO to PDMS) versus the surface roughness from ZnO (which would favor a higher ratio). As will later be shown, the 1:1 ZnO:PDMS surfaces have a higher micro-scale

roughness than either the 2:1 or 1:2 mixtures. At either extreme, there is either not enough roughness and re-entrant structure (1:2) or not enough PDMS (2:1) to sustain droplet formation. Additionally, it is known that PDMS swells in the presence of many hydrocarbons,[36] which could explain the RL's affinity for the surface and the wetting at the low nanoparticle concentration.

Table 2.2 Static contact angles of water and RL-68H on ZnO : PDMS coatings with fluorinated overcoatings

ZnO : PDMS ratio	**Top coat**	***θ*, H_2O (°)**	***θ*, RL-68H (°)**
Flat Si	Teflon AF	120 ± 6	75 ± 3
1 : 2	Teflon AF	117 ± 3	79 ± 3
1 : 1	Teflon AF	156 ± 2	72 ± 4
2 : 1	Teflon AF	157 ± 2	137 ± 2
2 : 1	FDTS	126 ± 6	146 ± 5
2 : 1	FDTS, plasma-treated	144 ± 2	148 ± 2

Table 2.2 shows contact angles for Teflon-coated and fluorosilane-coated samples. The static contact angles on a smooth reference sample coated with Teflon AF are 120° for water and 75° for the lubrication oil. At a 1 : 2 ratio of ZnO : PDMS, the contact angles are almost identical to those of the smooth reference sample (*i.e.*, Teflon coated Si wafer), confirming that roughness is minimal. Water contact angles on the 1 : 1 and 2 : 1 samples are similar to those without the Teflon AF coating. Unlike on the non-fluorinated samples, RL-68H contact angles increase dramatically with increasing ZnO : PDMS ratios, reaching a SCA > 135° at the 2 : 1 ratio. By changing the overcoating to FDTS, the contact angles of RL-68H were increased even more.

Table 2.3 presents the sliding angles of water and RL-68H droplets. Water droplets do not slide on surfaces that were sprayed at ratios of 1:2 ZnO:PDMS, with or without a Teflon

overcoat. The low roughness and the few extruding nanoparticles on these samples pin the three-phase contact line and act as barriers to the movement of the droplet.[38] At 1:1 and 2:1 ZnO:PDMS ratios, both uncoated and Teflon-coated surfaces have sliding angles of 5° or less for water droplets. These surfaces are thus superhydrophobic.

Table 2.3 Sliding angles (α) of water and RL-68H on ZnO : PDMS coatings

ZnO : PDMS ratio	**Top coat**	***α*, H_2O (°)**	***α*, RL-68H (°)**
2 : 1	FDTS, plasma treated	5	17
2 : 1	FDTS	20	Pinned
2 : 1	Teflon AF	5	Pinned
2 : 1	None	2	Wetted
1 : 1	Teflon AF	5	Pinned
1 : 1	None	3	Pinned
1 : 2	Teflon AF	Pinned	Wetted
1 : 2	None	Pinned	Wetted

FDTS-coated samples, however, have a sliding angle with water of 20°. This is consistent with only partial coverage of the surface with FDTS, as noted earlier. When the 2:1 ZnO:PDMS sample is plasma-oxidized prior to silanization with FDTS, however, the water sliding angle achieve again sliding angles of 5°. RL-68H droplets were pinned (i.e., even when the surface was tilted by 90°, the droplet was immobile) on all surfaces except on the plasma-oxidized, silanized sample. Oil droplets slide off easily at an angle of 17°. RL-68H droplets move across this surface and leave no oily stains behind, indicating a highly de- wetted state (**Figure 2.9**).

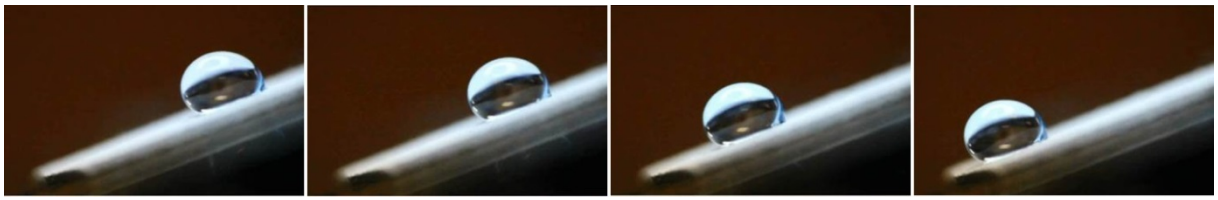

Figure 2.9 Images of an oil droplet sliding across a 2:1 ZnO:PDMS coated surface that was plasma-oxidized and functionalized with FDTS. Images were taken at 0 ms, 250 ms, 500 ms, and 750 ms from left to right, respectively.

Table 2.4 Contact (**θ)** and sliding (α) angles of milk on ZnO:PDMS samples

Sample (ZnO:PDMS)	**Top Coat**	**θ, Milk[a] (°)**	**α, Milk (°)**
1:2	None	87 ± 5	Pinned
1:1	None	120 ± 2	22
2:1	None	145 ± 4	3
1:2	Teflon	96 ± 6	Pinned
1:1	Teflon	125 ± 3	21
2:1	Teflon	147 ± 5	4
2:1	FDTS[b]	122 ± 15	See note
2:1	FDTS, plasma-treated	148 ± 2	3

[a]Surface tension of milk = 54 mN/m

[b]This sample produced erratic contact and sliding angles (α =>45, droplets pinned sometimes)

To provide further information on mechanism and scope of the surface interactions, we have also examined our surface interactions with milk, whose surface tension[39] (γ=54 mN/m) is intermediate between water and oil. Milk was used as an example of a more complex fluid and a good choice to show omniphobicity. Milk contains fats, proteins, sugars, and importantly its morphology is hydrophobic colloidal suspension in water. The results of surface contact angle measurements are shown in the table above and are generally close to those with water.

2.3.3 Surface Characterization

Table 2.5 Average height (S_a), maximum feature height (S_z), root-mean-squared gradient (S_{dq}) and roughness (r) of ZnO:PDMS samples[a]

Sample (ZnO:PDMS)	S_a (average height) [µm]	S_z (maximum feature height) [µm]	S_{dq} (rms gradient)[b]	r = A/A_{flat} [c]
1:2 – as-is	6.6	75	1.3	1.2
1:2 – Teflon	9.6	115	2.3	1.4
1:1 – as-is	32.5	255	11.1	3.3
1:1 – Teflon	33.1	239	11.0	3.3
2:1 – as-is	27.4	224	10.0	3.0
2:1 – Teflon	18.9	151	7.9	2.6
2:1 – Silane	18.2	146	4.7	2.3
2:1 – Silane[d]	10.3	92	3.2	2.0
ZnO only	10.0	83	3.8	2.0
PDMS only[e]	0.1	12	0.1	1.0

[a]Numbers represent the roughness values for an area of 0.58x1.04 mm² on each sample. Given the method of sample fabrication by random spraying, the roughness at other points of the sample might deviate from the reported values by up to ± 20%. The general trend between the samples, however, remains the same.

[b]S_{dq} refers to the root means squared change in slope of the area of the sample scanned.

[c]A / A_{flat} is the total area A of the rough sample divided by the projected area A_{flat}, (i.e. that of a flat silicon wafer).

[d]Plasma-oxidized before silanization.

[e]Numbers are based on very few data points, image acquisition was not possible due to high sample reflectance, and high flatness.

The surfaces of each of the spray coating formulations were characterized in several ways, as discussed in this section. The table above shows values for various parameters that were calculated from 3D microscope images that were taken over a cross-section of the spray coatings. The images used for calculating these values are shown below. As is expected, the roughness tends to increase as the amount of ZnO increases relative to PDMS. However, it is

interesting to note that the 1:1 samples gave higher roughness values than their 2:1 counterparts in all cases. The roughness captured is only on the micro-scale, as the 3D microscope does not have the resolution necessary to evaluate roughness due to individual ZnO nanoparticles. It is possible that the 2:1 samples have higher nano-roughness, but similar or lower micro-roughness (note that all values do have a reasonable error). Si The 3D images of the 1:1 and 2:1 samples look fairly similar (**Fig 2.10**), but the SEM images shown earlier qualitatively show an increase in roughness. The contact angle data further supports this conclusion, since the 2:1 samples gave higher contact angles for each of the liquids examined. As a final piece of evidence, when ZnO nanoparticles are sprayed onto a Si wafer with no PDMS at all, the roughness values are still lower than the 1:1 sample.

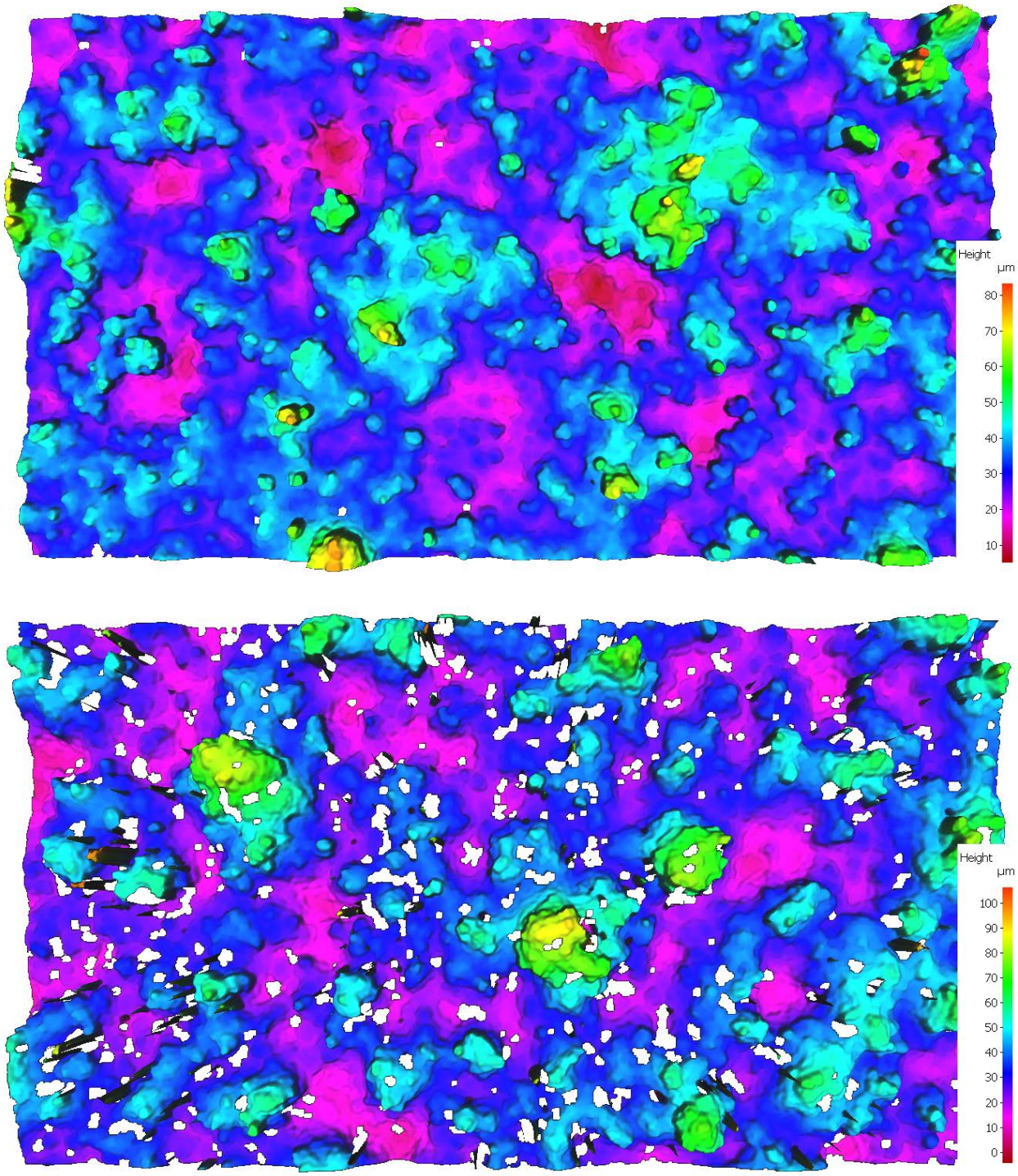

Figure 2.10a Topographical images taken with the Alicona 3D microscope of samples with a ratio of 1:2 ZnO:PDMS (top) and 1:2 ZnO:PDMS, Teflon overcoated (bottom). The white areas in the bottom image are data points that could not be picked up by the lens. These do not significantly affect the average roughness measurements given in **Table 2.5**.

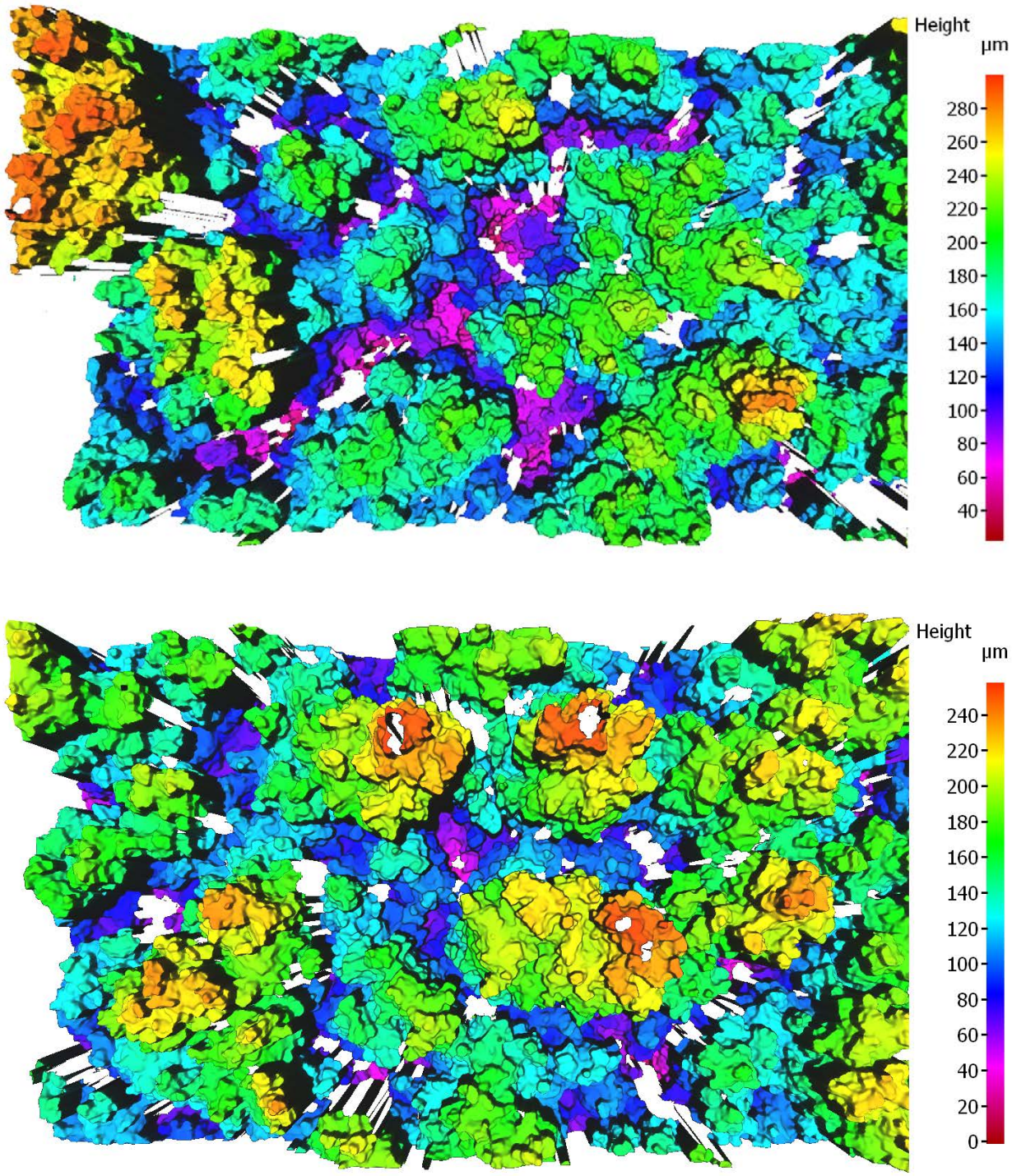

Figure 2.10b Topographical images taken with the Alicona 3D microscope of samples with a ratio of 1:1 ZnO:PDMS (top) and 1:1 ZnO:PDMS, Teflon overcoated (bottom). The white areas in the images are data points that could not be picked up by the lens. These do not significantly affect the average roughness measurements given in **Table 2.5**.

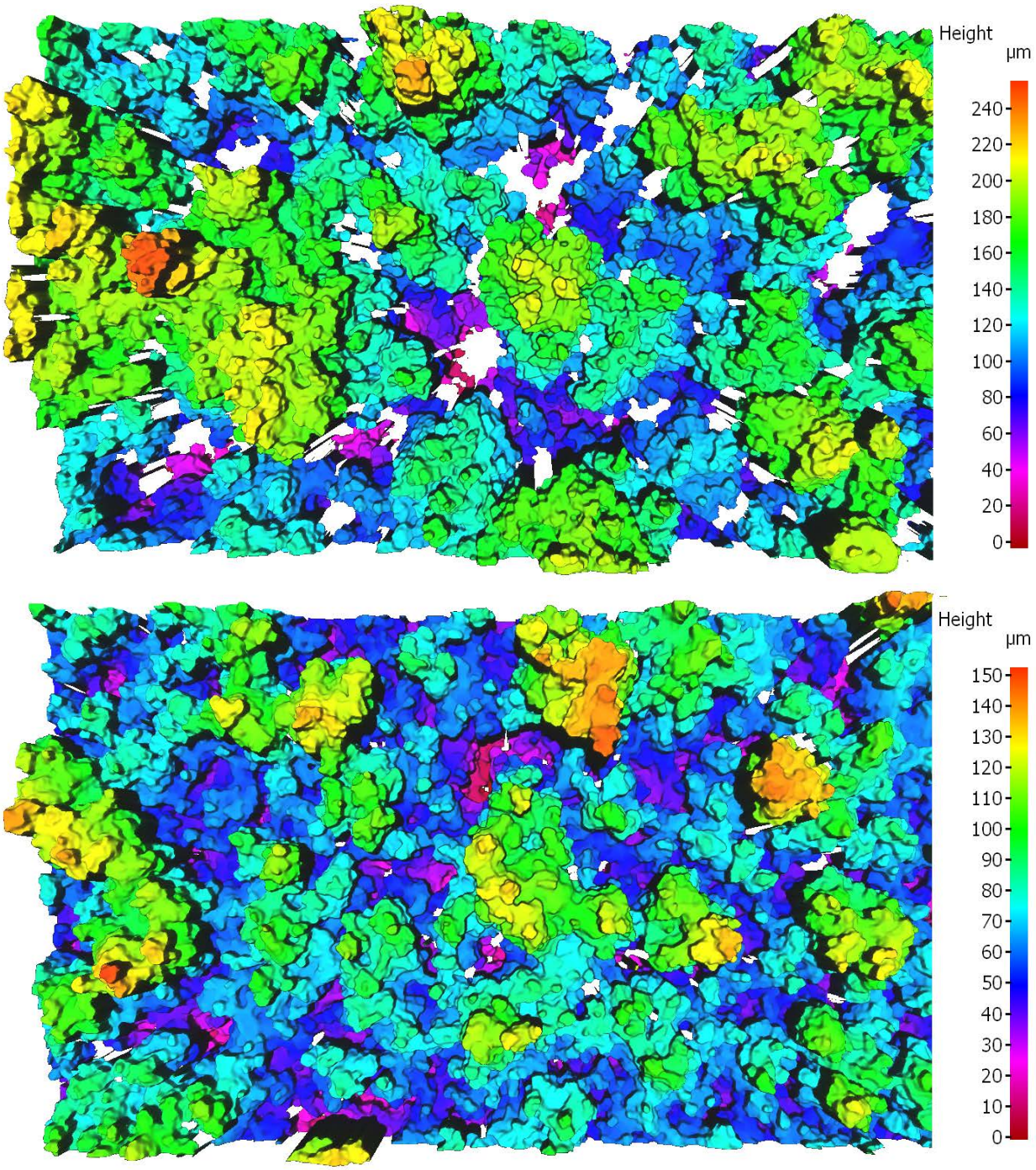

Figure 2.10c Topographical images taken with the Alicona 3D microscope of samples with a ratio of 2:1 ZnO:PDMS (top) and 2:1 ZnO:PDMS, Teflon overcoated (bottom). The white areas in the images are data points that could not be picked up by the lens. These do not significantly affect the average roughness measurements given in **Table 2.5**.

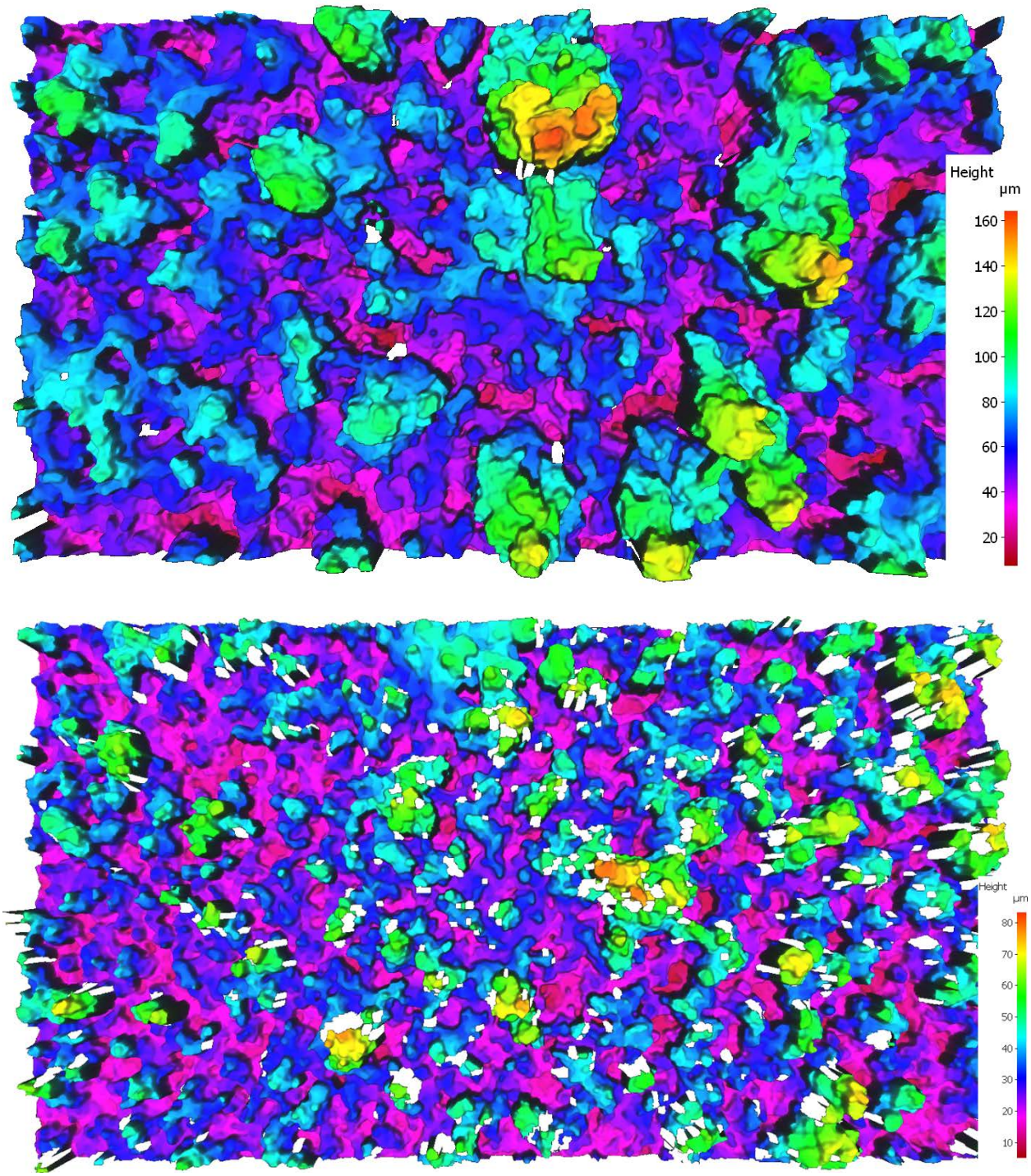

Figure 2.10d Topographical images taken with the Alicona 3D microscope of silanized samples with a ratio of 2:1 ZnO:PDMS, the bottom image was treated with O_2 plasma before silanization. The white areas in the images are data points that could not be picked up by the lens. These do not significantly affect the average roughness measurements given in **Table 2.5**.

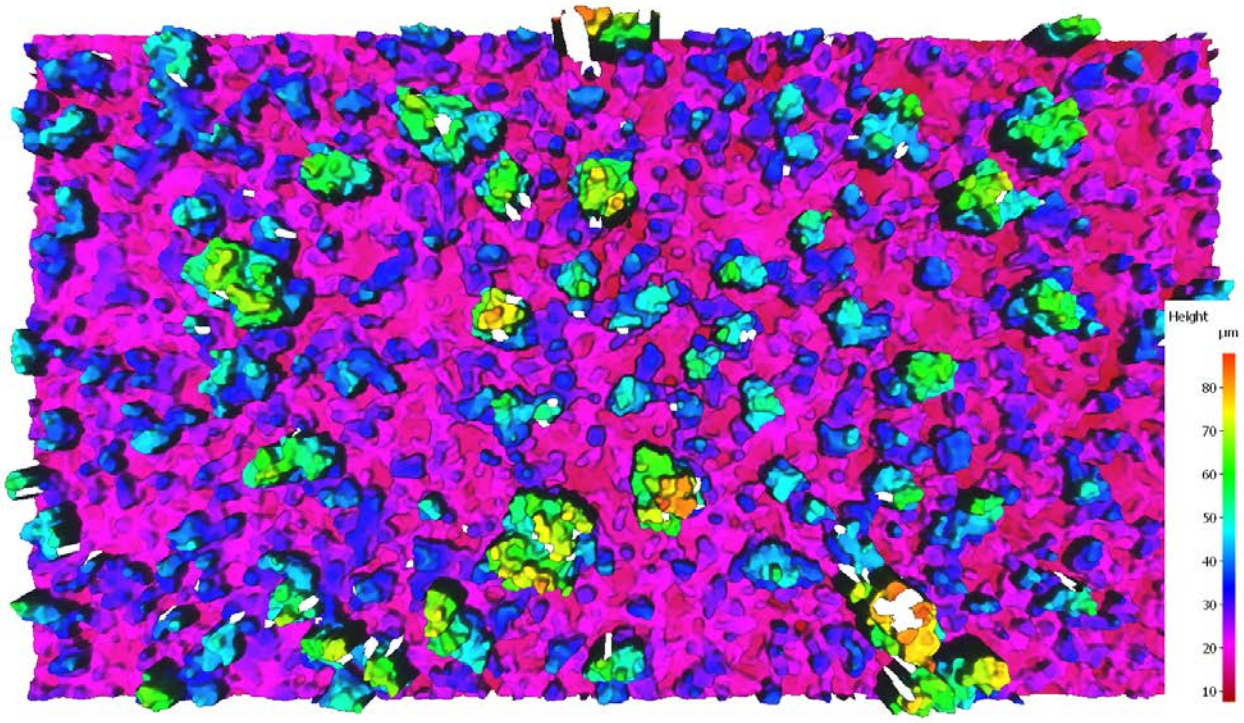

Figure 2.10e Topographical images taken with the Alicona 3D microscope of samples sprayed with ZnO nanoparticles only. The white areas in the images are data points that could not be picked up by the lens. These do not significantly affect the average roughness measurements given in **Table 2.5**.

2.3.3.1 ATR-IR Spectroscopy

IR spectroscopy shows that all of the surfaces are indeed very similar, though they behave very differently when in contact with liquid. A surface coated only with PDMS has the same IR peaks as a surface with ZnO, a Teflon over-coat or both. ZnO has no IR signal, and small Teflon peaks can be seen emerging at 1145 and 1245 wavenumbers. Other than that, the only major change occurs when an FDTS treatment is used instead of Teflon.

Interestingly, we saw in **Table 2.3** and **2.4** that the FDTS-treated sample has lower water and milk contact angles than RL-68H contact angles, despite the fact that the oil has a much lower surface tension than either. This may be due to hydroxyl groups present on the surface,

which can be a result of partially hydrolyzed silanes (i.e. Si-OH formation). OH stretches are visible in the broad 3500 band in the IR of this sample (**Figure 2.11**c). Polar OH groups raise the surface tension of the surface, but are compensated by the low surface energy of the FDTS itself. It is very important to note though, that polar groups tend to raise the *polar* component of surface tension as opposed to the dispersive (Van der Waals) component. Non-polar liquids, such as oils, tend to interact with the dispersive component,[40] whereas polar liquids, such as water and milk, interact strongly with polar groups via hydrogen bonding. Recent work has even exploited this idea by infusing ionic liquids into surfaces that can repel oils.[41] This does not occur when the sample is plasma-oxidized before silanization, evidenced by the lack of OH stretches (**Figure 2.11**c). Plasma oxidation generates OH groups for the silane to react with so that it can bond to the surface. Additionally, water molecules are very small compared to the RL-68H or FDTS, meaning that they may be able to align themselves favorably to unreacted hydroxyl groups.

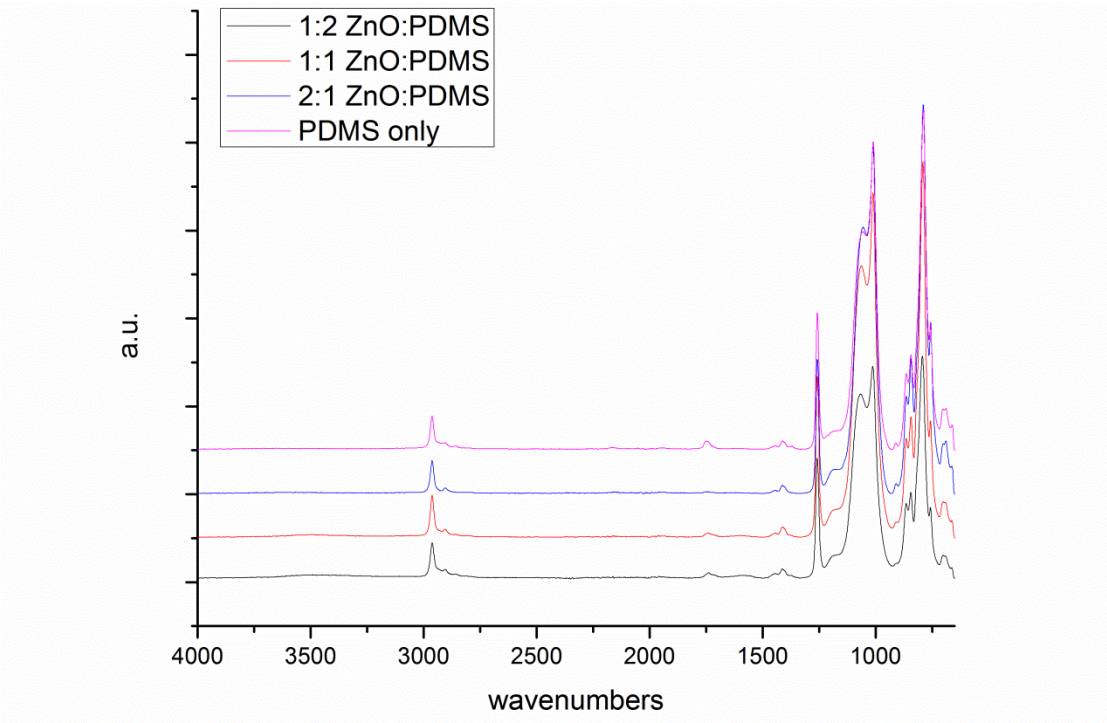

Figure 2.11a ATR-IR of ZnO:PDMS coatings and that of PDMS only.

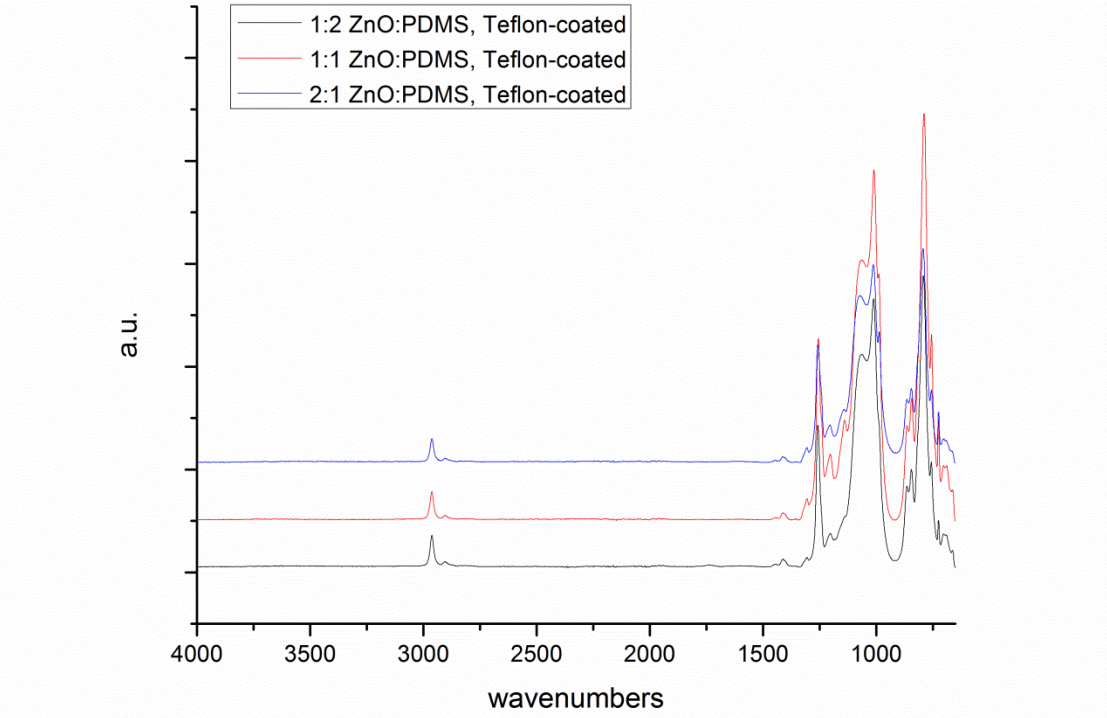

Figure 2.11b ATR-IR of ZnO:PDMS coatings that were overcoated with Teflon AF.

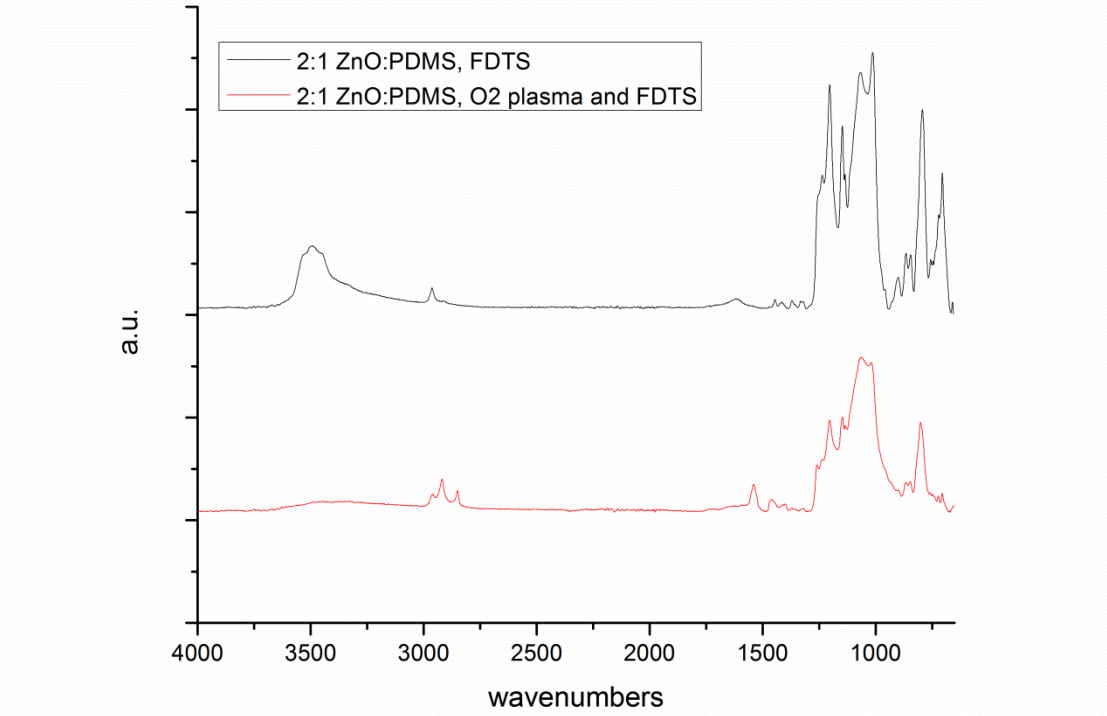

Figure 2.11c ATR-IR of ZnO:PDMS coatings and that were overcoated with FDTS.

2.3.3.2 XPS Data

Table 2.6 Relative atomic percentages (at. %) of C, Si and F on the surface of ZnO:PDMS samples, as determined by x-ray photoelectron spectroscopy. O and H components are not accounted for in these analyses.

Sample (ZnO:PDMS)	Top Coat	C (rel. at. %)	Si (rel. at. %)	F (rel. at. %)
1:2	None	68	32	0
1:1	None	68	31	1
2:1	None	73	26	1
1:2	Teflon	53	20	27
1:1	Teflon	44	11	45
2:1	Teflon	43	11	46
2:1	FDTS	54	6	39
2:1	FDTS, plasma-treated	36	3	61

Liquid-repellent behavior is correlated first and foremost with surface energy, and then with roughness. This is corroborated by the fact that the FDTS-coated samples (which have lower surface energy) are more omniphobic than their Teflon-coated counterparts (which were on average, rougher, see **Table 2.5**). Surface energy itself seems to highly correlate with the amount of fluorocarbons present on the surface, as evidenced by **Table 2.6**. Our most omniphobic sample also contained the highest fluorine content. This is also corroborated by the IR data, which show more prominent peaks for C-F stretches than their Teflon-counterparts. The roughness, while correlated to the ZnO:PDMS ratio, does not affect the actual composition of the surface, which consists mostly of PDMS (**Figure 2.11a**).

2.3.4 Comparison to Literature Reports

Table 2.7 Literature Reports of Liquid-Repellent Nanoparticle and Spray Coatings

Omniphobic coating	Method of deposition	Liquids tested	Static Contact Angles (SCA) / Sliding Angles (α)
ZnO nanoparticles and fluorocarbon-methacrylate copolymer[40]	Sprayed onto glass slides	Water (γ =72.6 mN/m) Hydraulic oil (γ =n.r.) Hexadecane (γ =27.5 mN/m)	SCA >150° for all liquids; sliding angles not reported.
ZnO nanoparticles with quaternary amine surfactant[41]	Sprayed onto micro-molded PDMS substrate, then functionalized with fluorosilanes	Water (γ =72.6 mN/m)	SCA >150°, $\alpha < 2°$
ZnO nanostructures with fluorosilane[29]	Nanostructures made via chemical bath deposition onto silicon wafer	Water (γ =72.6 mN/m) 30 % aq. ethanol (γ =35 mN/m)	SCA ~ 160° SCA ~ 145°, $\alpha = 10°$
Fluoroalkyl-functionalized silica + 20 wt% added fluorocarbon[32]	Sprayed onto flat wafer	Water (γ =72.6 mN/m) Diiodomethane (γ =50.8 mN/m) Rapeseed Oil (γ =35.5 mN/m.) Hexadecane (γ = 27.5 mN/m)	SCA ~ 165°, $\alpha < 5°$ SCA ~ 151°, $\alpha < 5°$ SCA ~ 153°, $\alpha \sim 10°$ SCA ~ 150°, $\alpha \sim 25°$
Current Work:	Sprayed onto flat wafer	Water (γ =72.6 mN/m)	SCA ~ 144°, $\alpha < 5°$
ZnO/PDMS + FDTS		Milk, 1% fat (γ =54 mN/m) RL-68H (γ =27.7 mN/m)	SCA ~ 148°, $\alpha < 5°$ SCA ~ 148°, $\alpha \sim 17°$

Previous publications report progress omniphobic ZnO-based coatings[32, 42-44] as given in **Table 2.7**. Steele and coworkers pioneered the fabrication of an omniphobic surface based on a sprayable solution of nanoparticle ZnO with a perfluorinated methacrylic copolymer (PMC) dispersed in acetone.[43] When comparing contact angle data, they achieved results similar to ours but no sliding angle data was reported.

In subsequent work, however, Steele and coworkers noted that their PMC/ZnO solution cured in an uneven coating when applied to a micro-molded PDMS substrate and sometimes left hydrophilic regions on the surface.[44] This multistep process required (1) prior fabrication of micro-posts of PDMS, (2) followed by fluorosilane deposition, (3) modified with dispersion onto the surface of a surfactant solution containing nanoparticle ZnO, and (4) completed with a final treatment with fluorosilane deposition. The contact and sliding angle data for water droplets are similar to our data, but neither oils nor low surface- tension liquids were tested.

Perry and co-workers synthesized ZnO nanostructures using a chemical bath deposition on a silicon wafer, which was then functionalized either with a C_4F_8 plasma or by treatment with FDTS.[42] They achieved high contact angles and low sliding angles for water droplets and aqueous ethanol droplets; aqueous ethanol has significantly higher surface tensions than RL-68H and no tests were reported for alkanes, oils or other low surface-tension liquids.

Lastly, Campos et al. used fluoroalkyl-functionalized silica instead of ZnO nanoparticles in an ETP-600S fluoropolymer matrix to study the effect of the particle mass fraction on contact angles and sliding angles of water, diiodomethane, rapeseed oil and hexadecane.[32] Hexadecane (similar surface tension to RL-68H) showed similar contact angles as the oil in our study, however, the sliding angles were somewhat higher than that obtained in the present study. The

present work improves upon both the fabrication of omniphobic surfaces as well as their application to oils.

2.4 Conclusions

In conclusion, we have developed a sprayable ZnO-PDMS composite that make surfaces superhydrophobic. In addition, an overcoating of Teflon AF or FDTS increases liquid repellency of the sprayed surfaces and renders them omniphobic. The ease of use, and scalability of this procedure make it an attractive option for a variety of surfaces that would otherwise be difficult to coat. We report static contact angles of ~150° for water and the refrigeration oil RL-68H. Water droplet mobility is excellent on the superhydrophobic surfaces with a ratio of ZnO to PDMS of at least 1:1. Highest contact angles with the oil are achieved with a 2:1 ZnO:PDMS mixture. By functionalizing the surface with plasma oxidation and silanization, oil sliding angles as low as 17° were achieved. Future work aimed at promoting droplet condensation in refrigeration condensers, however, will need to focus on fabricating surfaces that repel liquids with even lower surface tensions.

2.5 References

1) L. Gao and T. J. McCarthy. The “lotus effect” explained: two reasons why two length scales of topography are important. *Langmuir*, 2006, **22**, 2966-2967.

2) A. Marmur. The lotus effect: superhydrophobicity and metastability. *Langmuir*, 2004, **20**, 3517-3519.

3) N. A. Patankar. Mimicking the lotus effect: influence of double roughness structures and slender pillars. *Langmuir*, 2004, **20**, 8209-8213.

4) T. Young. An essay on the cohesion of fluids. *Philosophical Transactions of the Royal Society of London*, 1805, **95**, 65-87.

5) W. Barthlott and C. Neinhuis. Purity of the sacred lotus, or escape from contamination in biological surfaces. *Planta*, 1997, **202**, 1-8.

6) R. N. Wenzel. Resistance of solid surfaces to wetting by water. *Industrial & Engineering Chemistry*, 1936, **28**, 988-994.

7) A. Cassie. Contact angles. *Discussions of the Faraday Society*, 1948, **3**, 11-16.

8) R. Fürstner, W. Barthlott, C. Neinhuis and P. Walzel. Wetting and self-cleaning properties of artificial superhydrophobic surfaces. *Langmuir*, 2005, **21**, 956-961.

9) S. Nishimoto and B. Bhushan. Bioinspired self-cleaning surfaces with superhydrophobicity, superoleophobicity, and superhydrophilicity. *RSC Adv.*, 2013, **3**, 671-690.

10) T. Sun, L. Feng, X. Gao and L. Jiang. Bioinspired surfaces with special wettability. *Acc. Chem. Res.*, 2005, **38**, 644-652.

11) A. Tuteja, W. Choi, G. H. McKinley, R. E. Cohen and M. F. Rubner. Design parameters for superhydrophobicity and superoleophobicity. *MRS Bull.*, 2008, **33**, 752-758.

12) D. Quéré. Wetting and roughness. *Annu. Rev. Mater. Res.*, 2008, **38**, 71-99.

13) T. L. Liu and C. Kim. Repellent surfaces. Turning a surface superrepellent even to completely wetting liquids. *Science*, 2014, **346**, 1096-1100.

14) A. Tuteja, W. Choi, M. Ma, J. M. Mabry, S. A. Mazzella, G. C. Rutledge, G. H. McKinley and R. E. Cohen. Designing superoleophobic surfaces. *Science*, 2007, **318**, 1618-1622.

15) A. Tuteja, W. Choi, J. M. Mabry, G. H. McKinley and R. E. Cohen. Robust omniphobic surfaces. *Proc. Nat. Acad. Sci.*, 2008, **105**, 18200-18205.

16) T. Darmanin and F. Guittard. One-pot method for build-up nanoporous super oil-repellent films. *J. Colloid Interface Sci.*, 2009, **335**, 146-149.

17) T. Darmanin and F. Guittard. Highly hydrophobic films with various adhesion by electrodeposition of poly(3, 4-bis(alkoxy)thiophenes). *Soft Matter*, 2013, **9**, 1500-1505.

18) L. Cao, T. P. Price, M. Weiss and D. Gao. Super water-and oil-repellent surfaces on intrinsically hydrophilic and oleophilic porous silicon films. *Langmuir*, 2008, **24**, 1640-1643.

19) R. Dufour, M. Harnois, Y. Coffinier, V. Thomy, R. Boukherroub and V. Senez. Engineering sticky superomniphobic surfaces on transparent and flexible PDMS substrate. *Langmuir*, 2010, **26**, 17242-17247.

20) K. Golovin, D. H. Lee, J. M. Mabry and A. Tuteja. Transparent, Flexible, Superomniphobic Surfaces with Ultra-Low Contact Angle Hysteresis. *Angew. Chem., Int. Ed.*, 2013, **52**, 13007-13011.

21) A. Grigoryev, I. Tokarev, K. G. Kornev, I. Luzinov and S. Minko. Superomniphobic magnetic microtextures with remote wetting control. *J. Am. Chem. Soc.*, 2012, **134**, 12916-12919.

22) H. Kim, K. Noh, C. Choi, J. Khamwannah, D. Villwock and S. Jin. Extreme superomniphobicity of multiwalled 8 nm TiO_2 nanotubes. *Langmuir*, 2011, **27**, 10191-10196.

23) S. P. Kobaku, A. K. Kota, D. H. Lee, J. M. Mabry and A. Tuteja. Patterned Superomniphobic–Superomniphilic Surfaces: Templates for Site-Selective Self-Assembly. *Angew. Chem., Int. Ed.*, 2012, **51**, 10109-10113.

24) G. Soliveri, R. Annunziata, S. Ardizzone, G. Cappelletti and D. Meroni. Multiscale rough Titania films with patterned hydrophobic/oleophobic features. *J. Phys. Chem. C*, 2012, **116**, 26405-26413.

25) B. B. J. Basu and A. K. Paranthaman. A simple method for the preparation of superhydrophobic PVDF–HMFS hybrid composite coatings. *Applied Surface Science*, 2009, **255**, 4479-4483.

26) J. Li, L. Yan, Q. Ouyang, F. Zha, Z. Jing, X. Li and Z. Lei. Facile fabrication of translucent superamphiphobic coating on paper to prevent liquid pollution. *Chemical Engineering Journal*, 2014, **246**, 238-243.

27) H. Ogihara, J. Xie, J. Okagaki and T. Saji. Simple method for preparing superhydrophobic paper: spray-deposited hydrophobic silica nanoparticle coatings exhibit high water-repellency and transparency. *Langmuir*, 2012, **28**, 4605-4608.

28) W. Wu, X. Wang, X. Liu and F. Zhou. Spray-coated fluorine-free superhydrophobic coatings with easy repairability and applicability. *ACS applied materials & interfaces*, 2009, **1**, 1656-1661.

29) M. A. Kedzierski and M. Gong, *Effect of CuO nanolubricant on R134a pool boiling heat transfer with extensive measurement and analysis details*, Report NISTIR 7454, National Institute of Standards and Technology, Gaithersburg, MD, 2007.

30) A. Lefebvre. *Atomization and Sprays*, Taylor & Francis, New York, 1989.

31) S. Srinivasan, S. S. Chhatre, J. M. Mabry, R. E. Cohen and G. H. McKinley. Solution spraying of poly (methyl methacrylate) blends to fabricate microtextured, superoleophobic surfaces. *Polymer*, 2011, **52**, 3209-3218.

32) R. Campos, A. J. Guenthner, A. J. Meuler, A. Tuteja, R. E. Cohen, G. H. McKinley, T. S. Haddad and J. M. Mabry. Superoleophobic surfaces through control of sprayed-on stochastic topography. *Langmuir*, 2012, **28**, 9834-9841.

33) J. M. Mabry, A. Vij, S. T. Iacono and B. D. Viers. Fluorinated Polyhedral Oligomeric Silsesquioxanes (F-POSS). *Angew. Chem., Int. Ed.*, 2008, **47**, 4137-4140.

34) R. Renner. Growing concern over perfluorinated chemicals. *Environmental science & technology*, 2001, **35**, 154A-160A.

35) A. Marmur. From hygrophilic to superhygrophobic: theoretical conditions for making high-contact-angle surfaces from low-contact-angle materials. *Langmuir*, 2008, **24**, 7573-7579.

36) J. N. Lee, C. Park and G. M. Whitesides. Solvent compatibility of poly (dimethylsiloxane)-based microfluidic devices. *Anal. Chem.*, 2003, **75**, 6544-6554.

37) R. J. Vrancken, H. Kusumaatmaja, K. Hermans, A. M. Prenen, O. Pierre-Louis, C. W. Bastiaansen and D. J. Broer. Fully reversible transition from Wenzel to Cassie− Baxter states on corrugated superhydrophobic surfaces. *Langmuir*, 2009, **26**, 3335-3341.

38) L. Barbieri, E. Wagner and P. Hoffmann. Water wetting transition parameters of perfluorinated substrates with periodically distributed flat-top microscale obstacles. *Langmuir*, 2007, **23**, 1723-1734.

39) A. J. Bertsch. Surface tension of whole and skim-milk between 18 and 135 C. *Journal of Dairy Research*, 1983, **50**, 259-267.

40) F. M. Fowkes. Attractive forces at interfaces. *Industrial & Engineering Chemistry*, 1964, **56**, 40-52.

41) D. F. Miranda, C. Urata, B. Masheder, G. J. Dunderdale, M. Yagihashi and A. Hozumi. Physically and chemically stable ionic liquid-infused textured surfaces showing excellent dynamic omniphobicity. *APL Materials*, 2014, **2**, 056108.

42) G. Perry, Y. Coffinier, V. Thomy and R. Boukherroub. Sliding droplets on superomniphobic zinc oxide nanostructures. *Langmuir*, 2012, **28**, 389-395.

43) A. Steele, I. Bayer and E. Loth. Inherently superoleophobic nanocomposite coatings by spray atomization. *Nano Lett.*, 2009, **9**, 501-505.

44) A. Steele, I. Bayer, S. Moran, A. Cannon, W. P. King and E. Loth. Conformal ZnO nanocomposite coatings on micro-patterned surfaces for superhydrophobicity. *Thin Solid Films*, 2010, **518**, 5426-5431.

CHAPTER 3: SILICONE MICROSPHERES VIA ULTRASONIC SPRAY PYROLYSIS

3.1 Introduction

This chapter is taken in part from the following references:

Rankin, J. M.; Neelakantan, N. K.; Lundberg, K. E.; Grzincic, E. M.; Murphy, C. J.; Suslick, K. S. Magnetic, Fluorescent, and Copolymeric Silicone Microspheres. *Advanced Science* 2015, **2**, 1500114.

Suslick, K. S.; Neelakantan, N. K.; Rankin, J. M. Methods of Producing Silicone Microspheres. U. S. Patent Appl. 15/004016*;* 2016.

Silicones are an ideal polymer for use in biomedical applications due to their biocompatibility, inertness and chemical resistance. Interestingly, very few reports of the synthesis of PDMS microspheres exist in the literature even though they are promising materials for drug delivery or carriers for pharmaceutical agents.[1-8] Problems with current synthetic methods (**Figure 3.1**) include particle agglomeration, emulsion instability, and low product yield. This is due to the low surface energy of PDMS as well as the high temperatures necessary for polymerization to occur.

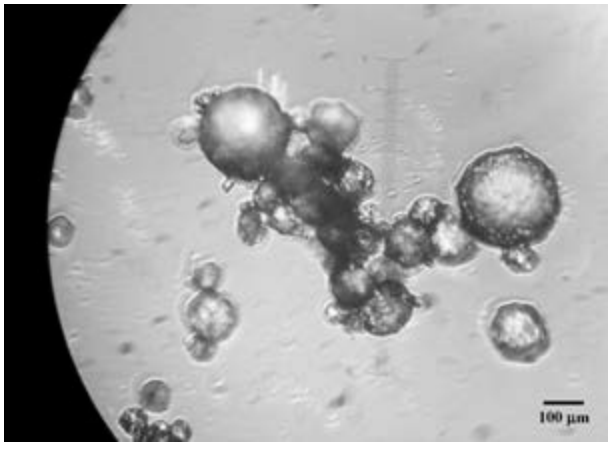

Figure 3.1 Highly agglomerated PDMS microspheres, produced via an emulsion route.[5]

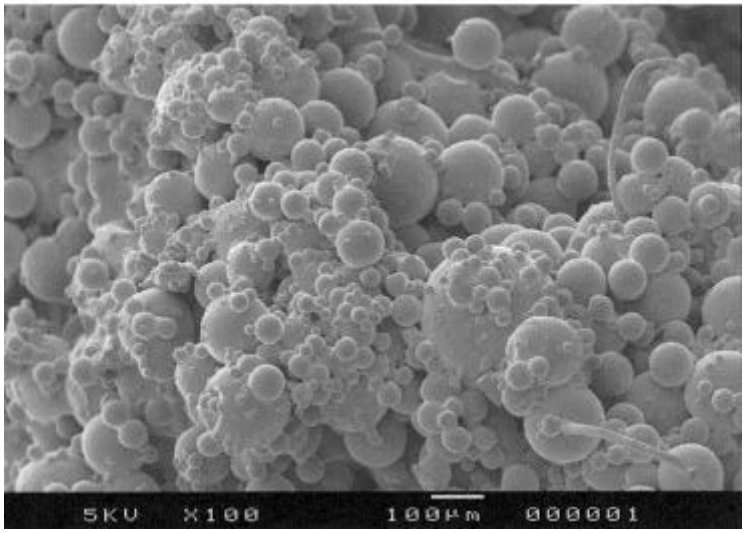

Figure 3.2 PDMS microspheres made from a heptane-water emulsion. Note the polydispersity and large size (>50 µm) of most microspheres.[9]

For instance, the above attempt relied on heptane-water emulsion to stabilize spherical PDMS colloids in solution[9] (**Figure 3.2**). A lipophilic surfactant acts to prevent agglomeration of PDMS colloids. These colloids would then cure with heating and stirring. As seen above, the wide range of microsphere sizes renders this method nonviable for many applications. Supposing one were to use PDMS microspheres as part of an injectable, they would need to pass through blood vessels and capillaries, which means they need to be around the same size as a blood cell, which is about 7 µm in diameter.

Other groups have attempted to use microfluidics with or without ferrofluids, for instance, to control the size of the cured PDMS particles. Two examples are shown on the following page.[7, 10]

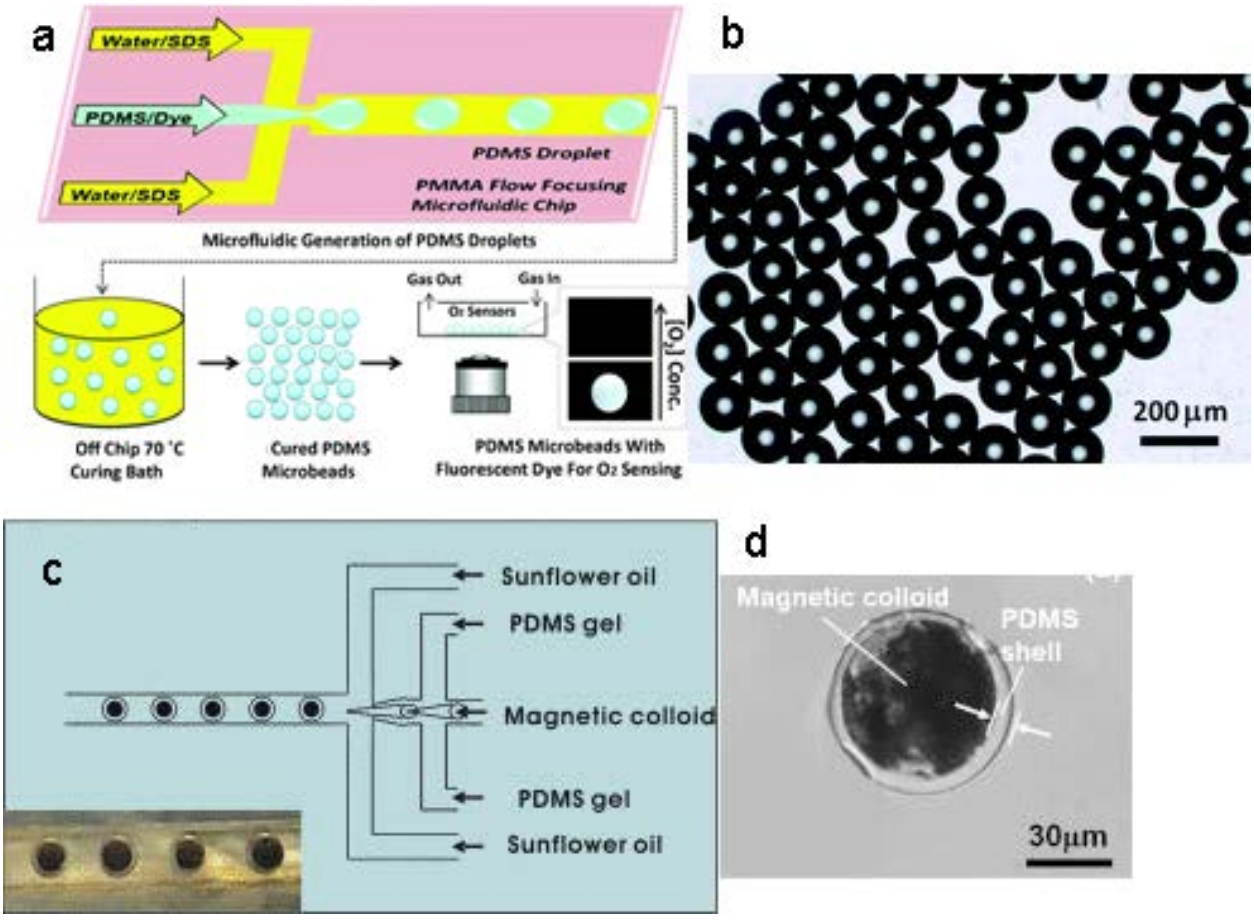

Figure 3.3 a) Schematic for microfluidic production of fluorescent PDMS microbeads for oxygen sensing. b) Optical microscope images of cured PDMS microbeads from (a). c) Schematic for microfluidic production of magnetically responsive microspheres, using a similar multi-flow strategy. D) Optical image of the resultant core-shell product.[7, 10]

In the first example[10] (**Figure 3.3** a,b), a sodium dodecylsulfate solution was flowed through a microfluidic channel along two outer channels, while the inner channel injected uncured PDMS droplets. These droplets could be cured into highly monodisperse microspheres. In addition these microspheres could be made fluorescent. In the second example (**Figure 3.3** c,d), a magnetic core is coated by PDMS gel, and guided through a microfluidic channel.[7] The composite sphere is then cured in a heat bath. In both cases, the product is 30 µm in diameter at

best, far larger than usable for most practical medical applications. Additionally, the throughput is effectively limited to a one-at-a-time production per microfluidic channel. As we will see, the work described in this chapter produces far smaller functionalized microspheres with far higher throughput and yield, by using a simple spray pyrolysis technique, be they magnetic, fluorescent, etc.[11, 12]

3.1.1 Ultrasonic Spray Pyrolysis (USP)

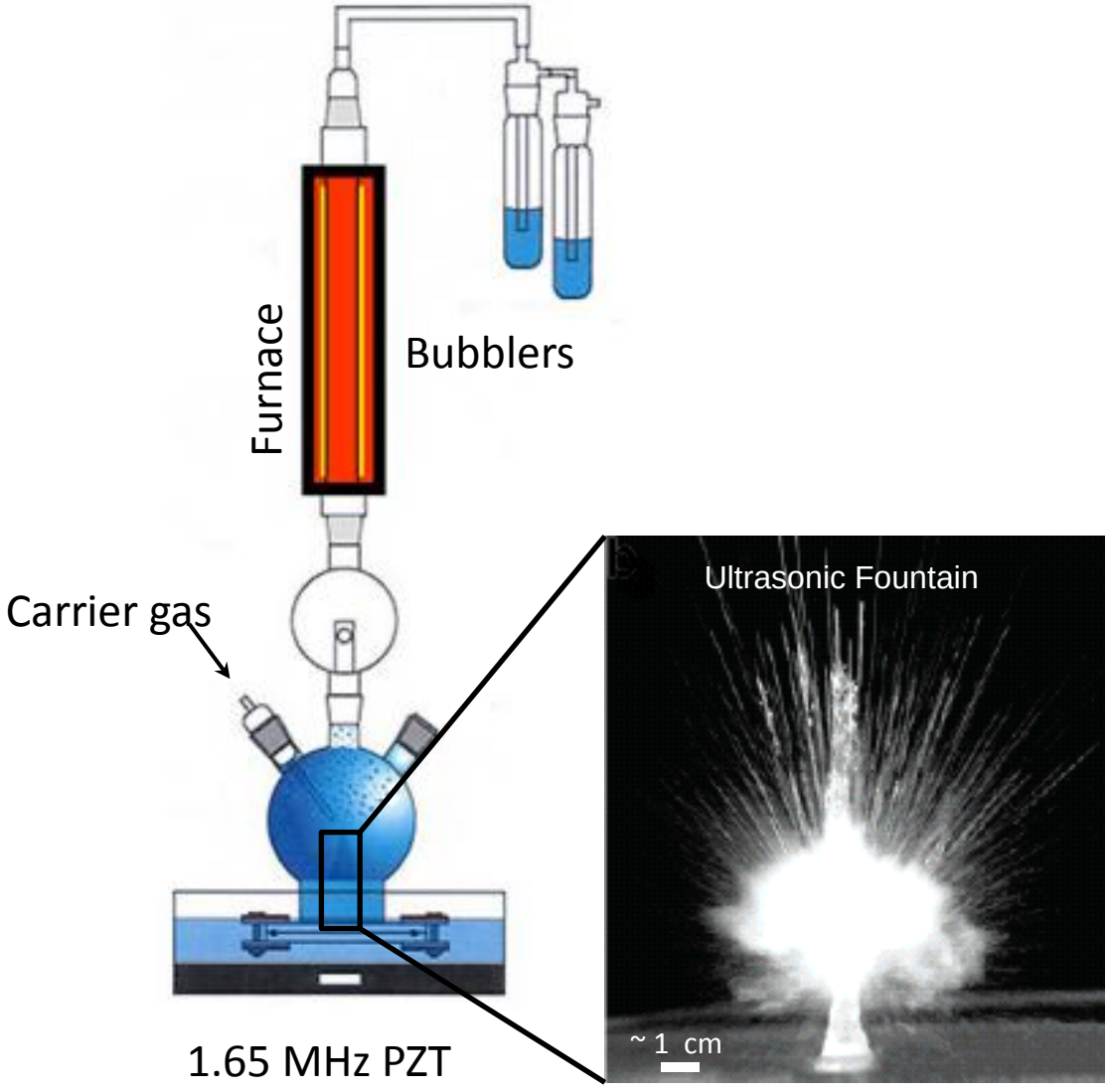

Figure 3.4 Ultrasonic spray pyrolysis setup with inset of an ultrasonic fountain.[13]

USP is a low cost, continuous flow method (**Figure 3.4**) that is easily scalable, and has been used to successfully synthesize porous carbon, quantum dots, and metal oxides among other materials.[14-22] A piezoelectric transducer (PZT) generates an ultrasonic fountain that forms aerosol microdroplets of precursor solution. The aerosol is then carried by gas flow through a furnace tube, where the precursor reacts. Then, the product is collected in a series of bubblers. This method is advantageous as it is a one-pot synthesis and the size and composition of the product is easily adjusted by altering the identity and concentration of the reactants.

In 1962, Lang[23] equated the droplet size generated by an ultrasonic mist as follows:

$$D_d = 0.34\left(\frac{8\pi\gamma}{\rho f^2}\right)^{1/3}$$

Where D_d is the droplet diameter, γ is the surface tension of the liquid being nebulized, ρ is the density of the liquid, and f is the frequency of the ultrasonic vibrations. Using water as the liquid, and 1.65 MHz as the frequency (which is the same frequency as used in this thesis): the average droplet diameter is approximately 3 μm, with most ultrasonically generated aerosols being between 3-5 μm.

Since the droplets must undergo evaporation, curing, annealing, etc. depending on the precursor, the final particle diameter can be calculated[24] by the following equation:

$$D_p = \left(\frac{MD_d{}^3C}{1000\rho_p}\right)^{1/3}$$

Where D_p is the particle diameter, M is the molecular mass of the precursor in solution, C is the molarity of the precursor in solution and ρ_p is the density of the precursor. The implication here is that particle size can be controlled by adjusting the precursor concentration.

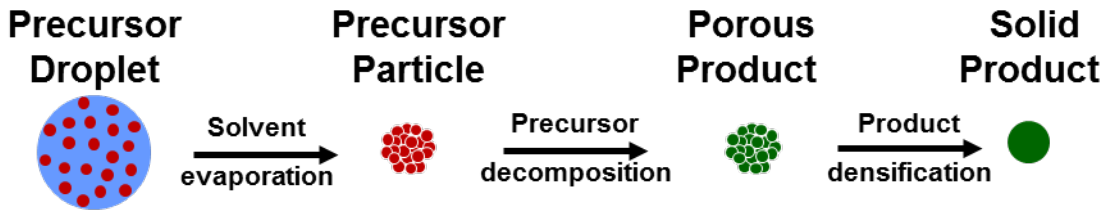

Figure 3.5 Schematic of an aerosol droplet undergoing a typical USP reaction.

The figure above describes a reaction taking place in the furnace tube of a USP cell. A droplet containing a precursor dissolved in solution undergoes solvent evaporation, and subsequent decomposition of the precursor (e.g., loss of water, CO_2). The removal of gaseous byproduct initially gives a porous material, which may undergo further densification. The Suslick group has made extensive use of ultrasonic spray pyrolysis; the figure below shows exemplary microspheres produced by this technique.[25-28]

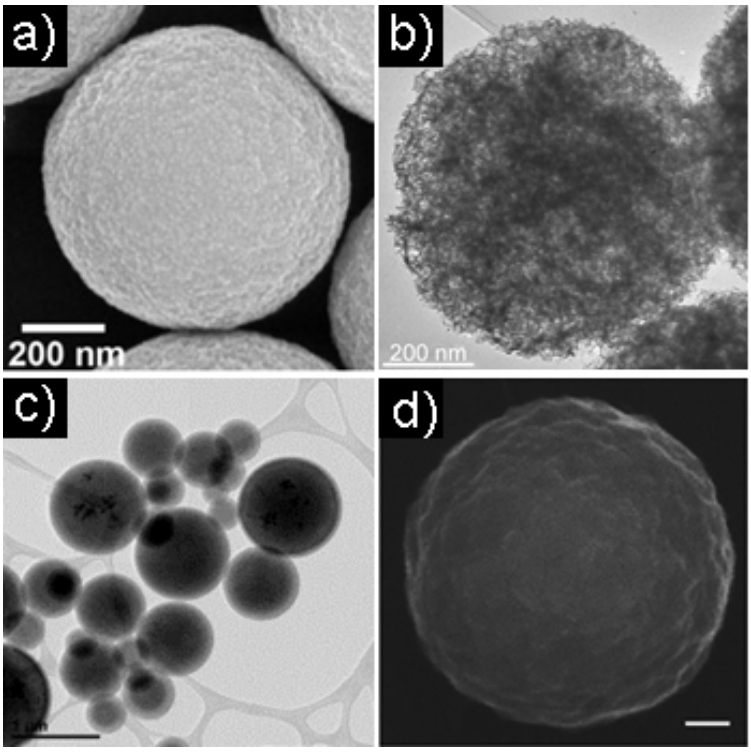

Figure 3.6 (a) SEM of titania microspheres, (b) TEM of porous MoS_2 microspheres, TEM of iron oxide microspheres (c), and (d) SEM of poly(ethylene-dioxythiophene) microspheres.

3.2 Experimental

3.2.1 Ultrasonic Spray Pyrolysis Apparatus

All the syntheses described in this chapter use the vertical setup shown in **Figure 3.6**. All of the glassware, excluding the furnace tube, was fabricated by the University of Illinois School of Chemical Sciences Glass Shop. The nebulizer consists of an electronic board (APC International, Inc., #50-1011) that has a piezoelectric transducer operating at 1.65 MHz (**Figure 3.7**). This generates approximately 2 μm droplets for water. The wave intensity of the transducer is controlled by a variable AC transformer (variac). The maximum intensity of the nebulizer was used for all work. As seen in the corresponding figure, the board/transducer sits at the base of what is essentially a household humidifier. Above the base is a water bath, which is in direct contact with the nebulizer. The water level sensor is a small buoy that acts as a killswitch in case the water level is below the cutoff for safe use; this is ~ 1L for the apparatus used in the following experiments. The four alignment pegs ensure that nebulization cell is positioned directly above the center of the nebulizer.

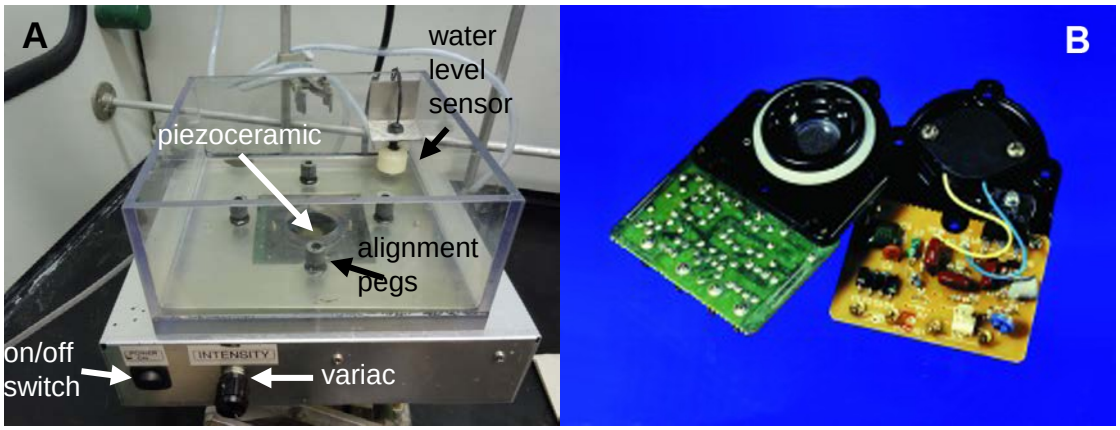

Figure 3.7 Photographs of (A) the home-built nebulizer and (B) the front and back of the piezoceramic nebulizer board. Image adapted from http://www.americanpiezo.com/products_services/nebulizers.html.

The nebulization cell is a custom-made 1L 3-neck round bottom flask. The bottom is fitted with a 57 mm flange with grooves for use with a Teflon O-ring. All neck types and dimensions are 24/40 ground glass joints. In order to separate the water bath from the nebulization cell, a 2 mil polyethylene or polytetrafluoroethylene film was used a membrane. This membrane was fixed in place between the O-ring and a custom clamp fabricated by the School of Chemical Sciences Machine Shop. The clamp consists of the following parts assembled in the following order: a brass ring (9 cm outer diameter, 6 cm inner diameter, 2 mm thick) with six equally spaced holes (1/4 in diameter), a polytetrafluoroethylene (PTFE) ring of similar dimensions, a second PTFE ring (5.6 cm outer diameter, 2.8 cm inner diameter, 7 mm thick) with an O-ring groove (4 mm wide, 1.5 mm deep). The O-ring sits between the groove and the membrane, on top of which sits the flange of the nebulization cell (**Figure 3.9**). Two semi-circular PTFE rings and then two semi-circular brass rings (with the same dimensions as the first brass and PTFE rings) are positioned above the flange, their holes aligned with those of the rings on the bottom. The clamp is then fixed in place by six socket head cap screws (1/4 in outer diameter, 2 in in length) which are threaded through the six holes and secured with washers and nuts (**Figures 3.8** and **3.9**). The composite cell is placed into the water bath, and any air trapped between the separation membrane and the water bath is removed using a syringe. This reduces impedance mismatch between the nebulizer and the contents of the nebulization cell, which results in poor mist generation.

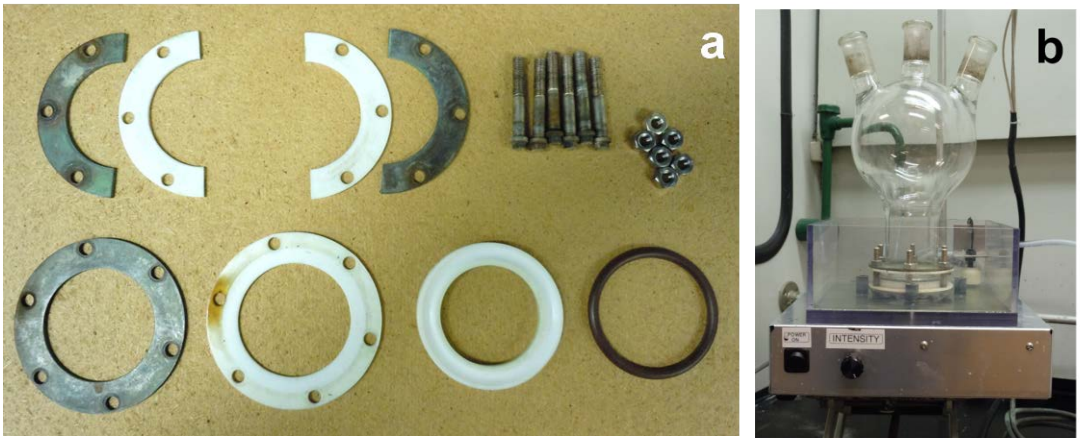

Figure 3.8 (a) Photograph of the custom nebulization cell clamp. (b) Photograph of the custom nebulization cell with clamp in the nebulizer base.

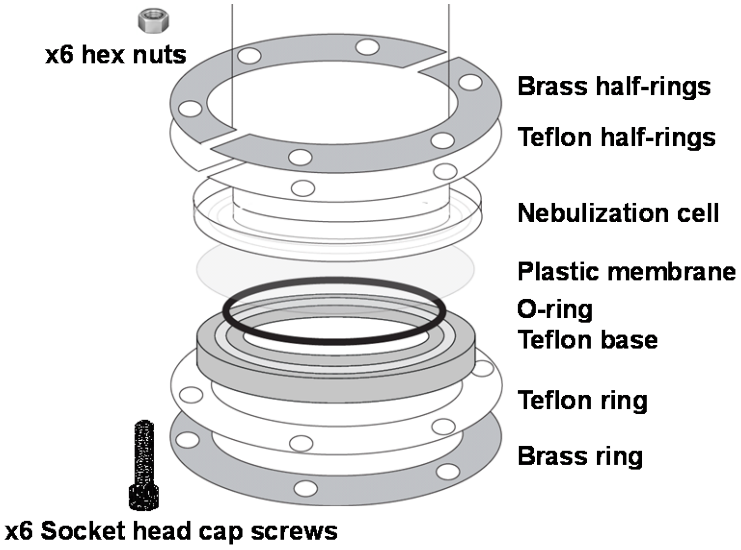

Figure 3.9 Diagram of clamp configuration, showing order of assembly.

A custom carrier gas inlet (**Figure 3.10**) is inserted into a side neck of the nebulization cell. The inlet has a male 24/40 ground glass hose connection joint with a stem that extends into the center of the nebulization cell (7 mm outer diameter, 5 mm inner diameter, ~3" in length). Since the center neck is connected the furnace tube, this ensures that the ultrasonic mist is carried by the gas efficiently. The hose connection is connected by Tygon tubing to the carrier gas. The flow rate of the gas is controlled by a rotameter. A rubber septum keeps the other side neck of

the nebulization cell airtight, allowing for precursor solution to be injected into the nebulization cell without introducing oxygen or moisture (for sensitive reactions).

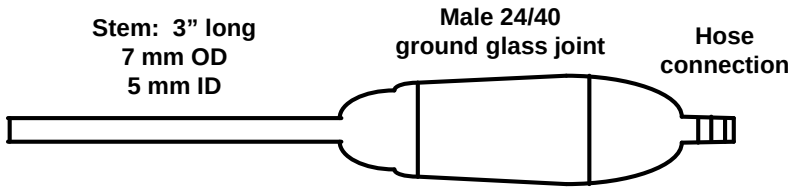

Figure 3.10 Schematic of the custom carrier gas inlet.

A standard rotary evaporator trap with a 24/40 ground glass joint is connected to the center neck of the nebulization cell to condense larger droplets before they enter the furnace tube; this is to ensure a narrower particle size distribution. Secondly, it prevents splashes of liquid alongside the ultrasonic fountain from touching the inside of the hot furnace tube and accumulating.

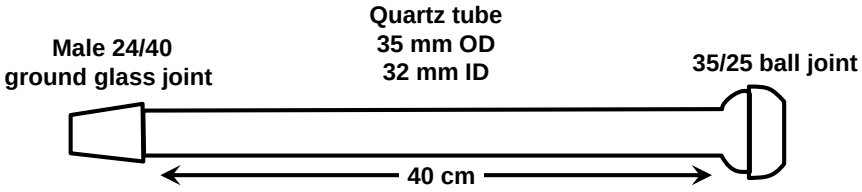

Figure 3.11 Schematic of the quartz furnace tube.

A quartz furnace tube (35 mm outer diameter, 32 mm inner diameter ~40 cm long, made by Quartz Scientific, Inc., **Figure 3.11**) with a 24/40 male ground glass joint at one end and a 35/25 ground glass ball joint at the top is housed in the furnace (Omega CRFC-212/120-C-A, **Figure 3.12**) and connected to the bump trap via the 24/40 joint. The furnace is controlled by a variable AC transformer and is rated for temperatures up to 980 °C. The temperature is monitored by a K-type thermocouple inserted between the furnace and the furnace tube. The tip

of the thermocouple is approximately one-third of the way down the tube (determined to be the hottest portion of the vertically oriented furnace).

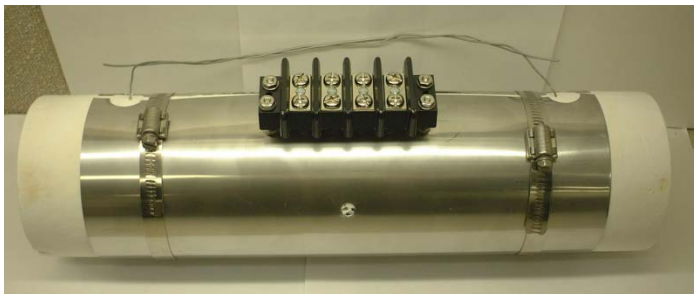

Figure 3.12 Cylindrical furnace for ultrasonic spray pyrolysis. Note that the picture is horizontally oriented. For syntheses, furnace was vertical. Photo Credit: Wong Suh.

A glass hose adapter (**Figure 3.13**, left) with a 35/25 ground glass socket joint on one end and a hose connection on the other sits atop the furnace tube and is held in place with a c-clamp (**Figure 3.13,** center). Tygon tubing (5/16 in inner diameter, 7/16 in outer diameter) connects this adapter to a series of bubblers (Chemglass #CG-4515, **Figure 3.13**, right) also connected to one another by Tygon. The bubblers are used for product collection, with each bubbler approximately half-filled with collection solvent.

Figure 3.13 Left: Glass adapter for furnace tube, center: c-clamp to fasten adapter to furnace tube and right: collection bubbler.

3.2.2 PDMS Microsphere Synthesis

Sylgard 184 polydimethylsiloxane (PDMS) precursor was purchased from Dow Corning as a two-part kit. PDMS microsphere precursor solutions contained the PDMS precursor in a 2:1 base:accelerator ratio. Colloidal Fe3O4 nanoparticles (~10 nm) were purchased as a stable suspension under the trade name Magna View Fluid from United Nuclear. The fluid consisted of 5% magnetite, 10% surfactant (oleic acid), and 85% oil carrier by volume. Polydiphenylco-polydimethylsiloxane microspheres were synthesized using a precursor solution containing 1.9 v/v % 15-17% diphenylsiloxane-dimethylsiloxane copolymer vinyl terminated (PDV- 1625, Gelest Inc.), 0.07 v/v% 25-35% methylhydrosiloxane-dimethylsiloxane copolymer (HMS-301, Gelest Inc.), 0.02 v/v% platinum-divinyltetramethyl-disiloxane complex in xylene (SIP6831.2LC, Gelest Inc.) in hexanes. Polytrifluoropropyl-co-polydimethylsiloxane microspheres were synthesized using a precursor solution containing 1.4 v/v% 35-45% trifluoropropylsiloxane-dimethylsiloxane copolymer vinyl terminated (FMV-4035, Gelest Inc.), 0.7 v/v% HMS-301, 0.02 v/v% SIP6831.2LC in hexanes. Polydimethylsiloxane-copoly(propylene oxide-ethylene oxide) microspheres were synthesized using a precursor solution containing 1.4 v/v% 30 mole% non-silicone dimethylsiloxane-vinylmethylsiloxane-(propylene oxide-ethylene oxide) block copolymer (DBP-V102, Gelest Inc.), 0.7 v/v% HMS- 2 301, 0.02 v/v% SIP6831.2LC in toluene. Polyethylene glycol (Mw 600) and polystyrene (Mw: 35,000) were added to the precursor as liquid cores. All other reagents were purchased from Sigma Aldrich and used as received without further purification. As described previously, a 1.65 MHz piezoelectric transducer is used to nebulize a precursor solution (e.g., 20 mg/mL PDMS in hexanes) into a mist of micrometer-sized droplets. The aerosol is carried into and through a heated furnace tube via an inert argon stream at 0.4 slpm. The droplets act as micron-sized

reaction vessels; the hexanes solvent quickly evaporates and Sylgard 184 precursors, catalyzed by a Pt catalyst, cross-link in the heated furnace (300 °C). The polymerization of PDMS happens very quickly, as the residence time in the furnace is only ~60 seconds, and since each droplet acts as an individual reaction vessel, individual microspheres are produced. The cured PDMS microspheres are collected in ethanol bubblers; ethanol was chosen because it is miscible with hexane, dissolves the uncured PDMS precursors, and easily disperses the cured microspheres. Following collection, the ethanol/microsphere suspension was centrifuged at ~5000 rpm for 60 minutes until the microspheres formed a pellet in the bottom of the centrifuge tube, the ethanol supernatant was decanted, fresh ethanol (~40 mL) was added, and the microspheres were re-dispersed via sonication. This washing protocol was repeated three times; the washed microspheres were suspended in hexanes and stored.

3.2.3 Cell Culture

Sections 3.2.3.-5 were done in collaboration with Elissa Grzincic and Prof. Cathy Murphy. Metastatic human breast cancer cells of the MDA-MB-231 cell line (ATCC) were used for microsphere uptake and viability experiments. All live cell work was done in a sterile environment with sterile materials, and live cells were kept at 37°C and 5% CO2. Cells were cultured in phenol red-free high-glucose DMEM (Corning) with 1 mM sodium pyruvate (Corning), 10% fetal bovine serum (Gemini Bio-Products), 1% penicillin/streptomycin (Corning), 0.1 mM non-essential amino acids (Corning), and 2.5 μg/mL Fungizone (Gibco).

3.2.4 Microsphere Uptake

20,000 cells (in complete culture medium) were plated into the well of a 35 mm well glass-bottomed culture dish (MatTek Corporation). After incubation for 24 hours, the medium was replaced with 200 μL of the 1.5 mg/mL PDMS microsphere solution (in medium). These

samples were incubated for another 24 hours, before washing five times with PBS (phosphate buffered saline solution) to remove free microspheres. Samples were then prepared for imaging, with multiple PBS washes between steps. Cells were first fixed with pre-warmed 4% (in PBS) paraformaldehyde (Sigma) for 15 min. and permeabilized with 0.5% (in PBS) Triton X-100 (Sigma) for 10 min. They were then stained for F-actin with 1:100 fluorescein phalloidin (Molecular Probes, 1 h incubation) and for cell nuclei with 300 nM 4',6-diamidino- 2-phenylidole dihydrochloride (DAPI, Molecular Probes, 30 min. incubation). Nile Red labeled microsphere uptake was then imaged by confocal fluorescence microscopy using a Zeiss LSM 710 confocal microscope.

3.2.5 Cell Viability

20,000 cells (in complete culture medium) were plated into the well of 35 mm well glass bottomed culture dishes. Three separate cultures were made for each of the tested conditions. After 24 hours of incubation, the medium was replaced with 200 μL of the appropriate concentration of non-fluorescent PDMS microspheres (davg = 1.15 μm). After a second 24 hour incubation, cells were washed once with PBS and stained using a MarkerGeneTM Live:Dead/Cytotoxicity Assay Kit. The working solution (in PBS) contained 2 μM carboxyfluorescein diacetate for staining live cells and 4 μM propidium iodide for staining dead cells. Samples were imaged by fluorescence microscopy using a Zeiss Axio Observer Z1 inverted compound microscope. Five random spots in the cell layer were imaged for each sample.

3.2.6 Rhodamine 6G (R6G) Loading and Release

PDMS microspheres (1.25 mg/mL; davg = 1.15 μm) were suspended in a 10 mg/mL solution of R6G in $CHCl_3$. $CHCl_3$ was used as the loading solvent because the USP PDMS

microspheres form a stable suspension in $CHCl_3$, R6G is soluble in $CHCl_3$, and $CHCl_3$ swells PDMS.[29] The microsphere/R6G/$CHCl_3$ mixture was put on the rotisserie overnight. The loaded PDMS microspheres were isolated from the $CHCl_3$/R6G solution via centrifugation (3400 rpm, 2 hrs). The microspheres were washed three times with 10 mL cold water. Each washing consisted of adding the water to the centrifuge tube, inverting the tube several times, centrifuging at 3400 rpm for 30 minutes, and immediately removing the supernatant using a pipette. After the final washing, the spheres were suspended in 10 mL of phosphate buffered saline (PBS, Thermo Scientific, w/o calcium or magnesium) to a concentration of 0.85 mg loaded microspheres/mL. This suspension was put on the rotisserie and kept at 37 °C for the release experiments. At each time point (0 minutes, 30 minutes, 1 hour, 1.5 hrs, 3 hrs, 5hrs, 10 hrs, 25 hrs, 50 hrs, 75 hrs, and 100 hrs), 2.0 mL of the PBS solution was removed and analyzed with UV/VIS (Varian Cary 5G UV-VIS-NIR spectrophotometer); 2.0 mL of fresh PBS was added to the suspended microspheres immediately. To quantify the total R6G loaded into the PDMS microspheres, loaded microspheres were suspended in ethanol, the solution isolated, and the absorbance at 525 nm determined using UV/VIS.

3.2.7 Characterization

Generally, scanning electron micrographs were obtained on a JEOL 7000F instrument operating at 10 kV with a medium probe current and a working distance of 10 mm. Samples were prepared by freeze drying a suspension of PDMS microspheres in methylcyclohexane on a Si wafer. Samples were mounted to the holder via carbon tape and sputter coated with approximately 10 nm of Au/Pd prior to analysis to prevent surface charging. Size distribution analysis was performed using Image J software.

Infrared spectroscopic data was collected using a Perkin Elmer Spectrum 100 FT-IR instrument using a diamond/ZnSe attenuated total reflection (ATR) accessory.

Raman was collected using a Nanophoton Raman-11 laser Raman microscope with a 532 nm laser. Samples were prepared by freeze-drying a suspension of PDMS microspheres in methylcyclohexane on a Si wafer.

Thermogravimetric analysis of the PDMS microspheres was obtained using a TA Instrument Q50 TGA. A 2.21 mg sample was heated from 20 °C to 300 °C at a rate of 20 °C/min and 300 °C to 750 °C at a rate of 10 °C/min under air (60 mL/min).

UV/VIS Diffuse Reflectance was done using a Prime-X™ back-thinned CCD array spectrometer (2.5 nm resolution), Deuterium (30 W)- Tungsten (5 W) light source, and fiber optic reflectance probe (Seven 400 μm illuminates and one 600 μm read fiber with a read diameter of 1 mm) was used to collect the UV/VIS diffuse reflectance measurements. Microspheres were analyzed using PVDF as a white background. Data was smoothed using a 20 point Savitzky-Golay smoothing filter and converted to a pseudo-absorbance using the Kubelka-Munk equation. Data from 485.35- 487.76 nm and 654.08-657.89 nm was removed prior to analysis; these regions show distortion due to hydrogen emission lines characteristic of the deuterium light source.

Fluorescence imaging was done using a Zeiss Axiovert 200M inverted research-grade microscope with a 41039 special yellow filter. Samples were prepared by drop-casting a suspension of the microspheres in hexane on a glass cover slip with immediate heating at 70 °C.

Energy dispersive spectrometry (EDS) line scans were obtained using a JEOL 7000F instrument equipped with a Thermo Electron EDS microanalysis system operating at 10 kV with

a high probe current and a working distance of 10 mm. Samples were prepared by freeze drying a suspension of PDMS microspheres in methylcyclohexane on Cu foil. Samples were mounted to the holder via carbon tape and sputter coated with approximately 10 nm of Au/Pd prior to analysis to prevent surface charging.

Transmission electron micrographs were obtained on a JEOL 2100 cryo microscope operating at 200 kV and equipped with a Gatan MatScan1kx1k progressive scan CCD camera. Samples were prepared by freeze-drying a suspension of PDMS microspheres in methylcyclohexane on a lacy formvar/carbon 200 mesh copper grid (Ted Pella, #01881-F).

3.3 Results and Discussion

3.3.1 Dow Sylgard 184 Microspheres via Ultrasonic Spray Pyrolysis

Ultrasonic spray pyrolysis (USP) is a simple and effective method for synthesizing micron-sized spherical particles because each nebulized droplet is its own micro-reactor. The size of the product can be tuned by changing the concentration of the reactant. The size of the droplet carrying the precursor can also be tuned by changing the frequency of the nebulizer, though this was not pursued in the following studies. We used the commercially available Dow Sylgard 184, which contains vinylmethylsiloxane-dimethylsiloxane copolymer and silica filler (toughening agent) as the base. The curing agent contains methylhydrosiloxane-dimethylsiloxane copolymer and a Pt catalyst. Dow Sylgard was designed to be cured at a variety of temperatures, inversely proportional to time. At room temperature, this takes 24 hours and at 100 °C, approximately 45 mins (according to manufacturer). Since the residence time of nebulized precursor in our USP setup is 30-60 seconds, even a five minute residence time would require an

impossibly slow flow rate. We therefore increased the reaction temperature to 300 °C, allowing for rapid solvent evaporation and curing. Rapid solvent removal is necessary because 2-part elastomers such as Sylgard do not cure in the presence of large amounts of solvent. We also used 5 times the recommended amount of curing agent, as initial experiments that used only the recommended amount gave little to no product. This modification almost certainly affects the crosslinking ratio and thus the swellability of our microspheres, but comes with the benefit of increasing the yield substantially.

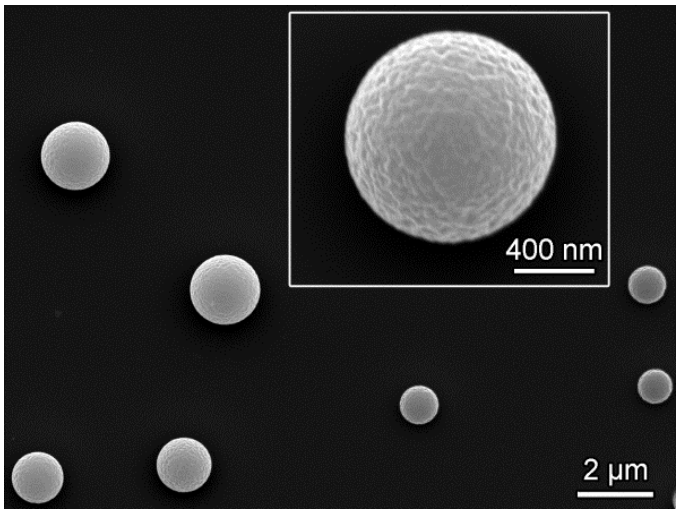

Figure 3.14 SEM of Dow Sylgard Microspheres, inset shows finer detail.

The SEM (**Figure 3.14)** indicates that the USP products are spherical particles with very little agglomeration or malformation. The IR spectrum contains all of the characteristic peaks associated with PDMS. Prominent peaks include aliphatic C-H stretches at 2963 cm^{-1}, Si-O-Si modes at 1100 and 1075 cm^{-1} and Si-CH_3 stretches at 790 and 1260 cm^{-1}. Raman also confirms the C-H stretches consistent with PDMS. Slight offsetting of the colorization in **Figure 3.15** occurs due to the spherical topography of the microspheres.

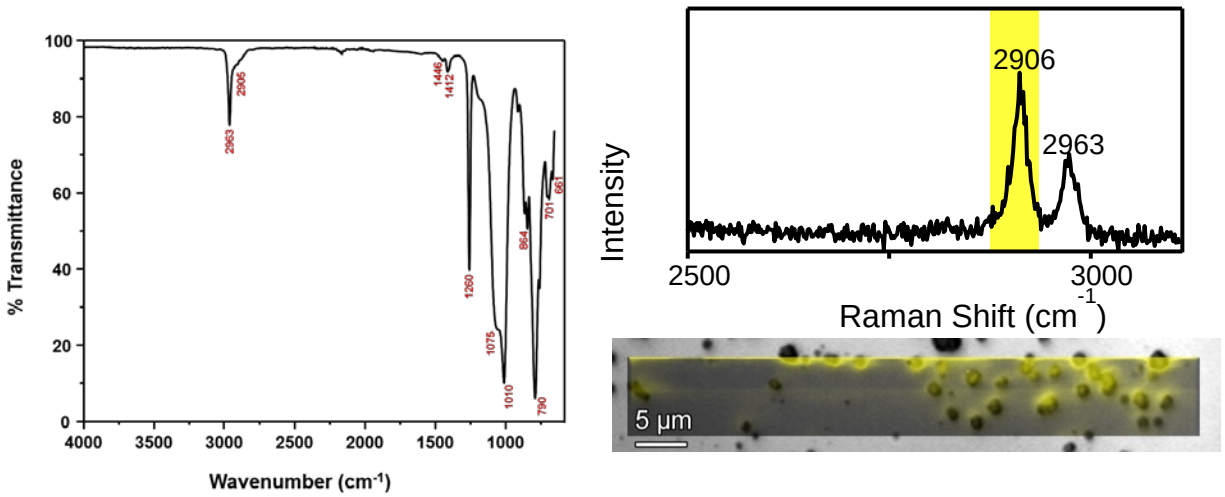

Figure 3.15 a) ATR-FTIR spectrum of resulting product; peaks match literature values for PDMS. [5, 30] b) Raman spectrum of product, C-H stretching peaks[31] (2906 and 2963 cm^{-1}) for PDMS are clearly evident. c) Optical image of PDMS microspheres overlaid with Raman mapping showing the relative intensity of the C-H stretching peak (2906 cm^{-1}, highlighted in (b)) as the intensity of yellow coloration.

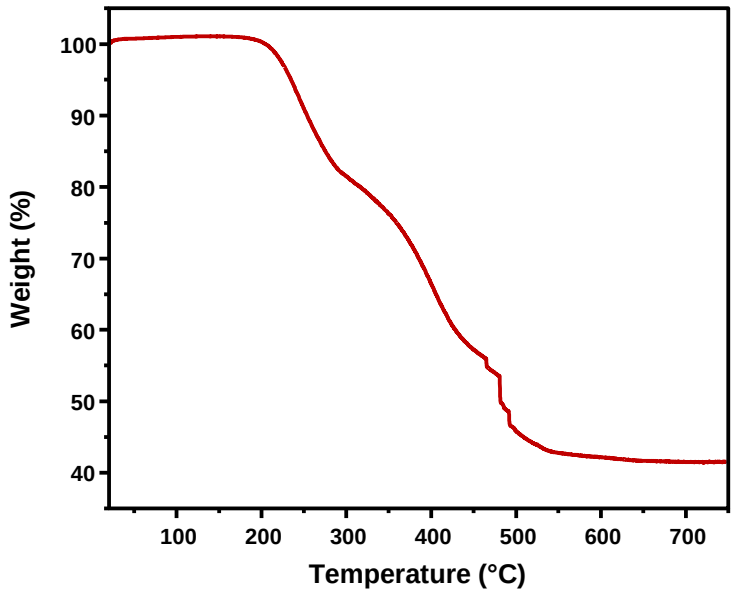

Figure 3.16 Thermogravimetric analysis of polydimethylsiloxane microspheres.

Thermogravimetric analysis (**Figure 3.16**) shows large mass loss beginning at 200 °C. This is attributable to volatilization of cyclosiloxanes, and the possible removal of uncured polymer remnants.[32, 33] Dow Corning notes that both base and curing agent contain volatile

organic compounds; it is possible a small amount of these may linger after curing and washing. At above 350 °C, PDMS begins to depolymerize and will form various combustion products in the presence of air, including CO_2, silica and silicon carbide. No notable decomposition occurred after 500 °C.

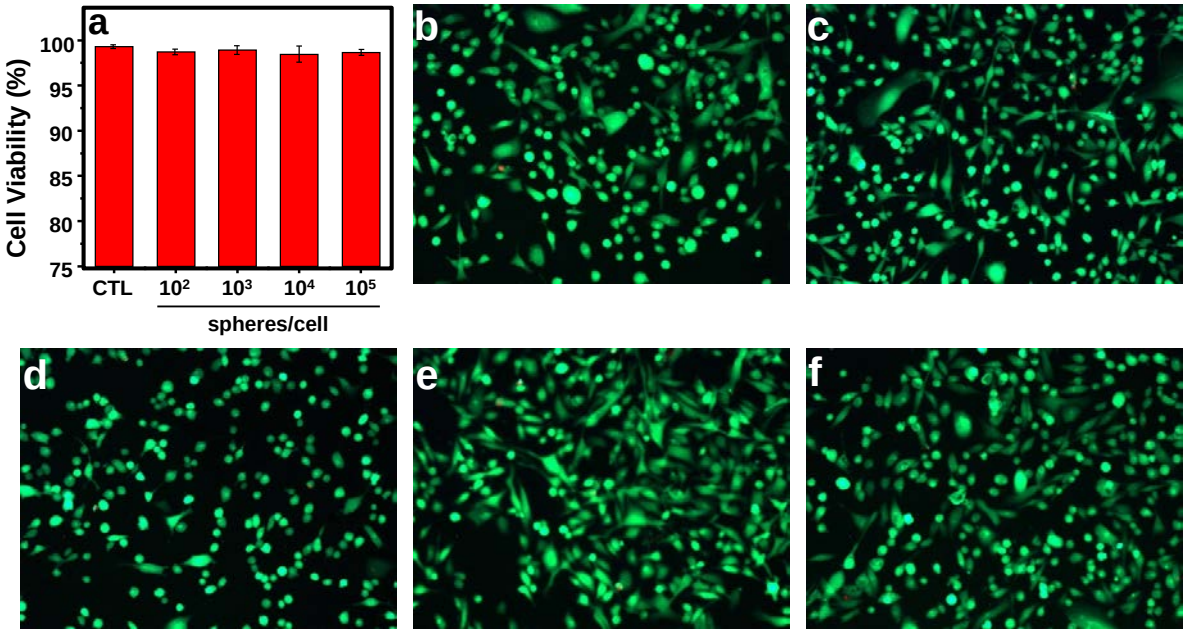

Figure 3.17 Polydimethylsiloxane (PDMS) microsphere (prepared by USP) cytotoxicity. (a) Cytotoxicity study; no statistically significant differences in cell viability are seen among the control and concentrations of PDMS microspheres ranging from 100 to 100,000 spheres/cell. (b-f) Representative fluorescence images of stained cells from polydimethylsiloxane microsphere viability experiments. (b) Control. (c) 100 spheres/cell. (d) 1000 spheres/cell. (e) 10,000 spheres/cell. (f) 100,000 spheres/cell. Cells that are stained green are alive, cells that are stained red are dead.

In order to demonstrate the biocompatibility of our microspheres (relevant to potential medical applications), we incubated them at various concentrations with human breast cancer cells. There was no statistical difference in viability between a control sample and cells incubated at a 10^5:1 ratio of microsphere:cell for 24 hours. Cell viability was 99% in cases,

indicating that these PDMS microspheres are effectively bio-inert. **Figure 3.17** shows fluorescence images of live/dead stained cells (live cells are green and dead cells are red).

The size of these PDMS microspheres can be tuned by changing the concentration of the precursor. **Figure 3.18-19** show the variation in particle size as a function of concentration, which was varied by a factor of 100. At the lower end of 1 mg PDMS per mL of solvent, the average particle size was 500 nm, with spheres as small as 100 nm being produced. By increasing the concentration to 4 mg/mL solvent, the average size increases to 890 nm. At 20 mg/mL, the average size is 1.15 μm and at 100 mg/mL the average size is 1.96 μm. The minimum concentration usable by the USP process is limited by yield, and perhaps also by the surface tension of the resultant product. The maximum concentration is limited by viscosity; reactions attempted at concentrations higher than 100 mg/mL were too viscous to nebulize.

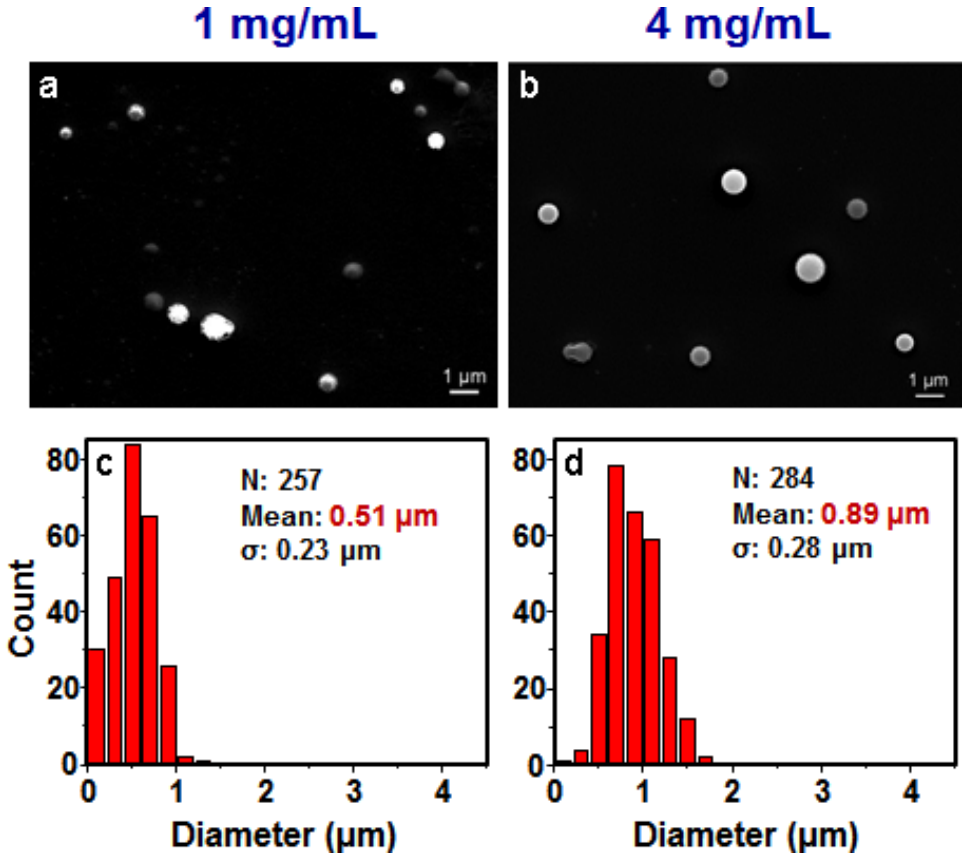

Figure 3.18 Size control of polydimethylsiloxane (PDMS) microspheres. a,b) SEMs of PDMS microspheres obtained with a) 1 mg mL^{-1}, and b) 4 mg mL^{-1}, PDMS in hexanes. c,d) Size distributions of microspheres shown in (a,b), respectively. Size distributions were determined using the Image J software package, with total number of microspheres counted given as N.

Interestingly, the values we obtained for particle diameter do not quantitatiely follow the cube root of concentration as is predicted by the equation. Possible reasons for this could be polydispersity in the precursor material itself. We estimate the average molecular weight of the precursor to be 50,000 g/mol, but there may be large variations in that value. Secondly, Dow Sylgard 184 contains silica filler, the amount of which certainly would affect the final product. Finally, the monodispersity of the aerosol cannot be taken for granted; our only safeguard against unusually large droplets entering the furnace tube is a rotary evaporator trap.

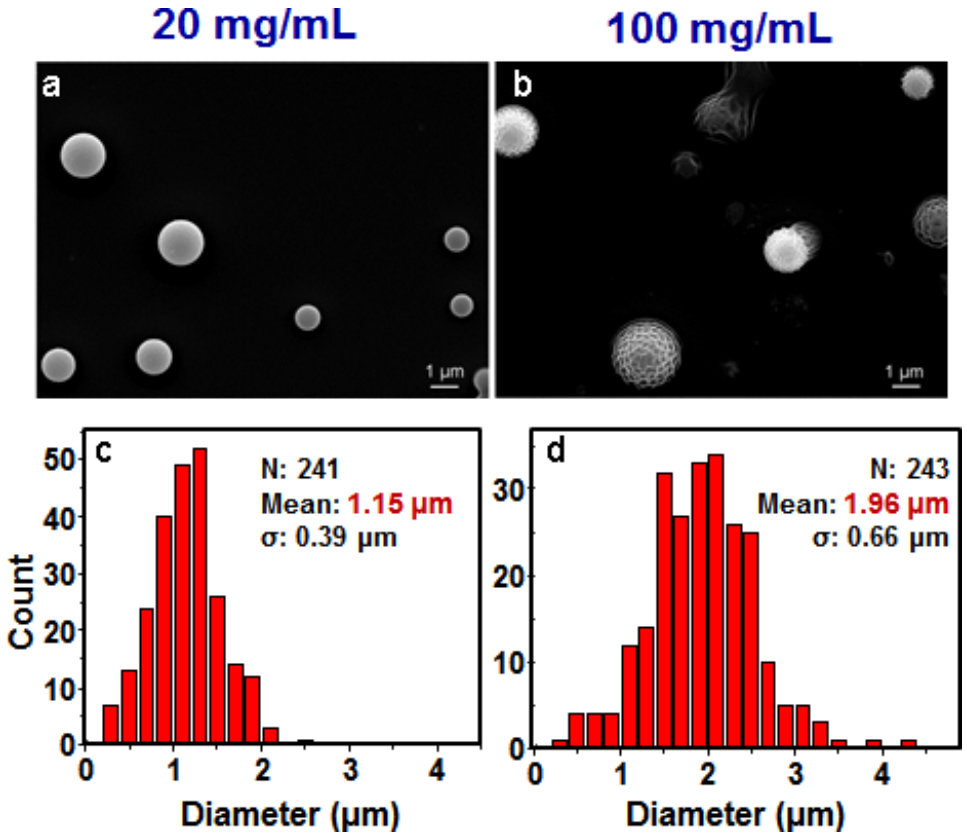

Figure 3.19 Size control of polydimethylsiloxane (PDMS) microspheres. a,b) SEMs of PDMS microspheres obtained with a) 20 mg mL^{-1}, and b) 100 mg mL^{-1}, PDMS in hexanes. c,d) Size distributions of microspheres shown in (a,b), respectively. Size distributions were determined using the Image J software package, with total number of microspheres counted given as N.

3.3.2 Copolymeric Silicone Microspheres via Ultrasonic Spray Pyrolysis

Our USP synthesis is not limited solely to Dow Sylgard, but a variety of copolymeric silicones also work. In order to demonstrate this, we chose the following silicone copolymers listed in **Table 3.1**. Since these formulations contain no silica filler, and have a known mole-ratio of their respective constituents, we have the ability to very precisely adjust the properties of the resultant product.

Table 3.1 Co-polymeric microsphere precursors, properties and mole percent

Co-Polymer	Properties of co-polymer[34]	Mole percent co-polymer
Polydiphenyl-co-dimethylsiloxane	Improved low-temperature stability, higher refractive index relative to PDMS	15-17
Polytrifluoropropyl-co-dimethylsiloxane	Lower hydrocarbon solubility, lower refractive index relative to PDMS	25-35
Polydimethylsiloxane-co-poly(propylene oxide-ethylene oxide)	More polar/hydrophilic than PDMS, greater compatibility with thermoplastics	30

As demonstrated by **Figure 3.20**, USP is capable of producing a variety of silicone microspheres. Several other copolymeric Pt-catalyzed silicones exist. We believe that they can be used in the precursor, regardless of substituent, so long as the appropriate solvents and appropriate ratio of the precursors are used. Peaks in **3.20a** corresponding to the polydiphenylsiloxane chains are labeled; defining peaks include sharp bands at 1600 and 1430 cm^{-1} and a set of three bands in the fingerprint region at ~ 740, 720 and 700 cm^{-1} that have increasing band intensity with decreasing wavenumber.[35] Characteristic polytrifluoropropylsiloxane peaks in **3.10**c include a peak at 1210, 1070, and 900 cm^{-1}.[35] Peaks in **3.20e** corresponding to the poly(propylene oxide-ethylene oxide) regions are labeled; the stretches at 2870, 1375, and the shoulder at 1350 cm^{-1} can be attributed to, respectively, a CH_3 stretching mode, the symmetrical bending vibration of the methyl group, and the wagging vibration of the methylene group of the poly(propylene oxide-ethylene oxide) chains.[36] The FTIR spectra (**Figure 3.20**a, c, e**)** show all characteristic peaks expected for polydimethylsiloxane.

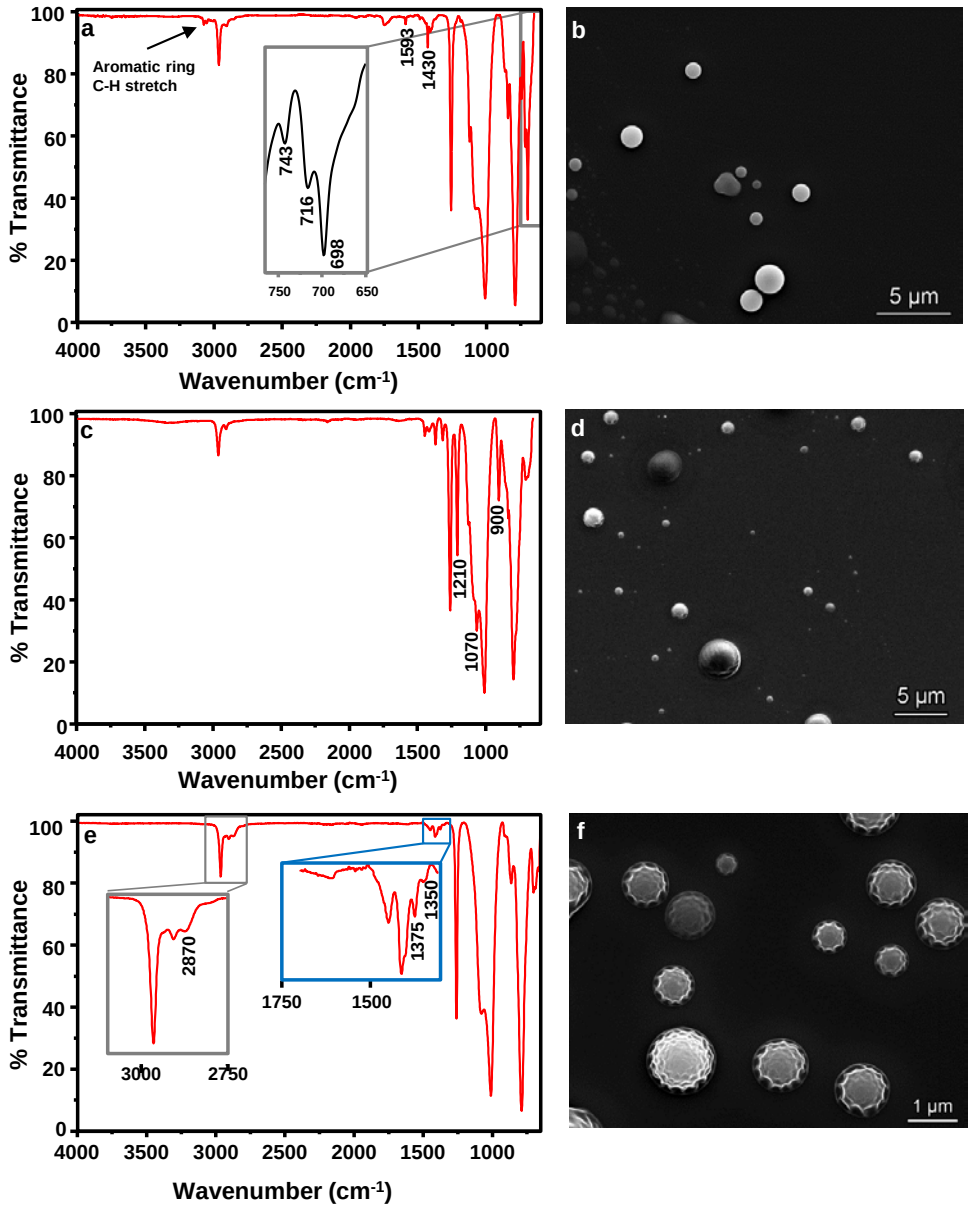

Figure 3.20 Copolymeric silicone microspheres fabricated using ultrasonic spray pyrolysis. **(a & b)** ATR-FTIR and SEM, respectively, of polydiphenyl-co-polydimethylsiloxane microspheres. **(c & d)** ATR-FTIR and SEM, respectively, of polytrifluoropropyl-co-polydimethylsiloxane microspheres. **(e & f)** ATR-FTIR and SEM, respectively, of polydimethylsiloxane-co-poly(propylene oxide-ethylene oxide) microspheres. Note that the scale bar for **(f)** is different from that of **(b)** and **(d)**.

3.3.3 Magnetic Microspheres via Ultrasonic Spray Pyrolysis

Magnetic polymer-encapsulated microspheres have been proposed for use in applications such as MRI contrast, magnetic hyperthermia, and magnetic cell separation and as targeted drug delivery agents. By simply adding a commercial ferrofluid to the precursor used to make the microspheres in 3.3.1, we synthesized magnetic silicone microspheres (**Figure 3.21**). The ferrofluid is a colloidal suspension of superparamagnetic iron oxide nanoparticles (SPIONs). SPIONs are an ideal choice for the applications listed above as they have no remnant magnetization in the absence of a strong magnetic field. This reduces the risk of agglomeration in blood vessels.

As dispersed in solution, the microspheres are light brown in color and can be easily moved by a magnet. Interestingly, the product takes on a core-shell morphology (**Fig 3.21**b), confirmed by TEM and EDX (**Figure 3.21c** and e), which can be explained by phase separation. The PDMS and the ferrofluid are immiscible, but because the PDMS has the lowest surface energy of all the precursor components, it will preferentially wet the ferrofluid and form the shell. A schematic of core-shell formation is shown in **Figure 3.22.**

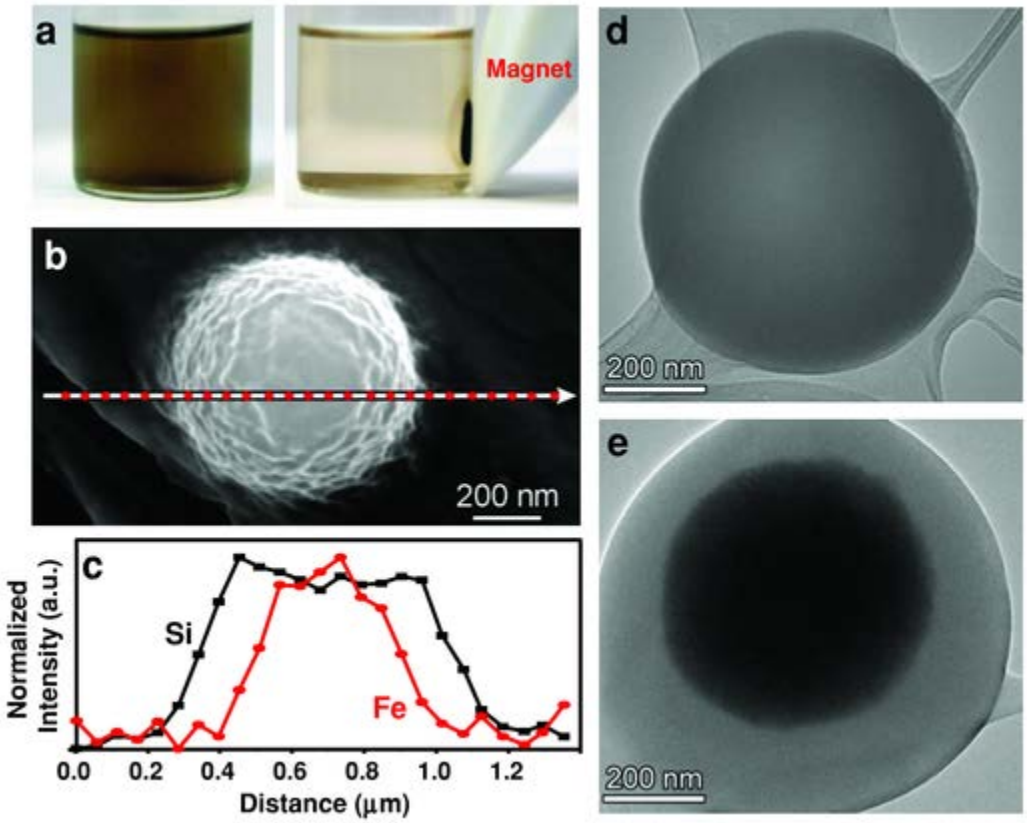

Figure 3.21 Magnetic core-shell polydimethylsiloxane (PDMS) microspheres prepared using ultrasonic spray pyrolysis. a) Image of magnetic PDMS microspheres showing (left) microspheres dispersed in hexanes and (right) microspheres pulled from solution using a magnet. b) SEM of magnetic PDMS microsphere on copper foil showing path of energy-dispersive X-ray spectral (EDS) line scan. c) EDS line scan showing Si and Fe concentrations along the path line shown in (b). d) TEM of PDMS microsphere (prepared without Fe_3O_4) showing uniform density and composition throughout the sphere. e) TEM of magnetic microsphere showing core-shell structure.

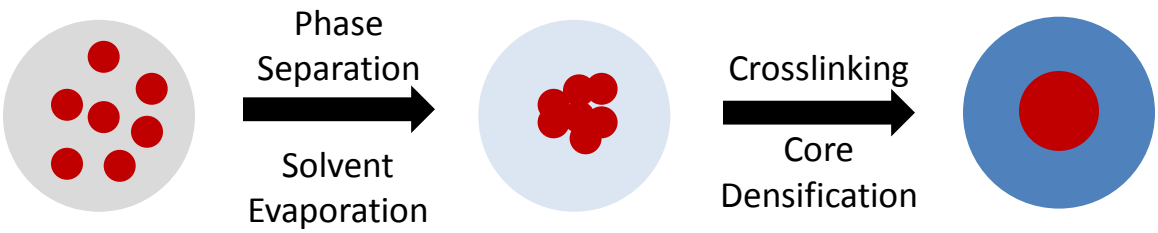

Figure 3.22 Schematic of core-shell formation. Iron oxide nanoparticles (red) move to the core to maximize favorable interactions, while PDMS (gray: dissolved in solvent, light blue: uncured, dark blue: cured) does the opposite, curing as a shell.

While the schematic above uses the example of a single-core particle, we observed that as many as 25% of our magnetic microspheres had multiple cores (**Figure 3.23**.) It is possible that smaller single core-shell particles merged during the solvent evaporation process forming one larger multi-core shell structure. Though we cannot exclusively make single-core or multi-core particles using the USP method, we were able to exercise a great degree of control over the size of the average core. By simply changing the ratio of PDMS:Ferrofluid from 1:1 v/v to 3:1 v/v, the average size of the core shrank from 800 nm to about 400 nm. The average diameter of the particle on the other hand, showed a modest decrease as the iron content increased (**Figure 3.24**). The thickness of the PDMS shell is important depending on the application: for drug delivery, thicker shells would be able to carry a larger dose of the active pharmaceutical. For hyperthermia, very thin shells would be favorable since PDMS is insulating and heat transfer would be reduced.

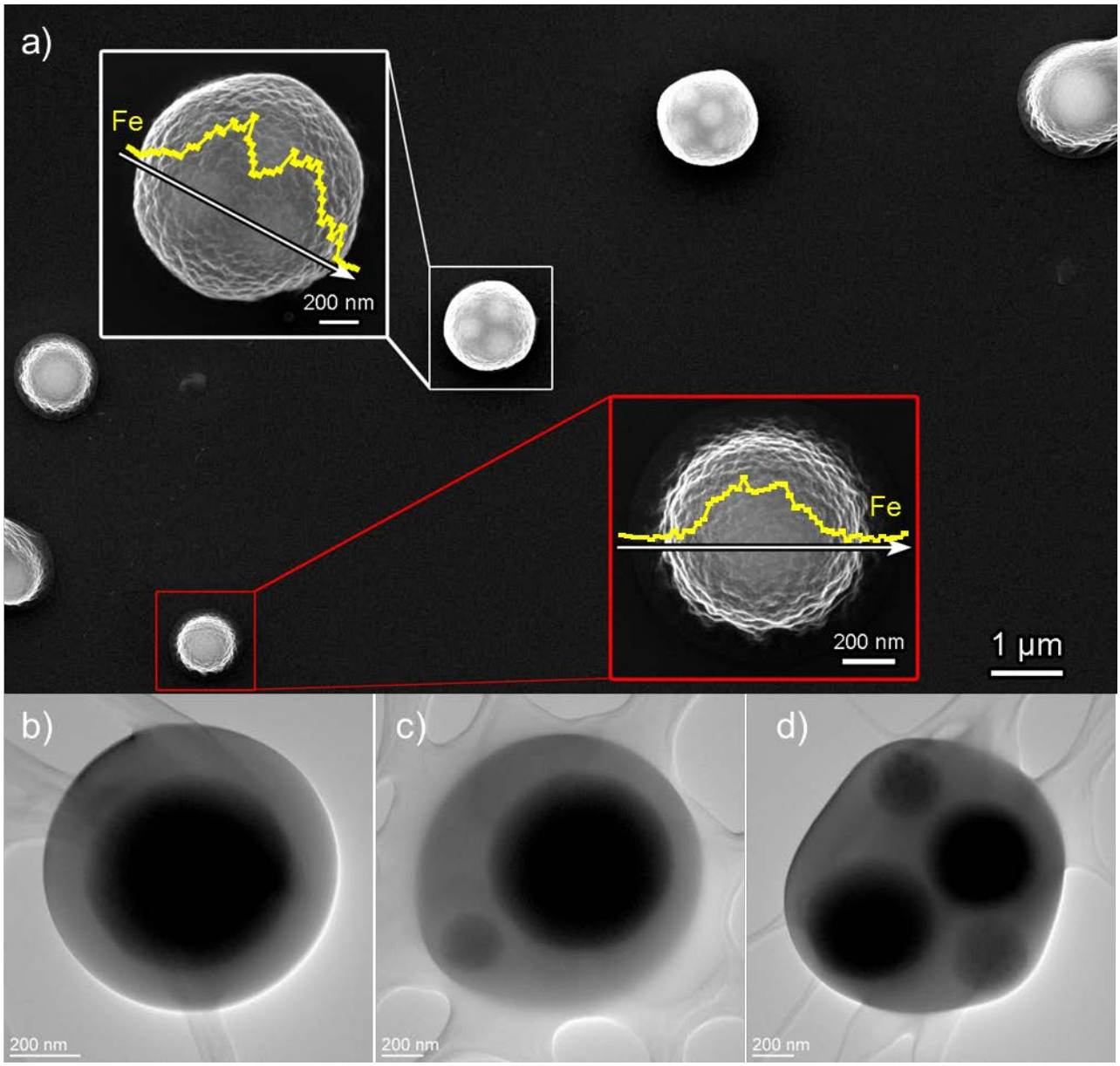

Figure 3.23 (a) Scanning electron micrograph of magnetic polydimethylsiloxane microspheres (accelerating voltage of 20 kV). Insets show expanded view of individual microspheres with EDS trace for iron shown in yellow. (b-d) Transmission electron micrographs of magnetic PDMS microspheres showing one, two, and many iron cores.

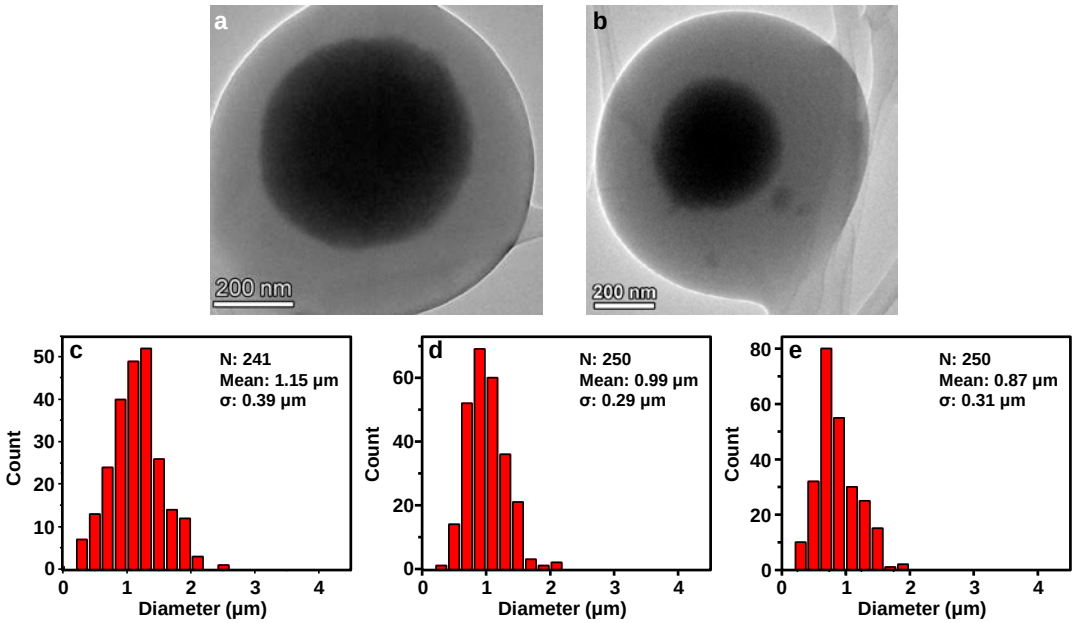

Figure 3.24 (a, b) Transmission electron micrographs of a magnetic polydimethylsiloxane (PDMS) microsphere obtained with (a) a precursor solution containing a 1:1 v/v ratio of PDMS (20 mg/mL hexane) to ferrofluid and (b) a precursor solution containing a 3:1 v/v ratio of PDMS (20 mg/mL hexane) to ferrofluid. (c-e) Size distribution of PDMS microspheres obtained with (c) a 20 mg/mL PDMS in hexane precursor solution, (d) a precursor solution containing a 1:1 v/v ratio of PDMS (20 mg/mL hexane) to ferrofluid, and (e) a precursor solution containing a 3:1 v/v ratio of PDMS (20 mg/mL hexane) to ferrofluid.

We were also able to produce composite magnetic silicone microspheres (**Figure 3.25**), with both the iron oxide and PDMS distributed throughout the particle as opposed to a core-shell structure. This was done by substituting dimethylsiloxane-vinylmethylsiloxane-(propylene oxide-ethylene oxide) block copolymer (DBP-V102, Gelest Inc.) in for Dow Sylgard. The DBP-V102 contains 30 mol% polypropylene oxide and polyethylene oxide (PPO-PEO), which is hydrophilic and has a higher surface energy. Thus, it is incapable of wetting the ferrofluid. SEM shows that dried microspheres tend to form grape-like clusters, presumably due to the favorable interactions of the hydrophilic PPO-PEO portions of the PDMS. EDS (**Figure 3.25 c-e**) confirms that both Si and Fe are evenly distributed throughout the clustered microspheres, and TEM (**Figure 3.25a**) shows no evidence of a core-shell structure. At higher magnifications, individual

SPIONs can be seen. A composite structure could be more useful than a core-shell structure in certain circumstances. For instance, MRI contrast is strongly dependent on proximity of local hydrogen atoms to the contrast agent. A shell would increase this distance, whereas a composite structure increases the number of possible interactions.

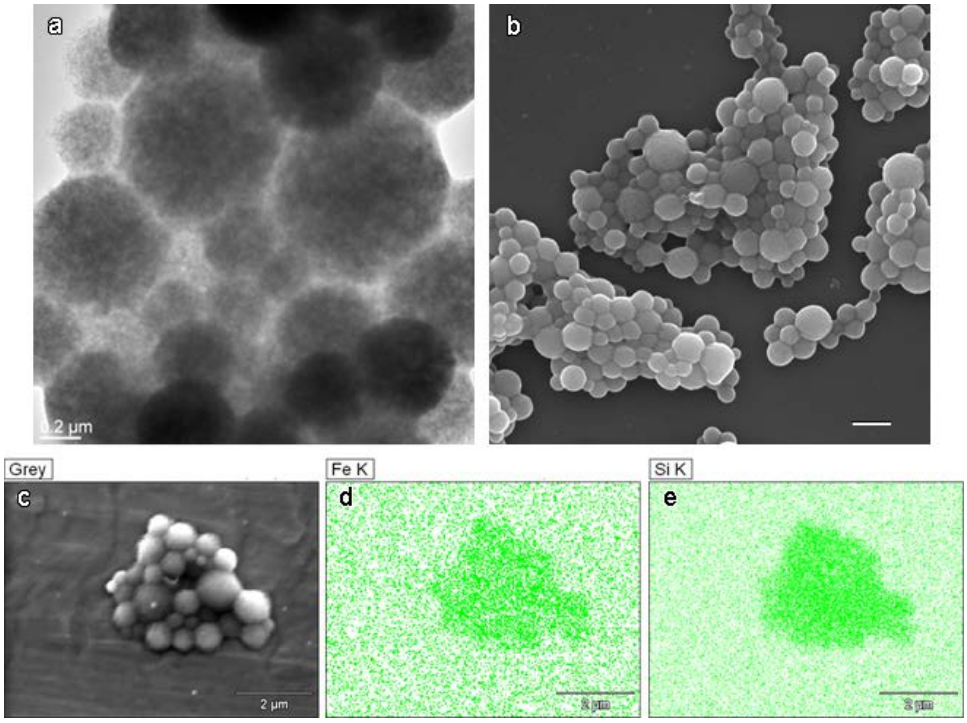

Figure 3.25 a) Transmission electron micrograph of a composite magnetic PDMS-co-PPO-PEO microsphere, showing no signs of core-shell structure. b) Scanning electron micrograph of the same particles, showing significant clustering. Scale bar is 1 µm. c) Grey EDS image of a cluster of composite magnetic microspheres. d) Fe color-mapping of the same particles and e) Si mapping of the same particles on a Cu sample grid. Both Fe and Si are dispersed throught the entirety of the microsphere cluster.

3.3.4 Liquid-Filled and Polystyrene Core Microspheres

Liquid-filled particles can be used to encapsulate a variety of interesting compounds such as fragrances and pharmaceuticals. In order to make liquid-filled silicone microspheres (**Figure 3.26**), we added liquid polyethylene glycol or solid polystyrene at a 1:1 ratio by volume to the

precursor using the synthesis described in 3.3.1. The product resembles the magnetic particles described in the beginning of 3.3.3 in that both single and multi-core products are formed.

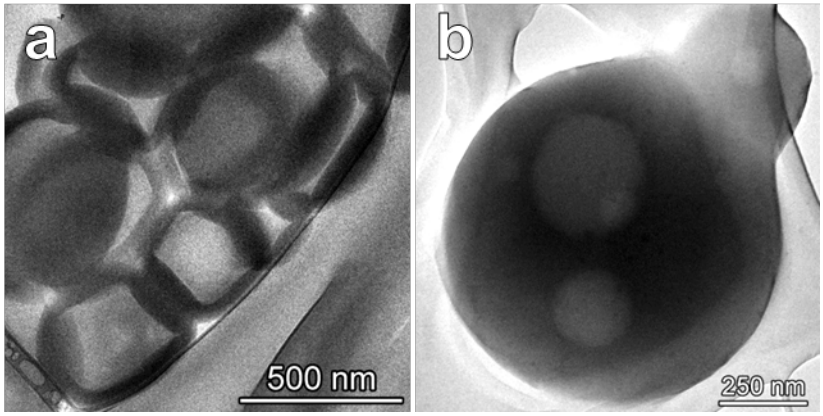

Figure 3.26 a) Liquid PEG-PDMS core-shell microspheres synthesized using USP from a precursor solution containing a 1:1 ratio of PDMS (Sylgard 184): PEG (MW = 900) 22 mg mL^{-1} in toluene. (b) PS-PDMS core-shell microspheres synthesized using USP from a precursor solution with a 5:1 ratio of PDMS (Gelest VDT-123):PS (MW = 35,000) 22 mg mL^{-1} in toluene.

The product in (a) is not completely spherical because PDMS is an elastomer and thus, can deform. In the presence of a liquid core, some of the liquid is removed during the washing protocol, thus the appearance of these microspheres is akin to a partially inflated basketball. Polystyrene is commonly used as a template that can be etched away by acetone, (for instance, in hollow silica particles). Thus, these microspheres could be made completely hollow. Applications of hollow microspheres were explored by former Suslick members Jackie Rankin and Samantha Fuchs. Experimental details, characterization and proposed applications of such microspheres can be found in Rankin's thesis.[37]

3.3.5 Fluorescent Silicone Microspheres

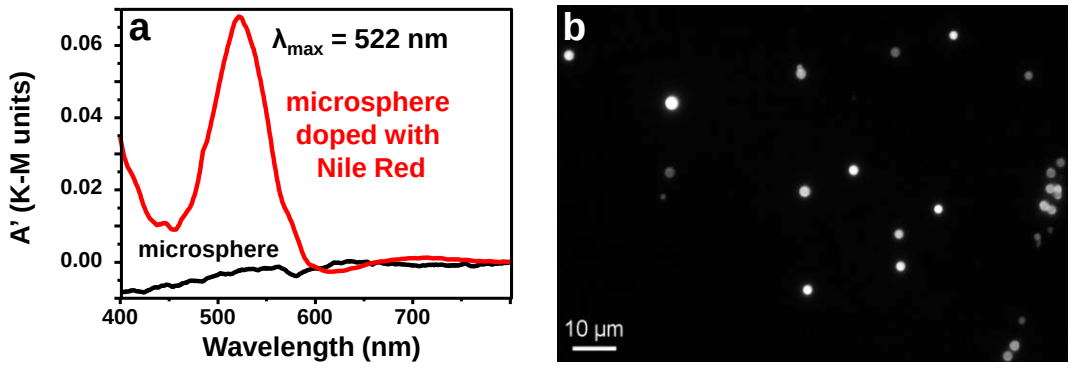

Figure 3.27 Fluorescent polydimethylsiloxane (PDMS) microspheres, cell uptake, and small molecule release. a) Diffuse reflectance spectrum of Nile red doped PDMS microspheres (red) and non-fluorescent PDMS microspheres (black). Peak at 522 nm indicates successful inclusion of Nile red. b) Fluorescence image of Nile red doped PDMS microspheres.

Fluorescent microparticles have found use in biological assays and for labelling specific cells of interest.[38] Problems often encountered with such materials range from photo-bleaching to short half-life in biological media.[39, 40] Thus, we produced fluorescent silicone microspheres and evaluated their ability to fluoresce in cells. There are two synthetic routes to fluorescent microspheres: 1) Adding a fluorescent dye to the precursor to ensure that it is suspended in the crosslinked matrix of the resultant microspheres, 2) dissolving the dye in an appropriate solvent and then adding silicone microspheres to the solution, causing the microspheres to uptake the dye. The second route may be necessary for heat-sensitive dyes that would otherwise decompose in the furnace, that would be difficult to acquire/manufacture or that would not appreciably dissolve in a solvent compatible with the PDMS precursor. In order to demonstrate the viability of route 1, we doped the microspheres synthesized in 3.3.1 with Nile Red, a common organic dye. As can be seen in **Figure 3.27**, the peak at 522 nm indicates that the Nile Red persists in the final product, even after washing the product with solvent several times. Even after prolonged

storage (~1 month) in solvents such as hexane or ethanol, these microspheres continued to show fluorescence peaks.

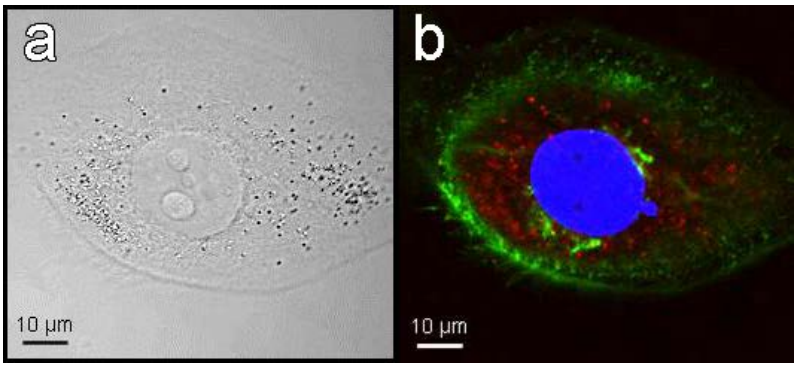

Figure 3.28 a) Bright field image of cell that has taken up Nile-red doped PDMS microspheres. b) Fluorescent image of cell in (a). The cell membrane has been stained green, the cell nucleus has been stained blue, and the Nile red doped microspheres appear red.

These fluorescent microspheres also have the potential to be used for cellular tracking. To this end, we incubated Nile Red doped silicone microspheres with human carcinoma cells for 24 hours in a phosphate-buffered saline (PBS) medium. The cells were then imaged and showed strong red fluorescence from the cytosol, indicating that the microspheres had successfully been taken up. The cells are localized to the cytosol (stained red in **Figure 3.28b**) and stay separate from the nucleus (stained blue in **Figure 3.28b**).

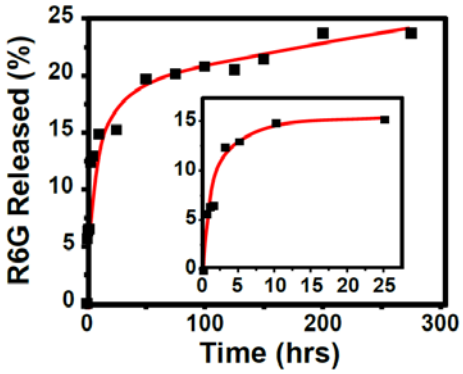

Figure 3.29 Release kinetics of Rhodamine 6G (R6G) from PDMS microspheres into phosphate buffered saline.

Route 2 opens up a different functionality for these microspheres. When we incorporated Rhodamine 6G, an organic dye, into Sylgard microspheres post-synthesis, it was found that the dye could be slowly released into a phosphate-buffered saline solution over time (**Figure 3.29**). This was done by calibrating the UV/VIS absorption of known concentrations of R6G and comparing the absorbance of the PBS-microsphere solution over time. Rhodamine 6G is a small hydrophobic molecule that has a very similar partition coefficient to many important drugs.[41, 42] Thus, we believe that the PDMS microspheres described here could be used for slow release of active pharmaceutical agents, especially those that are highly sensitive or expensive. These results are very preliminary, as only ~25% of the total R6G was released over 2 weeks. It is likely that high siloxane crosslinking ratios and the hydrophobic nature of the PDMS polymer may have caused the microspheres to retain a majority of the R6G.

3.4 Conclusions

We have developed a simple and scalable route for mass production of a variety of PDMS microspheres. The composition, functionality and size can be easily tuned by modifying the precursors. The ultrasonic spray synthesis produces microspheres with diameters ranging from <500 nm to ~2 μm with a relatively narrow size distribution. These microspheres are easily taken into the cell cytosol and have extremely low cytotoxicity even at a concentration of 100,000 spheres/cell. We have also demonstrated the fabrication of magnetic, fluorescent and liquid-filled PDMS microspheres that may be potential MRI contrast agents, cellular labels and drug delivery capsules respectively.

Optimizing the hydrophilicity and the biodegradability of these microspheres are potential avenues of future research. These two properties are of the highest priority when

considering intravenous delivery or prolonged incubation inside the human body. Hydrophilicity controls the amount of interaction between the microspheres and cellular media. This affects the rate of drug release as well as the ease with which microspheres can cross the cell membrane. For magnetic microspheres to be effective MRI contrast agents, maximizing the number of interactions with protons increases contrast and decreases the dosage of microspheres needed. Since the overwhelming majority of protons in the body are water molecules, hydrophilic microspheres would be ideal.

Although our microspheres have low toxicity to cell growth, it is not yet known what the effects of bioaccumulation might be. To alleviate these concerns, future focus could be placed on developing biodegradable PDMS microspheres. Thus, it may be advantageous to intentionally synthesize microspheres with bonds that are susceptible to hydrolysis, as these would easily be broken down by the body into shorter and smaller chains of PDMS that could be excreted via the kidney.

3.5 References

1) T. J. Barnes and C. A. Prestidge. PEO-PPO-PEO block copolymers at the emulsion droplet-water interface. *Langmuir*, 2000, **16**, 4116-4121.

2) R. Buzio, A. Bosca, S. Krol, D. Marchetto, S. Valeri and U. Valbusa. Deformation and adhesion of elastomer poly (dimethylsiloxane) colloidal AFM probes. *Langmuir*, 2007, **23**, 9293-9302.

3) V. Carelli, S. Coltelli, G. Di Colo, E. Nannipieri and M. Serafini. Silicone microspheres for pH-controlled gastrointestinal drug delivery. *International journal of pharmaceutics*, 1999, **179**, 73-83.

4) M. I. Goller, T. M. Obey, D. O. Teare, B. Vincent and M. R. Wegener. Inorganic "silicone oil" microgels. *Colloids and Surfaces A: Physicochemical and Engineering Aspects*, 1997, **123**, 183-193.

5) L. González, M. Baoguang, L. Li, J. H. Hansen, S. Hvilsted and A. L. Skov. Encapsulated PDMS microspheres with reactive handles. *Macromolecular Materials and Engineering*, 2014, **299**, 729-738.

6) F. Kedzierewicz†, X. Darme, A. Etienne, J. Lemut, M. Hoffman and P. Maincent. Preparation of silicone microspheres by emulsion polymerization: application to the encapsulation of a hydrophilic drug. *Journal of microencapsulation*, 1998, **15**, 227-236.

7) S. Peng, M. Zhang, X. Niu, W. Wen, P. Sheng, Z. Liu and J. Shi. Magnetically responsive elastic microspheres. *Applied Physics Letters*, 2008, **92**, 012108.

8) B. C. Thanoo and A. Jayakrishnan. Tantalum loaded silicone microspheres as particulate emboli. *Journal of microencapsulation*, 1991, **8**, 95-101.

9) O. Dufaud, E. Favre and V. Sadtler. Porous elastomeric beads from crosslinked emulsions. *J. Appl. Polym. Sci.*, 2002, **83**, 967-971.

10) K. Jiang, P. C. Thomas, S. P. Forry, D. L. DeVoe and S. R. Raghavan. Microfluidic synthesis of monodisperse PDMS microbeads as discrete oxygen sensors. *Soft Matter*, 2012, **8**, 923-926.

11) J. M. Rankin, N. K. Neelakantan, K. E. Lundberg, E. M. Grzincic, C. J. Murphy and K. S. Suslick. Magnetic, fluorescent, and copolymeric silicone microspheres. *Advanced Science*, 2015, **2**, 1500114.

12) Suslick, K. S.; Neelakantan, N. K.; Rankin, J. M. Methods of Producing Silicone Microspheres. U. S. Patent Appl. 15/004016*;* 2016.

13) W. H. Suh and K. S. Suslick. Magnetic and porous nanospheres from ultrasonic spray pyrolysis. *Journal of the American Chemical Society*, 2005, **127**, 12007-12010.

14) M. Abdullah, F. Iskandar, S. Shibamoto, T. Ogi and K. Okuyama. Preparation of oxide particles with ordered macropores by colloidal templating and spray pyrolysis. *Acta materialia*, 2004, **52**, 5151-5156.

15) J. D. Atkinson, M. E. Fortunato, S. A. Dastgheib, M. Rostam-Abadi, M. J. Rood and K. S. Suslick. Synthesis and characterization of iron-impregnated porous carbon spheres prepared by ultrasonic spray pyrolysis. *Carbon*, 2011, **49**, 587-598.

16) J. H. Bang, W. H. Suh and K. S. Suslick. Quantum dots from chemical aerosol flow synthesis: preparation, characterization, and cellular imaging. *Chemistry of Materials*, 2008, **20**, 4033-4038.

17) S.-L. Che, K. Takada, K. Takashima, O. Sakurai, K. Shinozaki and N. Mizutani. Preparation of dense spherical Ni particles and hollow NiO particles by spray pyrolysis. *Journal of materials science*, 1999, **34**, 1313-1318.

18) Y. T. Didenko and K. S. Suslick. Chemical aerosol flow synthesis of semiconductor nanoparticles. *Journal of the American Chemical Society*, 2005, **127**, 12196-12197.

19) J. H. Lee and S. J. Park. Preparation of spherical SnO2 powders by ultrasonic spray pyrolysis. *Journal of the American Ceramic Society*, 1993, **76**, 777-780.

20) J. P. Markovic, D. Jugovic, M. Mitric, D. Makovec, S. K. Milonjic and D. P. Uskokovic. Nanostructured ZrO 2 powder synthesized by ultrasonic spray pyrolysis. *Surface Review and Letters*, 2007, **14**, 915-919.

21) S. E. Skrabalak and K. S. Suslick. Porous carbon powders prepared by ultrasonic spray pyrolysis. *Journal of the American Chemical Society*, 2006, **128**, 12642-12643.

22) H. Xu, J. Guo and K. S. Suslick. Porous carbon spheres from energetic carbon precursors using ultrasonic spray pyrolysis. *Advanced Materials*, 2012, **24**, 6028-6033.

23) R. J. Lang. Ultrasonic atomization of liquids. *The journal of the acoustical society of America*, 1962, **34**, 6-8.

24) T. T. T. Kodas and M. J. Hampden-Smith. *Aerosol processing of materials*, Wiley-Vch, 1999.

25) J. W. Overcash and K. S. Suslick. High Surface Area Iron Oxide Microspheres via Ultrasonic Spray Pyrolysis of Ferritin Core Analogues. *Chemistry of Materials*, 2015, **27**, 3564-3567.

26) S. E. Skrabalak and K. S. Suslick. Porous MoS2 synthesized by ultrasonic spray pyrolysis. *Journal of the American Chemical Society*, 2005, **127**, 9990-9991.

27) W. H. Suh, A. R. Jang, Y. H. Suh and K. S. Suslick. Porous, Hollow, and Ball-in-Ball Metal Oxide Microspheres: Preparation, Endocytosis, and Cytotoxicity. *Advanced Materials*, 2006, **18**, 1832-1837.

28) Y. Zhang and K. S. Suslick. Synthesis of Poly (3, 4-ethylenedioxythiophene) Microspheres by Ultrasonic Spray Polymerization (USPo). *Chemistry of Materials*, 2015, **27**, 7559-7563.

29) J. N. Lee, C. Park and G. M. Whitesides. Solvent compatibility of poly (dimethylsiloxane)-based microfluidic devices. *Analytical chemistry*, 2003, **75**, 6544-6554.

30) B. C. Arkles and G. L. Larson. *Silicon compounds: silanes and silicones: a survey of properties and chemistry*, Gelest, Incorporated, 2004.

31) A. F. Chrimes, K. Khoshmanesh, P. R. Stoddart, A. Mitchell and K. Kalantar-zadeh. Microfluidics and Raman microscopy: current applications and future challenges. *Chemical Society Reviews*, 2013, **42**, 5880-5906.

32) G. Camino, S. Lomakin and M. Lazzari. Polydimethylsiloxane thermal degradation Part 1. Kinetic aspects. *Polymer*, 2001, **42**, 2395-2402.

33) R. Johnson, R. Biefeld and J. Sayre. High-temperature electrical conductivity and thermal decomposition of Sylgard® 184 and mixtures containing hollow microspherical fillers. *Polymer Engineering & Science*, 1984, **24**, 435-441.

34) C. Gelsest. Reactive silicones: forging new polymer links. *Gelest Inc, Morrisville, Pennsylvania, Available at: www.gelest.com/company/ pdfs/reactivesilicones.pdf*, 1967.

35) B. Arkles, Larson, G. L., Ed. *Silicon Compounds: Silanes & Silicones, 5000A, 3rd ed*, Gelest Inc, Morrisville, PA., 2013.

36) G. Meszlényi, M. Sipos, É. Juhász, M. Eröss-Lelkes and G. Poszmik. Infrared spectroscopic investigation of propylene oxide-ethylene oxide polymers. *Acta Physica Hungarica*, 1988, **63**, 137-140.

37) J. Rankin, Ph.D., University of Illinois, Urbana-Champaign, 2015.

38) J. W. Pickering, T. B. Martins, R. W. Greer, M. C. Schroder, M. E. Astill, C. M. Litwin, S. W. Hildreth and H. R. Hill. A multiplexed fluorescent microsphere immunoassay for antibodies to pneumococcal capsular polysaccharides. *American journal of clinical pathology*, 2002, **117**, 589-596.

39) J. M. Anderson and M. S. Shive. Biodegradation and biocompatibility of PLA and PLGA microspheres. *Advanced drug delivery reviews*, 2012, **64**, 72-82.

40) Y. Kobayashi, K. Misawa, M. Kobayashi, M. Takeda, M. Konno, M. Satake, Y. Kawazoe, N. Ohuchi and A. Kasuya. Silica-coating of fluorescent polystyrene microspheres by a seeded polymerization technique and their photo-bleaching property. *Colloids and Surfaces A: Physicochemical and Engineering Aspects*, 2004, **242**, 47-52.

41) N. Bodor and P. Buchwald. Recent advances in the brain targeting of neuropharmaceuticals by chemical delivery systems. *Advanced drug delivery reviews*, 1999, **36**, 229-254.

42) P. Mura, F. Maestrelli, M. L. González-Rodríguez, I. Michelacci, C. Ghelardini and A. M. Rabasco. Development, characterization and in vivo evaluation of benzocaine-loaded liposomes. *European Journal of Pharmaceutics and Biopharmaceutics*, 2007, **67**, 86-95.

CHAPTER 4: SHOCK ANALYSIS OF SILICONE-BONDED EXPLOSIVES

4.1 Background

Energetic materials are a class of compounds that store large amounts of chemical energy to be released. These compounds include, but are not limited to, propellants, explosives and pyrotechnics.[1,2] This chapter will focus on research regarding explosives, specifically, composites made from powdered crystalline energetic materials with a silicone binder. To that end, a brief overview of explosives will be given in the first half of section 4.1.

The second half of section 4.1 will deal with shock-induced hotspots. The shock response of energetic materials is incredibly important, as it has broad implications on how much energy the material releases, what type of impact is necessary to trigger such an event and which applications the material is suitable for. Thus, a brief introduction to mechanical shock and its effects is necessary to understand the scope of this chapter, with specific regard as to how shock causes hotspots to form.

4.1.1 Primary Explosives

Primary explosives are defined by their high sensitivity to ignition from such sources as heat, impact (i.e., drop hammer) and electrical discharge, which cause them to readily undergo detonation.[3, 4] Due to this property, primary explosives are not used in large quantities by themselves, as safety and stability is an issue. Thus, their applications are generally limited to ignition sources for more stable and less sensitive energetic materials, such use as detonators. **Figure 4.1a-c** shows the chemical structure of some commonly used primary explosives, while **4.1d** shows a schematic for a detonator. A detonator is a device that has a triggering mechanism

and a small amount of primary explosive to initiate the detonation of a less sensitive compound. The detonator shown in **4.1d** is an exploding bridgewire (EBW) detonator. It uses an electrical discharge to vaporize a thin wire into plasma, generating a shockwave that launches the wire material into the primary explosive. The impact then triggers the detonation of the primary explosive, which in turn detonates the less sensitive explosive. The EBW design allows for extreme precision of detonation time and therefore finds use in nuclear weapons, where this is of utmost necessity.

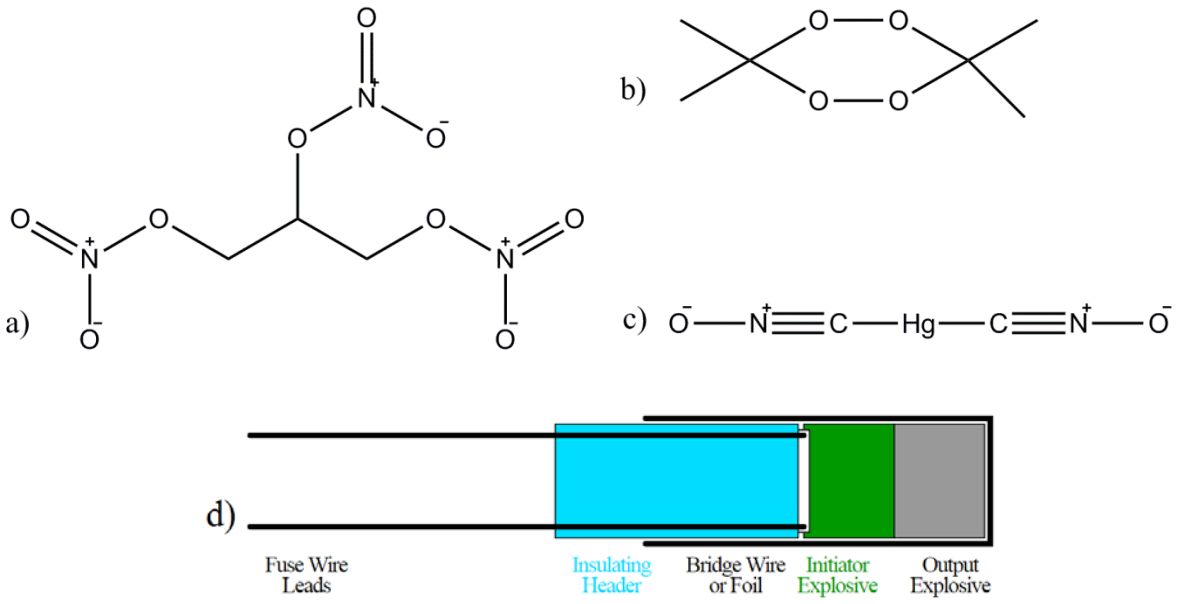

Figure 4.1 Representative primary explosives, a) Nitroglycerin, b) diacetone diperoxide, c) mercury fulminate and d) diagram of an exploding bridgewire (EBW) detonator (raster: George William Herbert, vectorization: Mliu92).

4.1.2 Secondary Explosives

Unlike primary explosives, secondary explosives are very difficult to detonate by simple impact, heating or electrical stimulation. Their insensitivity and stability makes them very safe for use in practical applications.[5] They are used in conjunction with initiators such as blasting

caps or detonators, such as the one shown in 4.1d, as part of an explosive train (output explosive). The structure of some of the more common secondary explosives is shown below in **Figure 4.2**. Some common characteristics of secondary explosives are a high amount of N-N, N-O and C-N bonds, which store large amounts of energy, as well as extremely low vapor pressures, which render them particularly difficult to detect.

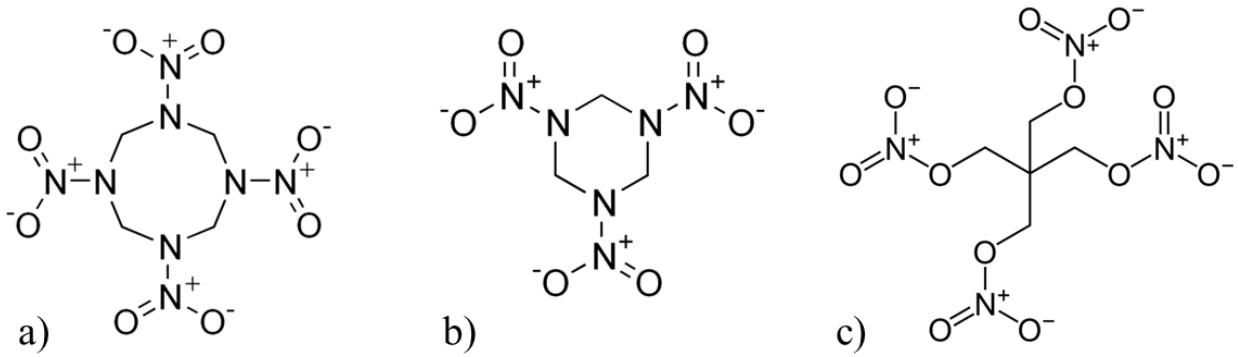

Figure 4.2 Representative secondary explosives, a) HMX (Octahydro-1,3,5,7-tetranitro-1,3,5,7-tetrazocine), b) RDX (Cyclotrimethylenetrinitramine), and c) Pentaerithrytoltetranitrate (PETN).

It should be noted that there is no objective standard for drawing a line between primary and secondary explosives; the most sensitive secondary explosive could just as easily be classified as the least sensitive primary explosive. Sensitivity tests can rank explosives from least to most sensitive, but these are often based on qualitative rather than quantitative results.

4.1.3 Polymer-Bonded Explosives (PBX) and Plastic Explosives

Secondary explosives, such as the ones shown in the previous subsection, are often combined with a polymeric binder to make polymer-bonded explosives (PBX). While any explosive can be used neat, PBX are most frequently used for military purposes because of the degree of control they offer; they can be molded and machined into very specific shapes, which

allows for the detonation energy to be directed. Alternatively, PBX can be formulated with a plasticizer to make plastic explosives, which offer malleability.

Table 4.1 shows the formulations of some of the most common PBX materials and their general applications. Polymer binders vary from Viton (a fluorinated polyethylene) and estane (a polyurethane) to Sylgard (polydimethylsiloxane elastomer).

Table 4.1 Composition of PBX and their Uses[6, 7]

Explosive	Formulation (wt %)	Usage
Composition B	69.5% RDX, 39.5% TNT, 1% wax	Common fill for explosive ordnance
C-4	91% RDX, 2.1% polyisobutylene, 1.6% motor oil, 5.3% DOS (plasticizer)	Demolition of structures/obstacles.
PBX-9501	95% HMX, 2.5% Estane, 2.5% BDNPF (plasticizer)	Explosive lens, shaped charges for nuclear ordnance
XTX-8003	80% PETN, 20% Sylgard 182	Extrudable plastic explosive, small failure diameter.

One very common application of PBX is their use as shaped charges in missile warheads. A shaped charge,[8] such as the explosive lens of a nuclear weapon, is necessary to trigger a fissile chain reaction. This requires specific machining and resistance to deformation, making a rigid PBX the ideal choice. A schematic of such a charge is shown in **Figure 4.3**. The explosive shell focuses the detonation energy at different points in the fissile core, maximizing the number of simultaneous nuclear chain reactions.

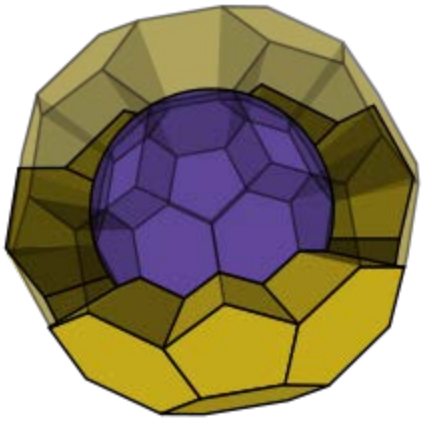

Figure 4.3 Schematic of an explosive lens (yellow shell) for a fissile core (purple) in a nuclear weapon.

4.1.4 Mechanism and Effects of Shock-Initiated Hotspots on Explosives

A mechanical shock occurs when a large force is applied in a short period of time relative to a structure of interest.[9] Explosives can be detonated using mechanical shocks that cause extreme and rapid heating. This rapid heating generally takes the form of hotspots that propagate throughout the explosive, generating the initial heat and gases associated with the subsequent explosion.[10] It is generally agreed that the formation of localized hotspots upon shock impact is crucial to this detonation process.[11-13] This section will discuss the mechanism behind shock-initiated hotspots as it pertains to the findings of this thesis.

While many theoretical models exist for hotspot formation, the structure of the compound of interest can give insight into which model has the most explanatory power. For instance, the structure of plastic explosives (examples shown in **Figure 4.4**) is heterogeneous and contains many pores and voids that may be capable of concentrating mechanical energy into a hotspot. Many experiments have shown that the presence of pores has a sensitizing effect on explosives.[14,15]

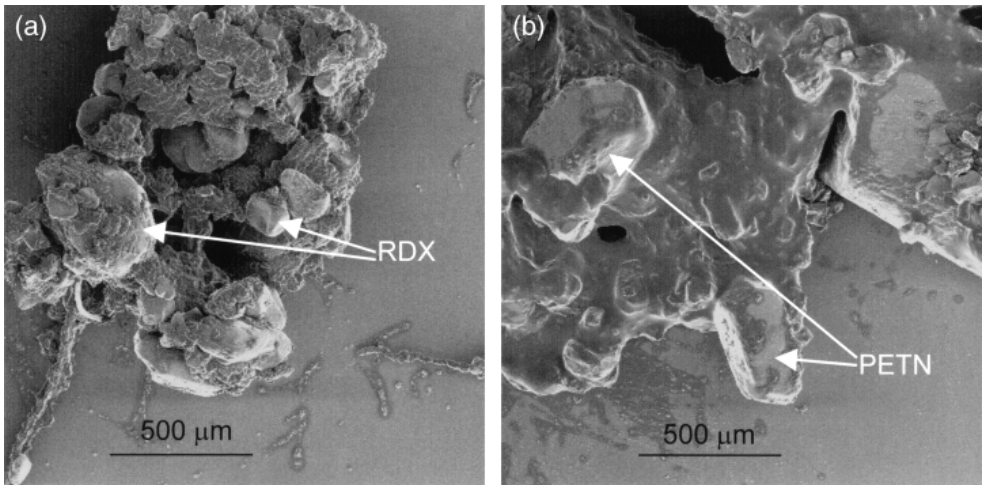

Figure 4.4 Scanning electron micrograph of (a) C-4 and (b) Semtex 1-A, plastic explosives. Examples of individual explosive crystals are marked by arrows.[16]

Two models have been used to explain the effect of pores based on pore size: 1) For large pores (50 μm to 1 mm in diameter), adiabatic heating of gases upon compression,[17] 2) For small pores (<1 μm in diameter), viscous and plastic heating mechanisms.[12] In order to explore how pores affect hotspot formation, we characterized the shock response of XTX-8003, an extrudable plastic explosive made of PDMS and PETN, using laser-launched Al foil plates as the shock source. The ongoing studies give insight into which mechanism predominates under specific conditions. These results are of great pertinence to explosives engineering, as an excess of defects such as pores may disadvantageously increase the sensitivity of a compound to unsafe levels.

4.2 Experimental

4.2.1 Laser-Driven Flyer Plate Apparatus

The following experiments were done in collaboration with Will Bassett and Professor Dana Dlott. The flyer plate apparatus[18] is a convenient way to generate highly reproducible shocks in an energetic material at the velocities present in real-life scenarios. **Figure 4.5**a shows a schematic of the apparatus used in the following experiments. Briefly, a 1550 nm Nd:YAG laser heats the back of the flyer plate substrate, which is a borosilicate glass with a layer of aluminum foil epoxied to the inside face with Eccobond 24 (Henkel). The heating causes the aluminum foil to undergo vaporization and rapidly generates Al plasma. This plasma rapidly expands and causes a shockwave that launches the Al foil outward and onto the sample substrate. Though this assembly is simply used a source of shock initiation, it is remarkably similar in mechanism to the EBW detonator shown in **Figure 4.1**. Thus the flyer plate is an excellent mimic for real-life detonation of explosives.

The sample substrate is also a glass plate, but with a thin layer of the compound of interest spread into a well (**Figure 4.5b**). This plate is separated from the flyer plate by a 375 μm spacer. Experiments can be done in vacuum or in the presence of a gas. A comparison of the well size and the detection area is shown in **Figure 4.5**c. The central 50 μm (red) of the 1 mm well is used to gather flyer velocity and spectral data. Flyer velocity is determined using a photon Doppler velocimeter. The spectral data is gathered by a series of photomultiplier tubes (PMT) with a range of 442-822 nm. Using a graybody model,[20] the emission data can be converted to temperature as a function of time with high resolution (2 ns).

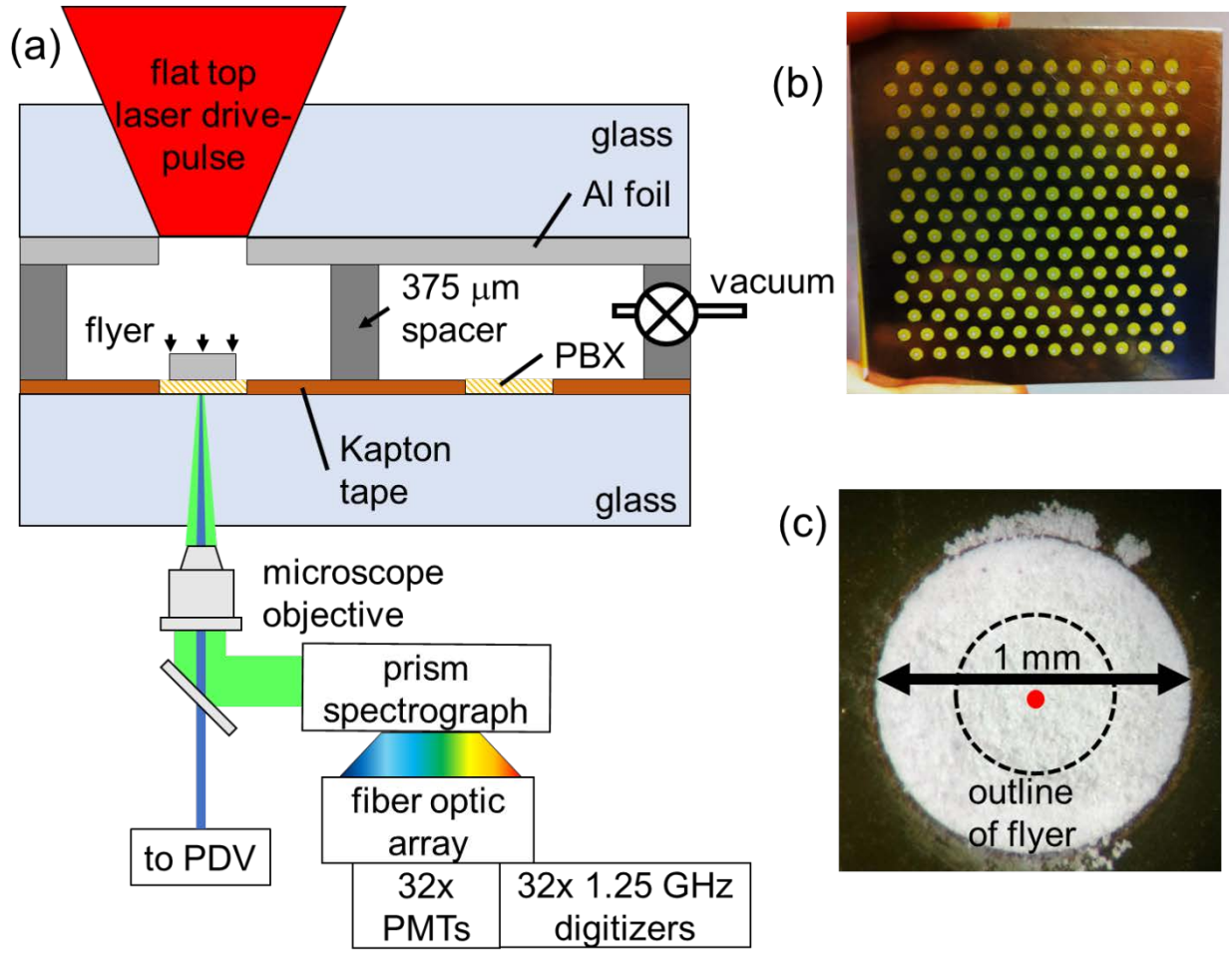

Figure 4.5 a) Schematic of the flyer plate apparatus, b) An exemplary glass plate filled with polymer bonded explosive (PBX) wells, c) optical image of an individual well with target area shaded in red.[19]

One factor that needs to be accounted for is that hotspots are not uniformly distributed over the analyzed shock area. **Figure 4.6** shows a PBX sample undergoing shock from a flyer plate with hotspot intensity color-mapped in red; the sample is not emitting radiation uniformly and thus, we must use an emissivity that is spatially averaged over the shock area. This emissivity parameter is defined as

$$\Phi = \varepsilon V^*$$

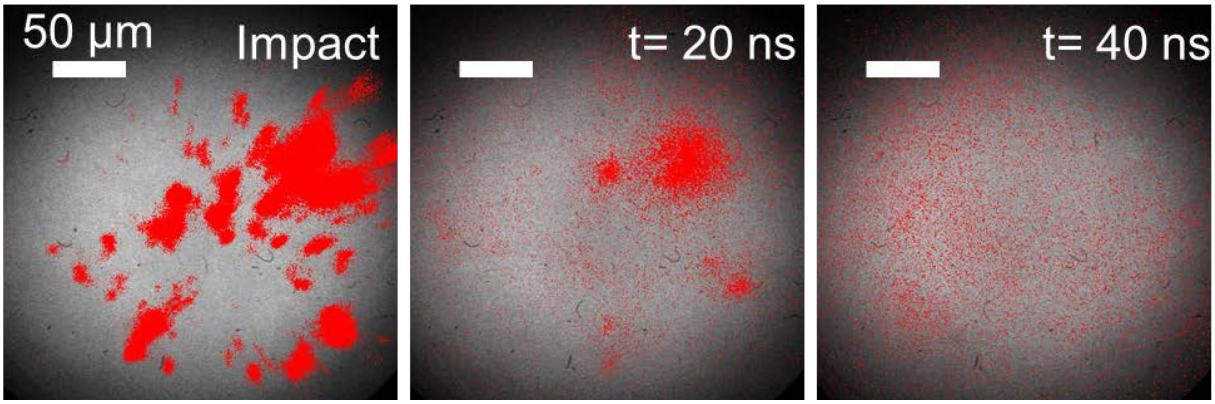

Figure 4.6 Time-lapsed images of a PBX sample undergoing impact by a 25 µm flyer plate at impact, 20 ns and 40 ns. The red spots represent light emitting pixels from the sample. The integration time for each image was 20 ns.

Where ε is the bulk emissivity and V^* is the volume fraction of the emitting hotspots. This value allows us to evaluate the growth, decay and relative strength of hotspots as a function of time, alongside the temperature emission data.

4.2.2 Materials

Pentaerithrytol nitrate (PETN) was obtained from Los Alamos National Laboratory. Hexanes (Fisher Scientific), methanol (Fisher Scientific) and acetone (Fisher Scientific) were used as received. Sylgard 184 (Polydimethylsiloxane (PDMS), Dow Corning) was used as received. Kapton tape of 40 µm and 80 µm thickness were obtained from Caplinq Inc. Starphire glass slides (75 mm x 75 mm x 6.35 mm) were obtained from Fusion Glassworks. Aluminum foil (Allfoils) 0.001” (25 µm) was used as received. Sucrose crystals and silica powder, 5 µm, (both Sigma Aldrich) were used as received.

4.2.3 Formation of PETN Powder

Large PETN crystals were dissolved in acetone to give a final concentration of approximately 150 mg/mL. This PETN solution was then added dropwise with a Pasteur pipet to a vial of excess distilled water (i.e. roughly 10 times the amount of PETN solution). The precipitated PETN in the acetone-water solution is then vacuum filtered dropwise through a Buchner funnel and washed with hexanes and methanol. The filtrate is then recovered as a fine powder of PETN.

4.2.4 Sylgard Coating of PETN

In a 20 mL scintillation vial, 300 mg of Sylgard 184 Elastomer (PDMS) were added at a 10:1 ratio of base to curing agent (i.e. 272 mg of base and 27 mg of curing agent) and dissolved in hexanes to give a final concentration of 30 mg/mL. The fine PETN powder prepared in the previous step is weighed and added to a vial and the PDMS-hexane solution is added to the PETN so that there is an 80:20 weight ratio of PETN to PDMS. A mechanical stir bar is added to the vial and stirred at low RPM overnight at room temperature so that the hexane is evaporated and the PDMS cures evenly. It should be noted that the standard formulation for XTX-8003 uses Sylgard 182; Sylgard 184 is virtually identical but cures faster at room temperature.

4.2.5 Pressing of PETN/PDMS Composite

The compound prepared in 4.2.4 is initially a ‘crumbly’ mixture of PETN powder and elastomer. In order to convert this mixture into a smooth and spreadable film, the crumbly mixture was pressed in a hydrostatic press at 2000 psi for 1 minute and subsequently spread as thinly as possible between two surfaces (in this case, using the back of a spatula and a razor

blade). This is done repeatedly to ensure that there is no loose powder in the mixture. The final product has a soft putty-like consistency that stretches across a surface when spread.

4.2.6 Silica and Sucrose Controls for XTX-8003

The procedure described in 4.2.4 can be done using silica or sucrose powder instead of PETN to make an inert analog for XTX-8003. Silica or sucrose were added to the same solutions of PDMS in hexane at a weight ratio of 80:20 (silica/sucrose:PDMS) and used as is after evaporation of hexane at room temperature. This acts as a control for the unpressed XTX. The procedure in 4.2.5 may be used to again convert this material to the pressed XTX analogs.

4.2.7 XTX-8003 Wells for Flyer Plate Experiments

Kapton tape was adhered to 75 x 75 x 6.35 mm glass slides and 1 mm circular wells were laser cut into the slide by the University of Illinois Machine shop. For flyer plate experiments 187 wells are cut into to each glass slide, with 150 containing a sample of interest and the remaining empty holes used for velocity determination. XTX-8003 or silica/sucrose analog was spread into each well one at a time using a metal spatula.

4.2.8 Characterization

Electron microscope images of samples were taken using a JEOL 7000F and a Philips XL30 ESEM-FEG scanning electron microscope. Samples were sputter-coated with Au/Pt for 20-30 sec (a thickness of 7-8 nm) prior to image acquisition.

Particle size distribution was done using ImageJ software and averaging the size of >120 individual crystals, as observed under electron microscope.

CHN analysis was performed by the University of Illinois School of Chemical Sciences Microanalysis Laboratory using an Exeter Analytical, Inc. Model CE-440 CHN analyzer.

Profilometry was carried out on a Dektak 3030. Linescans were between 1000 and 5000 µm, and the applied force was generally 15 N. Multiple sample heights were averaged to calculate relative density.

4.3 Results and Discussion

4.3.1 Characterization and Shock Analysis of XTX-8003

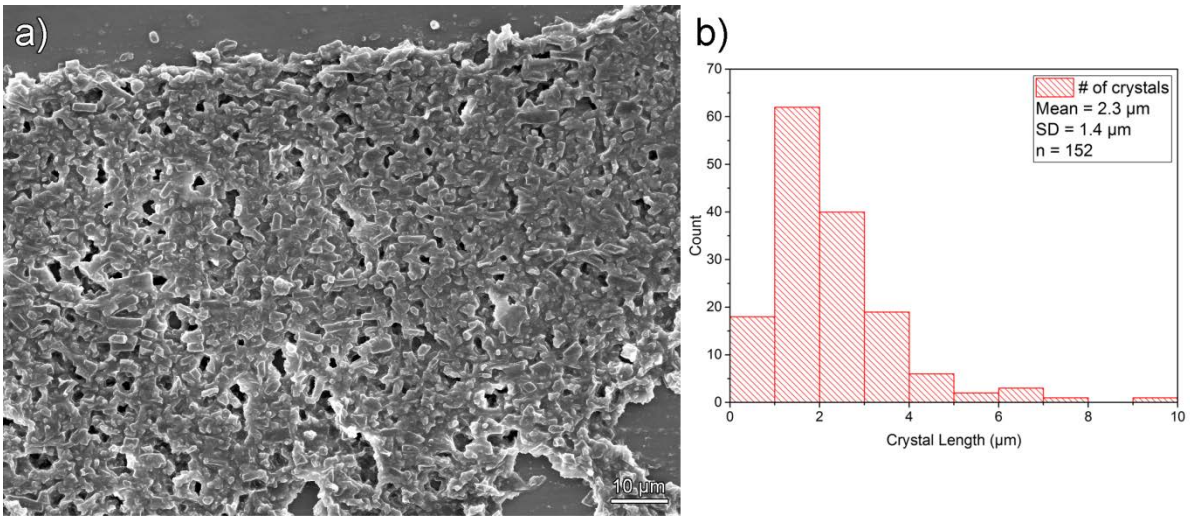

Figure 4.7 a) Scanning electron micrograph of homogenized and pressed XTX-8003. Scale bar is 10 µm. b) Particle size of the same image reported as crystal length.

Current shock research is generally limited to computer modelling and qualitative experiments that rely heavily on subjective observations and binary 'go'/'no-go' conditions.[21-24] To understand how shock affects these compounds and what processes take place, a quantifiable and reproducible measurement would be highly desirable. We developed a scaled down method for producing XTX-8003, a plastic explosive consisting of 80 wt % PETN and 20 wt % Sylgard elastomer (PDMS). The at-scale procedure involves vortex mixing large quantities of the two compounds and then pressing into a smooth sheet using a three-point mill. Since only lab-scale

amounts are necessary and safe for the aforementioned experimental section, our XTX-8003 was subject to a hydrostatic press and folding/spreading step to mimic the authentic procedure. An SEM of the final product is shown in **Figure 4.7**. Individual crystals can be seen held together by the PDMS matrix. Most particles were approximately 2 µm in length (4.7b).

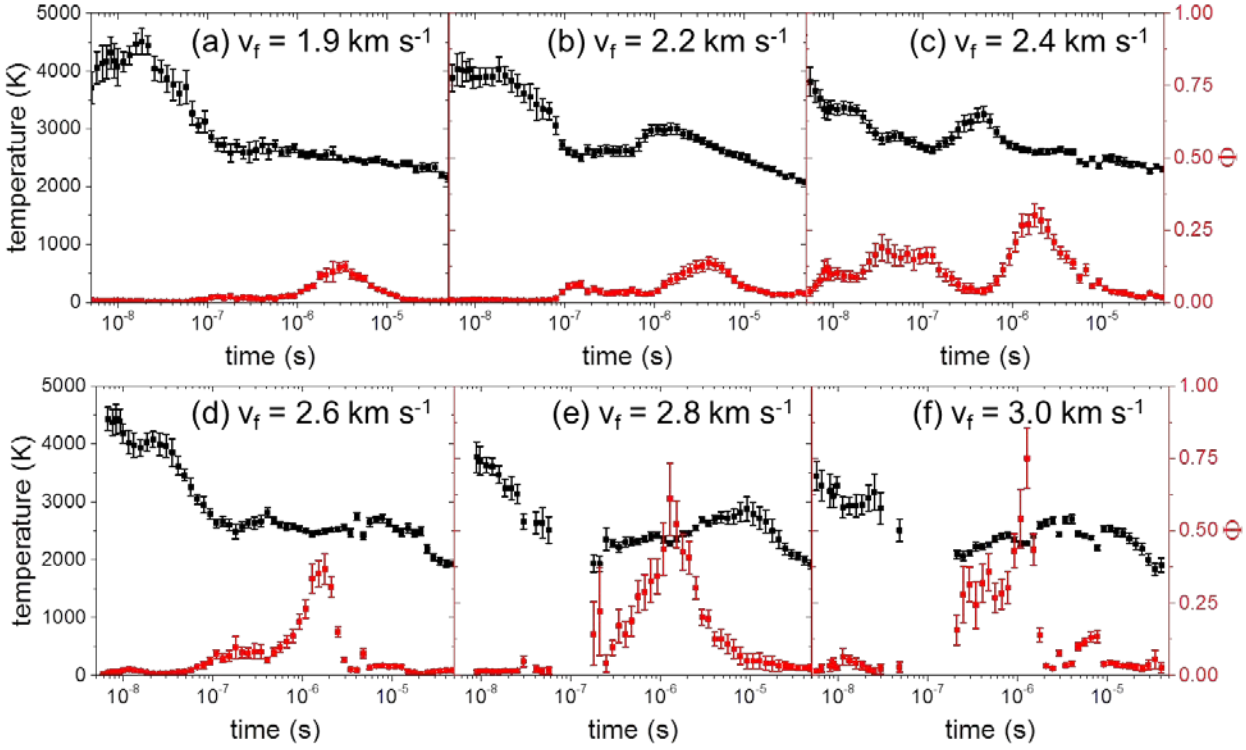

Figure 4.8 Flyer plate impacts of homogenized XTX under vacuum at various flyer velocities (v_f). Impact at a) 1.9, b) 2.2, c) 2.4, d) 2.6, e) 2.8 and (f) 3.0 km s^{-1}. Red = emissivity (Φ), black = T, graybody temperature.

In order to study the shock mechanics of XTX-8003, the flyer plate apparatus, as previously described, was used to launch foil plates of 25 µm length at various speeds. These plates impact the XTX-8003 and the resultant thermal emission was recorded from 1.9 km/s to 3.0 km/s flyer velocity (**Figure 4.8).** The data output is shown in terms of graybody temperature as well as the parameter Φ, the spatially averaged emissivity, with respect to time. As can be seen in **Figure 4.8**, for flyer velocities from 1.9 km/s to 3.0 km/s, the maximum temperature

achieved is between 4000 and 4500 K. The fraction of the sample emitting light is insignificant until the plateau of 2500 K occurs in the microsecond range. This plateau can be ascribed primarily to triboluminescence of the glass substrate; the plateau occurs even when bare glass is shocked under vacuum by a flyer plate. Minor events such as deflagration and smoldering may also be occurring as well.

Table 4.2 Relative density and CHN analysis of tested explosive compounds, theoretical values in parentheses

Compound	Relative Density	Carbon wt%	Hydrogen wt%	Nitrogen wt%
Pressed XTX	88 ± 3%	21.5 (21.6)[a]	3.5 (3.6)[a]	12.1 (14.2)[a]
Unpressed XTX	79 ± 9%	21.4 (21.6)[a]	3.6 (3.6)[a]	12.5 (14.2)[a]
Neat PETN	~30%[b]	19.4 (19)	2.3 (2.5)	16.1 (17.7)

[a] Ref 5
[b] estimated from prior experiments with similar HMX powder[19]

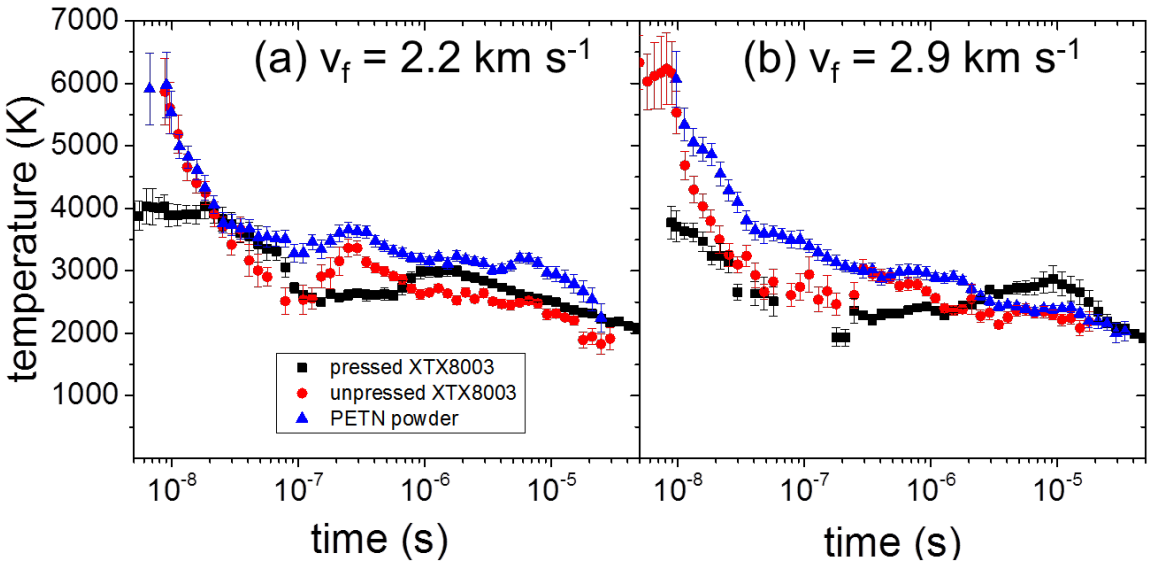

Figure 4.9 Flyer plate impacts of pressed XTX, unpressed XTX and PETN powder under vacuum at (a) 2.2 and (b) 2.9 km s^{-1} flyer velocity.

We also subjected an unpressed XTX-8003 (properties shown in **Table 4.2**) to shock, as well as neat PETN powder. In sharp contrast to pressed XTX, both show rapid heating to 6000

K. A comparison of all three samples (unpressed XTX, pressed XTX and PETN powder) at two different flyer velocities is given in **Figure 4.9**. These results suggest that the unpressed (raw) XTX has more porosity than the pressed XTX, since the PETN crystals were loaded into the wells as loose powder. It also suggests that porosity and poor packing are properties that the unpressed XTX shares with the PETN crystals. Indeed, the density is lower and variance in density is greater in the unpressed sample.

The unpressed XTX contains mostly bare crystals of PETN that are totally exposed at the surface. There is no evidence from the SEM that the PDMS has been homogenously incorporated into the mixture (**Figure 4.10a**). The PETN crystals themselves are somewhat larger on average when compared to the fully pressed XTX (7 μm on average compared to ~3 μm, **4.10b**). It appears that hydrostatic pressing crushes some of the larger crystals.

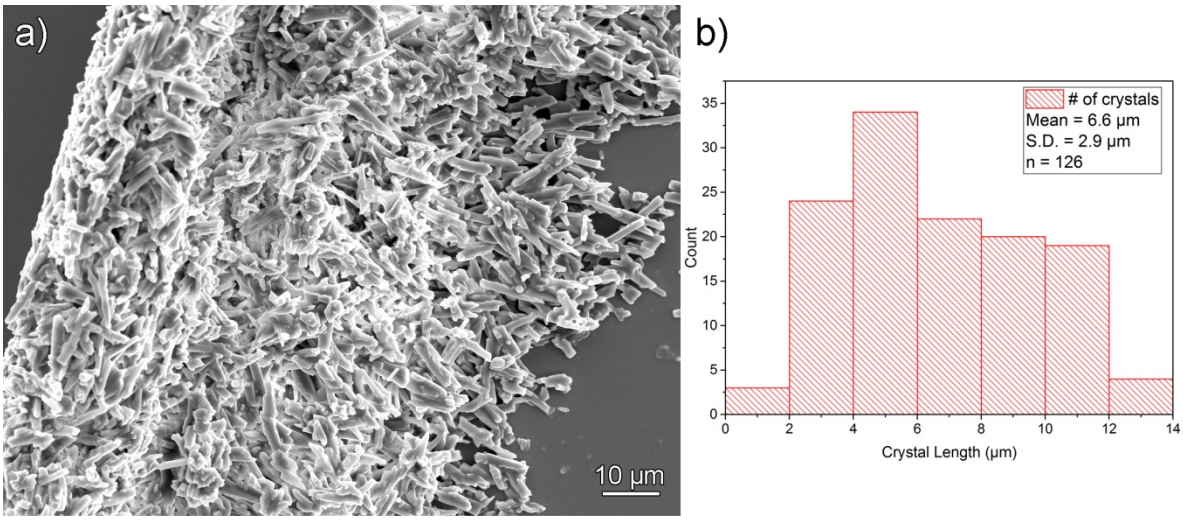

Figure 4.10 a) Scanning electron micrograph of unpressed XTX-8003. Scale bar is 10 μm. b) Particle size of the same image reported as crystal length.

The thermal behavior of the 'crumbly' unpressed XTX was also somewhat different from that of its pressed counterpart when subjected to various flyer velocities (**Figure 4.11**).

When shocked with flyer plates of similar velocities, the maximum temperatures observed sometimes approached ~5500 K, over 1000 K hotter than the hottest temperature observed in the pressed XTX. Additionally, the sample emits light erratically and well in to the microsecond regime.

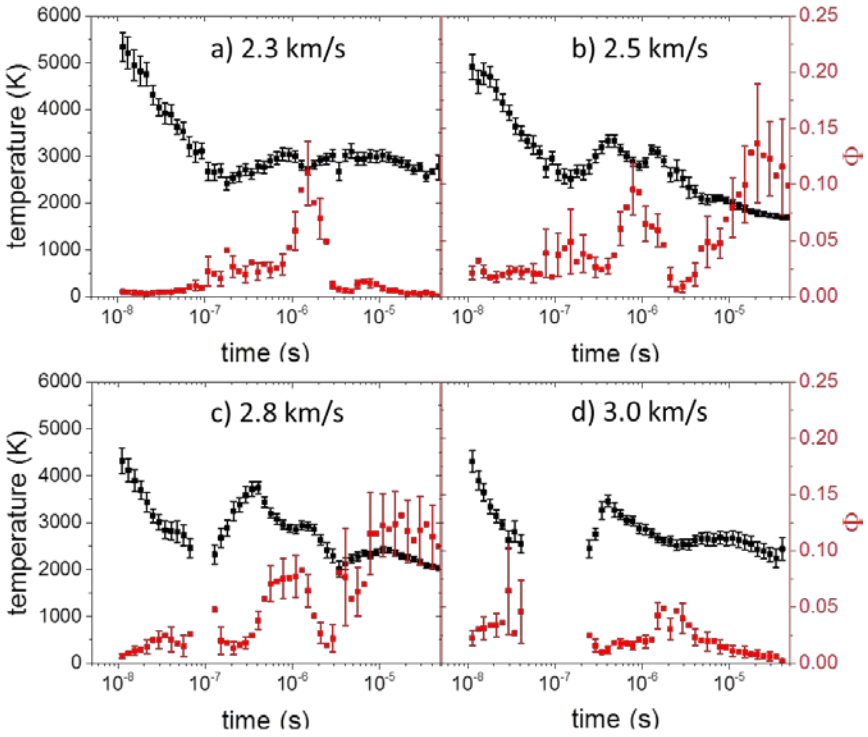

Figure 4.11 Flyer plate impacts of unpressed XTX under vacuum at various flyer velocities (v_f). Impact at a) 2.3, b) 2.5, c) 2.8 and (d) 3.0 km s^{-1}.

Sample degradation is not suspected as the cause of the erratic behavior; both XTX samples were of similar chemical composition (**Table 4.2**). However, the SEM of the unpressed XTX in **Figure 4.10** suggests that the PETN crystals are poorly packed at the surface, creating cavities that gases could occupy. Since the experiments are done *in vacuo*, the gases would necessarily be generated by the breakdown of the PETN into N_2, CO_2, etc. These gases could then undergo adiabatic compression and be the source of the high temperatures we sometimes

observed. Though the temperature spike in unpressed XTX was inconsistent, we further explored the effects of porosity in explosive sensitivity.

4.3.2 Heating Response of XTX-8003 under Various Gas Environments

Perhaps the most definitive proof of adiabatic heating we obtained was by shocking pressed XTX-8003 in the presence of various gases. Since there is no heat transfer involved in an adiabatic process, all of the heat rise can be attributed to the compression of the gas volume, which follows the equation:

$$\frac{T_2}{T_1} = \left(\frac{V_1}{V_2}\right)^{\gamma-1}$$

Where T_1 and V_1 are the initial temperature and volume of the gas, and T_2 and V_2 are the final temperature and volume of the gas, and γ is the isentropic expansion factor, which is calculated as:

$$\gamma = \frac{C_p}{C_v} = 1 + \frac{2}{f}$$

Where f is the degrees of freedom a gas can have (i.e. rotations, translations), depending on the identity of the gas and the temperature. C_p and C_v are the heat capacities at constant pressure and volume respectively. The implication is that the more translational and rotational modes a gas molecule has, the more heat it can dissipate.

The following gases were allowed to fill the chamber. Their heat capacities and gamma values are given in **Table 4.3**. Since air is roughly diatomic, we chose a monoatomic gas (Ar) and CO_2 as a triatomic gas. The limiting case of $\gamma = 1$ was approximated by butane.

Table 4.3 Heat Capacity (C_p) and isentropic expansion factor (γ) of test gases

Test Gas	Heat Capacity ($J/mol^{-1}K^{-1}$ at 298 K)	Isentropic Expansion Factor (γ)
Argon	21	1.66
Dry Air, pure N_2, pure O_2	29	1.40
Carbon Dioxide	37	1.30
Acetylene	49	1.20
Butane	98	1.08

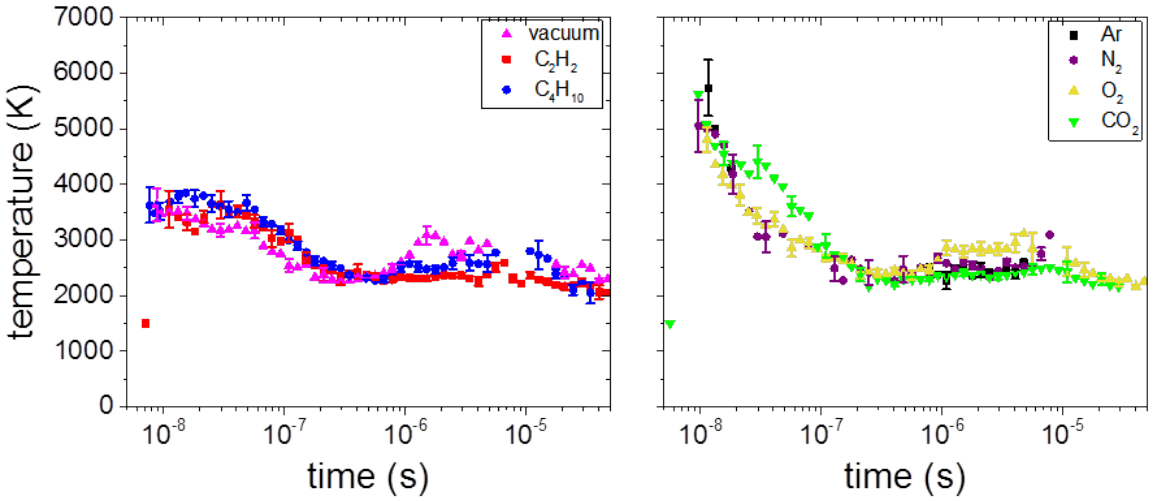

Figure 4.12 Flyer impact of pressed XTX-8003 in various gas environments. Solid shapes refer to temperature and hollow shapes refer to average emissivity.

The gases show a binary response of 4000 K peak temperature in acetylene and butane vs. 6000 K peak temperature in the mono-, di- and tri-atomics (**Figure 4.12**). The 4000 K appears to be a baseline response, as blank samples (i.e., bare glass) shocked in vacuum and butane show no heating at all. This means that the heating is coming from gases generated by the decomposition of XTX during shock impact. The rest of the gases all look similar for two reasons: 1) it is likely that dissociation and possibly ionization events are occurring, both of which are highly endothermic, 2) the temperature sensitivity of the instrument is low because it is near the upper-bound of the detection limit. For instance, argon, if compressed adiabatically to

near its liquid density inside the pores of XTX, would reach a temperature of nearly 24000 K. This is impossible as plasma is formed at far lower temperatures.

Table 4.4 Gas environment of XTX samples, temperature at peak energy emission (Tavg) and isentropic expansion factor (γ) of test gases

Gas Environment of XTX samples	T_{avg} (K)[a]	Isentropic Expansion Factor (γ)
Butane	3450	1.08
Acetylene	3500	1.20
Carbon Dioxide	4630	1.30
Nitrogen	5640	1.40
Oxygen	5300	1.40
Argon	5800	1.66

[a]Rel. Std. Dev. was 6-7% in all cases.

When examining XTX sample temperatures at the peak of their spectral radiance, a trend is seen relative to γ (**Table 4.4**). Peak spectral radiance represents the peak emitted energy of each sample and is a convenient way to compare shocked samples in various gas environments at their point of maximal heating. This is because emitted energy is proportional to T^4. The T_{avg} in **Table 4.4** represents the temperature at peak intensity across multiple samples in each gas environment. There is an increase in temperature relative to an increase in γ, although it is only moderate. One major explanation is that γ decreases with respect to temperature, and it is unclear that the gases being generated or compressed are at room temperature when the process begins. Secondly, given the possibility of ionization events, as previously discussed, it is likely that much higher temperatures cannot be sustained.

4.3.3 Heating Response of Inert Simulants

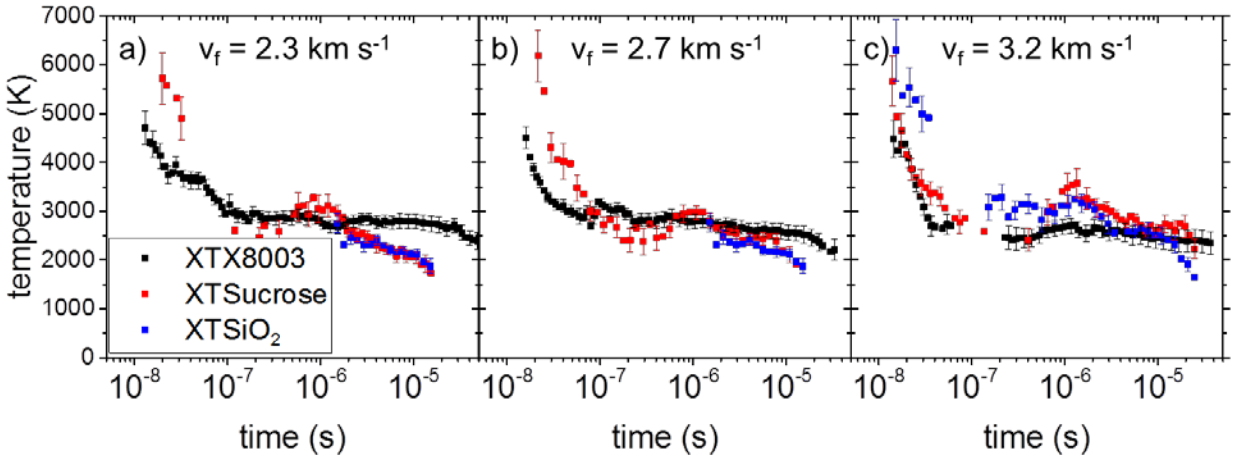

Figure 4.13 Flyer plate impacts of pressed XTX, unpressed sucrose analog (XTSucrose) and unpressed silica analog ($XTSiO_2$) under vacuum, at (a) 2.3, (b) 2.7 and (c) 3.2 km s^{-1} flyer velocity.

By replacing PETN with sucrose (XTSucrose) or silica ($XTSiO_2$) in our XTX formulations, we were able to make inert simulants. These simulants were not pressed, and thus mimic the unpressed XTX in terms of porosity. When subject to shock, they behave identically to their unpressed XTX counterpart and eventually reach >6000 K (**Figure 4.13**). Previous experiments[19] showed that silica by itself does not show any heating when shocked (i.e. it does not generate any gas), indicating that the PDMS plays a role in the decomposition process. Gases generated from PDMS breakdown can be compressed adiabatically and generate the high temperatures seen from 10^{-8} to 10^{-7} seconds. This is evidence that porosity sensitizes samples to adiabatic heating. Though the temperatures of the controls match that of XTX, the total radiance of the inert controls is far lower than that of XTX. This is expected because neither of them has that store large amounts of energy to be released (e.g., N-N and N-O single bonds).

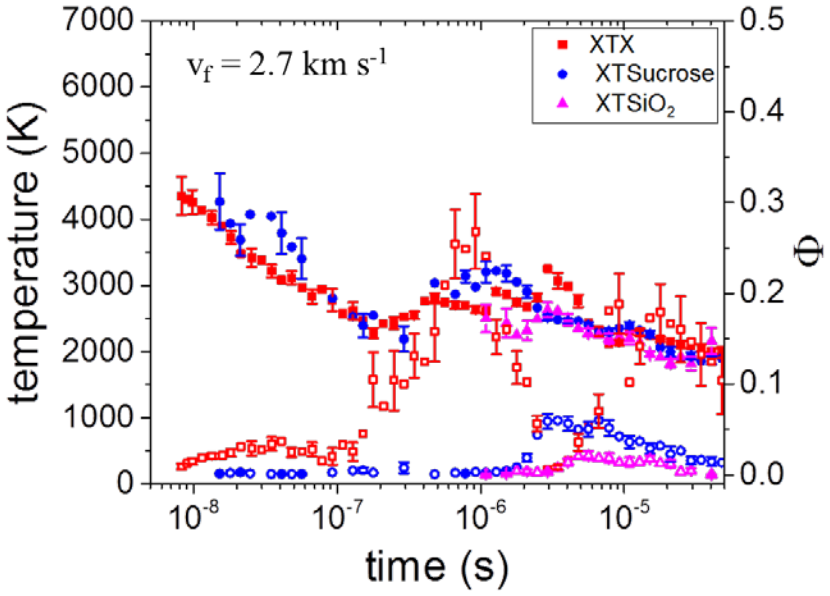

Figure 4.14 Flyer plate impacts of pressed XTX, pressed sucrose analog (XTSucrose) and pressed silica analog ($XTSiO_2$) under vacuum, at 2.7 km s^{-1} flyer velocity.

In sharp contrast, the thermal behavior of the pressed sucrose analog is identical to that of the pressed XTX while the silica analog does not heat at all until 1 μs (**Figure 4.14**). This further evinces the idea that adiabatic heating of gases generated in situ is responsible for ns hotspot formation. Both XTX and sucrose can generate a variety of gases such as nitrogen (XTX only), water and carbon dioxide. One major difference is in the total emissivity, which is far lower for sucrose than XTX. This is because the decomposition of XTX is far more exothermic than that of sucrose.

Pressed silica analogs on the other hand underwent no decomposition in the first microsecond. In previous studies by Bassett and Dlott, silica powder alone generates no heating at all when shocked by flyer plates at similar velocity.[19] The 2500 K is once again present, as the shattering glass substrate undergoes triboluminescence. Since unpressed silica analogs do show heating up to 6000 K, this finding confirms that gas compression of PDMS byproducts is sufficient to heat the sample to high temperatures when the sample has a high number of voids.

4.4 Conclusions

The shock initiation of XTX-8003 and subsequent hotspot formation is explored. By analyzing the response of XTX-8003 in a variety of ambient environments, it can be concluded that adiabatic heating resulting from gas compression (generated in situ or present in the chamber) during pore collapse is the source of the ns hotspots that we observed. Hotspot temperatures of 4000 K were reached by pressed XTX, whereas rough-surfaced, unpressed XTX and PETN crystals have hotspot temperatures of about 6000 K on the nanosecond time scale. This difference can be ascribed to the increased porosity in the latter two compounds. All samples show a plateau of 2500 K on the microsecond time scale, a consequence of the glass substrate's triboluminescence.

Under gaseous environments, the shock behavior of XTX-8003 changes in accordance with the isentropic expansion factor of the gas present. High gamma gases such as air and argon cause even pressed XTX to reach temperatures of >6000 K. Butane, which has a gamma near unity, causes very little heating and eventual deflagration. This general trend has been observed in external gas bubble collapse previously, but our experiments show that the same is true of pore collapse within a sample.

Even unpressed inert compounds can reach these high temperatures if enough gaseous products are sufficiently compressed, though far less energy is released. For pressed inert analogs, sucrose behaves similarly to pressed XTX, while silica undergoes no decomposition. Future experiments will need to be done on pressed and unpressed inert analogs in gas environments (i.e., butane, carbon dioxide, etc.) to see if the porosity at the surface is more important than the identity of the compound being shocked, as these results suggest.

It is clear that surface roughness and probably internal porosity in energetic materials is a sensitizing factor for hotspot formation in flyer plate impacts, and that adiabatic heating plays a part. These and ongoing experiments should enable greater understanding of energetic material decomposition and aid in their structural design and engineering.

4.5 References

1) P. F. Pagoria, G. S. Lee, A. R. Mitchell and R. D. Schmidt. A review of energetic materials synthesis. *Thermochimica Acta*, 2002, **384**, 187-204.

2) A. Sikder and N. Sikder. A review of advanced high performance, insensitive and thermally stable energetic materials emerging for military and space applications. *Journal of hazardous materials*, 2004, **112**, 1-15.

3) R. Matyáš and J. Pachman. *Primary explosives*, Springer, 2013.

4) M. Talawar, A. Agrawal, M. Anniyappan, D. Wani, M. Bansode and G. Gore. Primary explosives: Electrostatic discharge initiation, additive effect and its relation to thermal and explosive characteristics. *Journal of hazardous materials*, 2006, **137**, 1074-1078.

5) B. Dobratz, *LLNL explosives handbook: properties of chemical explosives and explosives and explosive simulants*, Lawrence Livermore National Lab., CA (USA), 1981.

6) T. R. Gibbs. *LASL explosive property data*, Univ of California Press, 1980.

7) Q.-L. Yan, S. Zeman and A. Elbeih. Recent advances in thermal analysis and stability evaluation of insensitive plastic bonded explosives (PBXs). *Thermochimica acta*, 2012, **537**, 1-12.

8) J. A. Zukas and W. Walters. *Fundamentals of shaped charges*, CMCPress, Baltimore, 1989.

9) L. Meirovitch. *Fundamentals of vibrations*, Waveland Press, 2010.

10) G. Langer and N. Eisenreich. Hot spots in energetic materials. *Propellants, explosives, pyrotechnics*, 1999, **24**, 113-118.

11) J. E. Field. Hot spot ignition mechanisms for explosives. *Accounts of chemical Research*, 1992, **25**, 489-496.

12) J. Kang, P. Butler and M. Baer. A thermomechanical analysis of hot spot formation in condensed-phase, energetic materials. *Combustion and flame*, 1992, **89**, 117-139.

13) A. Tokmakoff, M. Fayer and D. D. Dlott. Chemical reaction initiation and hot-spot formation in shocked energetic molecular materials. *The Journal of Physical Chemistry*, 1993, **97**, 1901-1913.

14) A. Yoffe. Influence of entrapped gas on initiation of explosion in liquids and solids. *Proceedings of the Royal Society of London A: Mathematical, Physical and Engineering Sciences*, 1949, **198**, 373-388.

15) R. B. Frey, *Cavity Collapse in Energetic Materials*, DTIC Document, 1986.

16) J. R. Verkouteren. Particle characteristics of trace high explosives: RDX and PETN. *Journal of forensic sciences*, 2007, **52**, 335-340.

17) N. Bourne and J. Field. Bubble collapse and the initiation of explosion. *Proceedings of the Royal Society of London A: Mathematical, Physical and Engineering Sciences*, 1991, **435**, 423-435.

18) A. D. Curtis, A. A. Banishev, W. L. Shaw and D. D. Dlott. Laser-driven flyer plates for shock compression science: Launch and target impact probed by photon Doppler velocimetry. *Review of Scientific Instruments*, 2014, **85**, 043908.

19) W. P. Bassett and D. D. Dlott. High dynamic range emission measurements of shocked energetic materials: Octahydro-1, 3, 5, 7-tetranitro-1, 3, 5, 7-tetrazocine (HMX). *Journal of Applied Physics*, 2016, **119**, 225103.

20) W. P. Bassett and D. D. Dlott. Shock initiation of explosives: Temperature spikes and growth spurts. *Applied Physics Letters*, 2016, **109**, 091903.

21) Q. An, Y. Liu, S. V. Zybin, H. Kim and W. A. Goddard III. Anisotropic shock sensitivity of cyclotrimethylene trinitramine (RDX) from compress-and-shear reactive dynamics. *The Journal of Physical Chemistry C*, 2012, **116**, 10198-10206.

22) K. Joshi, M. Losada and S. Chaudhuri. Intermolecular Energy Transfer Dynamics at a Hot-Spot Interface in RDX Crystals. *The Journal of Physical Chemistry A*, 2016, **120**, 477-489.

23) J. Miller, J. Mares, I. Gunduz, S. Son and J. Rhoads. The impact of crystal morphology on the thermal responses of ultrasonically-excited energetic materials. *Journal of Applied Physics*, 2016, **119**, 024903.

24) D. M. Williamson, S. Gymer, N. E. Taylor, S. M. Walley, A. P. Jardine, A. Glauser, S. French and S. Wortley. Characterisation of the impact response of energetic materials: observation of a low-level reaction in 2, 6-diamino-3, 5-dinitropyrazine-1-oxide (LLM-105). *RSC Advances*, 2016, **6**, 27896-27900.

25) M. Chaudhri and J. Field. The role of rapidly compressed gas pockets in the initiation of condensed explosives. *Proceedings of the Royal Society of London A: Mathematical, Physical and Engineering Sciences*, 1974, **340**, 113-128.